APPROVAL SHEET

Title of Thesis:	Analysis of self-induced transparency modelocking of quantum cascade lasers
Name of Candidate:	Muhammad Anisuzzaman Talukder Doctor of Philosophy, 2010

Dissertation and Abstract Approved: ______________________________

Curtis R. Menyuk
Professor
Computer Science and Electrical Engineering

Date Approved: ______________________________

Curriculam Vitae

Muhammad Anisuzzaman Talukder

EDUCATION

- **Doctor of Philosophy**, Electrical Engineering, May 2010
  University of Maryland Baltimore County (UMBC)
  Dissertation Title: Analysis of self-induced transparency modelocking of quantum cascade lasers
  Advisor: Professor Curtis R. Menyuk

- **Master of Science**, Electrical Engineering, May 2004
  Bangladesh University of Engineering and Technology
  Thesis Title: Analysis of self-phase modulation effect on optical WDM system with dispersion compensation

- **Bachelor of Science**, Electrical Engineering, May 2000
  Bangladesh University of Engineering and Technology

PROFESSIONAL EXPERIENCE

- **Research Assistant**, June 2007 – Present
  Advisor: Professor Curtis R. Menyuk
  Computer Science and Electrical Engineering
  University of Maryland Baltimore County

- **Teaching Assistant**, August 2006 – May 2007
  Computer Science and Electrical Engineering
  University of Maryland Baltimore County

- **Assistant Professor**, September 2004 – August 2006
  Electrical and Electronic Engineering
  Bangladesh University of Engineering and Technology

- **Lecturer**, February 2001 – September 2004
  Electrical and Electronic Engineering
  Bangladesh University of Engineering and Technology

- **System Engineer**, October 2000 – February 2001
  Grameen Phone Limited, Bangladesh

ACADEMIC HONORS AND AWARDS

- *Outstanding Research Contribution Award 2008–2009*, Mid-Infrared Technologies for Health and Environment (MIRTHE), National Science Foundation Engineering Research Center (NSF-ERC).

- *Best PhD Research Award 2008–2009*, Computer Science and Electrical Engineering, University of Maryland Baltimore County.
- *Second Place Award in Graduate Student Poster Competition 2008*, IEEE Baltimore and Washington-Northern Virginia LEOS chapter.

PUBLICATIONS IN JOURNALS

1. **M. A. Talukder** and C. R. Menyuk, "Self-induced transparency modelocking of quantum cascade lasers in the presence of saturable nonlinearity and group velocity dispersion," Opt. Express **18**, 5639 (2010).
2. **M. A. Talukder** and C. R. Menyuk, "Effects of backward-propagating waves and lumped mirror losses on self-induced transparency in quantum cascade lasers," Appl. Phys. Lett. **95**, 071109 (2009).
3. **M. A. Talukder** and C. R. Menyuk, "Analytical and computational study of self-induced transparency modelocking in quantum cascade lasers," Phys. Rev. A **79**, 063841 (2009).
4. C. R. Menyuk and **M. A. Talukder**, "Self-induced transparency modelocking of quantum cascade lasers," Phys. Rev. Lett. **102**, 023903 (2009) (also published in February 2009 issue of Virtual Journal of Ultrafast Science).
5. **M. A. Talukder** and M. N. Islam, "A long-haul wavelength division multiplexed system using standard single-mode fiber in presence of self-phase modulation," Opt. - Int. J. Light Electron Opt. **120**, 356 (2009).
6. **M. A. Talukder** and M. N. Islam, "Performance of bi-end compensation in a wavelength-division multiplexed system considering the effect of self phase modulation," Opt. Engineering **44**, 115005 (2005).

PUBLICATIONS / PRESENTATIONS IN CONFERENCES

1. **M. A. Talukder**,"A novel approach to create ultra-short mid-IR pulses," Graduate Research Conference 2010, University of Maryland Baltimore County (2010).
2. C. R. Menyuk and **M. A. Talukder**, "Self-induced transparency modelocking in quantum cascade lasers," SIAM Conference on Nonlinear Waves and Coherent Structures (NW10), Philadelphia, Pennsylvania (2010).
3. **M. A. Talukder** and C. R. Menyuk, "Self-induced transparency modelocking with saturable nonlinearity and group velocity dispersion," Conference on Lasers and Electro-Optics (CLEO 2010), San Jose, CA (2010).
4. **M. A. Talukder** and C. R. Menyuk, "Saturable nonlinearity and group velocity dispersion limits for self-induced transparency modelocking," MIRTHE NSF Site Visit, Princeton University, Princeton (2010).

5. **M. A. Talukder** and C. R. Menyuk, "Stability limits of self-induced transparency modelocking of quantum cascade lasers in bi-directional propagation," Conference on Intersubband Transition in Quantum Wells (ITQW 2009), Montreal, Canada (2009).
6. **M. A. Talukder** and C. R. Menyuk, "Carrier transport through quantum cascade lasers: Effects of coherence times," MIRTHE Summer Workshop, New York (2009).
7. **M. A. Talukder** and C. R. Menyuk, "Quantum cascade laser structures for self-induced transparency modelocking," MIRTHE NSF Site Visit, Princeton University, Princeton, (2009).
8. **M. A. Talukder** and C. R. Menyuk, "Stability in self-induced transparency modelocking as system parameters vary," IEEE LEOS Annual Meeting, New Port Beach, CA (2008).
9. **M. A. Talukder** and C. R. Menyuk, "Quantum cascade laser structures for self-induced transparency modelocking," International Quantum Cascade Lasers School and Workshop, Monte Verita, Switzerland (2008).
10. **M. A. Talukder** and C. R. Menyuk, "Stability of self-induced transparency modelocking in quantum cascade lasers," presented at MIRTHE Summer Workshop, Johns Hopkins University, Baltimore (2008).
11. **M. A. Talukder**, C. R. Menyuk, "Modelocking in quantum cascade lasers using self-induced transparency," presented and won the second prize at IEEE LEOS annual poster competition, Baltimore and Washington-Northern Virginia Chapter (2008).
12. **M. A. Talukder**, F.-S. Choa, C. R. Menyuk, K. J. Franz, S. S. Howard, and C. F. Gmachl, "Novel heat removal waveguide structure for high performance quantum cascade lasers," Conference on Lasers and Electro-Optics (CLEO 2008), San Jose, CA (2008).
13. **M. A. Talukder**, F.-S. Choa, and C. R. Menyuk, "High power quantum cascade laser with buried heterostructure," MIRTHE NSF Site Visit, Princeton University, Princeton (2008).
14. **M. A. Talukder**, C. R. Menyuk, and F.-S. Choa, "Comprehensive quantum cascade laser model and applications," MIRTHE NSF Site Visit, Princeton University, Princeton (2008).
15. **M. A. Talukder**, Fow-Sen Choa, and C. R. Menyuk, "Structure design for quantum cascade laser core temperature reduction," MIRTHE Summer Workshop, Princeton University, Princeton (2007).
16. **M. A. Talukder** and M. N. Islam, "Effect of self-phase modulation on optical communication system in presence of dispersion compensation," International Conference on Electrical and Computer Engineering (ICECE 2004), Dhaka, Bangladesh (2004).

17. **M. A. Talukder** and M. N. Islam, “Dependence of self-phase modulation impairments on input pulse shape over a dispersion-compensated transmission link using standard single mode fiber,” IEEE INMIC 2004, Lahore, Pakistan (2004).

WHITE PAPER

1. **M. A. Talukder**, C. R. Menyuk, and Fow-Sen Choa, “A comprehensive quantum cascade laser model,” http://www.umbc.edu/photonics/software.

INVITED TALKS

1. **M. A. Talukder**, “Quantum cascade lasers: The ultra-fast dynamics,” organized by Bangladesh University of Engineering and Technology and IEEE Electronic Devices Society – Bangladesh Chapter, Dhaka (2009).
2. **M. A. Talukder**, “Quantum cascade lasers: The art of band-structure engineering,” organized by East-West University Bangladesh and IEEE Electronic Devices Society – Bangladesh Chapter, Dhaka (2009).
3. **M. A. Talukder**, “Quantum cascade lasers, modelocking, and self-induced transparency,” Electrical Engineering Graduate Seminar, University of Maryland Baltimore County (2009).
4. **M. A. Talukder**, “Analytical and computational study of self-induced transparency modelocking in quantum cascade lasers,” Computer Science and Electrical Engineering Research Review, University of Maryland Baltimore County (2009).
5. **M. A. Talukder**, “Quantum cascade laser: Design and numerical characterization,” Electrical Engineering Graduate Seminar, University of Maryland Baltimore County (2008).

JOURNAL REFEREE

- Optics Express

PATENT

- C. R. Menyuk and **M. A. Talukder**, “Passively modelocked quantum cascade lasers,” U.S. Patent Application Serial No. 12/686,646.

Abstract

Department of Computer Science and Electrical Engineering
University of Maryland Baltimore County
Doctor of Philosophy

Analysis of Self-Induced Transparency Modelocking of Quantum Cascade Lasers

by Muhammad Anisuzzaman Talukder

The possibility of using the self-induced transparency (SIT) effect to modelock lasers has been discussed since the late 1960s, but has never been observed. It is proposed that quantum cascade lasers (QCLs) are the ideal tool to realize SIT modelocking due to their rapid gain recovery times and relatively long coherence times, and because it is possible to interleave gain and absorbing periods. Designs of QCLs are presented here that satisfy the requirements for SIT modelocking. The coupled Maxwell-Bloch equations that define the dynamics in QCLs that have both gain and absorbing periods have been solved both analytically and computationally. Analytical modelocked solutions have been found under the conditions that there is no frequency detuning, the absorbing periods have a dipole moment twice that of the gain periods, the input pulse is a π pulse in the gain medium, and the gain recovery times in the gain and the absorbing periods are much longer than the coherence time T_2 and are short compared to the round-trip time. It is shown that the modelocked pulse durations are on the order of T_2, which is typically about 100 fs. The Maxwell-Bloch equations have been solved computationally to determine the robustness of the modelocked solutions when frequency detuning is present, the dipole moment of the absorbing periods differs from twice that of the gain periods, the gain recovery time T_1 is on the order of 1–10 ps, as is typically the case in QCLs, and the initial pulse is not a π pulse in the gain medium. We find that modelocked solutions exist over a broad parameter range. We have also investigated the evolution of pulses that are initially much broader than the final modelocked pulses. As long as the initial pulse duration is on the order of T_1 or shorter and has enough energy to create a π pulse in the medium, a modelocked pulse with a duration on the order of T_2 will ultimately form.

We have developed a carrier transport model that includes both incoherent scattering and coherent tunneling mechanisms. The decay of the coherence of the levels is also included in the model. We have implemented the carrier transport model for a QCL, and we have studied the effects of an external applied electric field, a finite temperature, and the doping density on the carrier distribution in different energy levels. We find that coherence of the energy levels plays a significant role in carrier transport. In particular, when temperature increases, coherent tunneling of the electrons between the injector and the active regions decreases because the coherence time of the levels is shorter. We have then used these models to calculate the ratio of the gain obtained from one gain period and absorption obtained from one absorbing period in the SIT-modelocked QCLs. Hence we have estimated the ratio of the gain and absorbing periods for stable modelocked operation.

We have studied the effects of backward propagating waves and lumped mirror losses on SIT modelocking of QCLs. The qualitative features of the modelocking are unaffected when these effects are included in the model, but the parameter regime in which stable modelocked pulses may be found is reduced. This reduction is due to incomplete gain recovery near the edges of the QCL when pulses pass through after reflecting from the mirrors, coincident with the loss of pulse energy at the mirrors. Spatial hole burning is observed in parameter regimes in which continuous waves can grow, but it does not affect the stability of the modelocking.

We extend the model by including the effects of saturable nonlinearity and chromatic dispersion. Due to the strong intensity dependence of the refractive index of the QCL core, the loss or gain that the pulses experience may become saturated. We find that QCL modelocking is still obtained as long as either the saturable gain or the saturable loss is below a critical limit. The limit is larger in magnitude for saturable gain than it is for saturable loss by more than a factor of 10 in all cases that we examined. The critical limit also depends on the gain and absorption coefficients of the laser. There is also a critical limit for the magnitude of the chromatic dispersion. When saturable loss and chromatic dispersion act simultaneously, these two effects compensate each other and their respective stability limits increase. By contrast, when saturable gain and chromatic dispersion act simultaneously, their stability limits decrease.

Dissertation Supervisor: Curtis R. Menyuk
Title: Professor

Analysis of Self-Induced Transparency Modelocking of Quantum Cascade Lasers

by

Muhammad Anisuzzaman Talukder

A dissertation submitted in partial fulfillment
for the degree of Doctor of Philosophy

in the
Faculty of Graduate School
University of Maryland Baltimore County

May 2010

© Copyright by Muhammad A. Talukder, May 2010.
All Rights Reserved

Acknowledgements

First and foremost I would like to thank the Almighty for whatever I have achieved in my academic pursuit. There are no fitting words to properly describe His blessings that I have enjoyed during my journey towards obtaining a Ph.D. My journey towards a Ph.D has been a difficult due to my social and family responsibilities. I started my Ph.D. when I already had a family to care for. Starting as a Ph.D. student after almost six years of being a respected professional in my own country was not easy. It was emotionally unsettling when my family had to leave the USA shortly after I began my Ph.D. studies. However, I am grateful to the Almighty that He gave me the patience to hold myself together, the strength to work hard, and the ability to apply judgement. He kept me healthy and made my time more productive than I could expect. At the end, this journey has been very fruitful. I learned how to do research and fell in love with research. These years will have a profound impact on my future life.

Next, obviously I would like to thank Prof. Curtis Menyuk who supported and advised me throughout my time at the University of Maryland, Baltimore County (UMBC). The goal of a Ph.D. program is not only to accomplish specific research goals but also to train one as a scientist. More than anyone else, Prof. Menyuk has contributed to this second goal. He has given me a tremendous amount of freedom to set my own goals and seek my own solutions to problems, but at the same time he has always been approachable and encouraging when I needed help. I always have been fascinated by his scientific prowess, mathematical keenness, and analytical ability, and will always be happy that I pursued my Ph.D. dissertation under his supervision. Perhaps one of the most valuable skills I have acquired (hopefully) under Prof. Menyuk's tutelage is the ability to write clearly and present my work effectively. To the extent that the reader finds this work clear and understandable, I am deeply indebted to Prof. Menyuk. I am also deeply indebted to Prof. Menyuk because of the support that I received on a personal level during these years. I remember gratefully that when he knew that I could not afford health insurance for my family, he promptly resolved the problem.

I have benefited from many stimulating conversations with Prof. Fow-Sen Choa, and I have great esteem for his unrivaled enthusiasm and physical insight. It has been immensely helpful to attend his group meetings since spring 2007, in which

the physics of quantum cascade lasers (QCLs) was discussed, and experimentally-observed phenomena were explained. Working in Prof. Choa's lab under his supervision for a year and having a close tie with his group's work for last three years helped me gain experience with experimental research.

I must acknowledge the steadfast support of Prof. Anthony Johnson of the Center for Advanced Studies in Photonics Research (CASPR), UMBC and Prof. Claire Gmachl of Princeton University. Both of them have been very considerate and have enthusiastically supported my work on modelocking of QCLs. I am deeply grateful to Prof. Jacob Khurgin and Dr. Yamac Dikmelik at Johns Hopkins University for a number of enlightening discussions over the last few years. I would like to thank Prof. Gary Carter for what I learned in number of courses that he taught, especially, electromagnetic theory and lasers. I used many of the concepts in these courses throughout my research.

I would like to thank all present and past fellow members of the Computational Photonics Research group, with whom I have had a chance to interact. I thank Prof. John Zweck who helped me in getting started on the Optical Communication Simulator when I first joined the group, Oleg Sinkin who helped me in renting a house before I came to Baltimore, Jonathan Hu who helped me in getting started using COMSOL, and Venkat Veerasubramanian, Robert (Joe) Weiblen, Olukayode Okusaga, and David Casale for all the friendly interactions. I also would like to thank Mohit Godbole, Dingkai Guo, Xing Chen, Liwei Cheng, Tanvir Mahmood, and all others who have helped and encouraged me during my stay at UMBC.

Life at the Technology Research Center (TRC) is very convenient because of Lyn Randers, the heart and soul of the TRC building, who always had an open ear for my concerns. I also would like to thank Tim Buckheit for keeping a close eye on our group's space, especially, on our computer server, Hertz. My thanks are also to all people who work hard to make TRC a clean, safe, and friendly workplace.

Finally, I would like to acknowledge my family for their tireless love and support over the years. My parents, as always, were selfless in offering their unswerving support during my Ph.D. study. I am specially thankful to them that they took care of my wife and baby son during my studies. I also appreciate the patience of my wife during our long separations. I feel deeply sorry for depriving my son of

fatherly love and all the fun that I could and should have had with him. I also would like to acknowledge the love and care that I have always received from my brother, sisters, sister-in-law, and brother-in-laws.

Contents

Abstract i

Acknowledgements i

List of Figures vii

List of Tables xiv

Acronyms xv

Physical Constants xvi

1 Introduction 1

2 Self-Induced Transparency, Modelocking, and Quantum Cascade Lasers 9
- 2.1 Introduction 9
- 2.2 Self-Induced Transparency 10
- 2.3 Modelocking 13
  - 2.3.1 Modelocking methods 14
- 2.4 Quantum Cascade Lasers 18
  - 2.4.1 Intersubband vs. Interband Semiconductor Lasers 19
  - 2.4.2 Realization of Quantum Cascade Lasers 23
  - 2.4.3 A Typical Quantum Cascade Laser Structure 28

3 Self-Induced Transparency Modelocking of Quantum Cascade Lasers 30
- 3.1 Introduction 30
- 3.2 Physical Picture of SIT Modelocking 33
- 3.3 Maxwell-Bloch Equations 37
- 3.4 Analytical Solutions and Stability Limits 38
- 3.5 Computational Analysis 44
  - 3.5.1 Injection-Locked Pulse Dynamics 50

3.6 Conclusion 52

4 Quantum Cascade Laser Theory and Modeling **54**
4.1 Introduction 54
4.2 Electronic States in Heterostructures 55
4.3 Strained Heterostructures 59
4.4 Intersubband Radiative Transitions 61
  4.4.1 Spontaneous Emission 64
  4.4.2 Stimulated Emission 66
  4.4.3 Intersubband Gain 67
4.5 Intersubband Nonradiative Transitions 69
  4.5.1 Electron–LO Phonon Scattering 71
  4.5.2 Electron-Electron Scattering 74
  4.5.3 Electron-Interface Roughness Scattering 77
4.6 Resonant Tunneling Transport 79

5 Carrier Transport **83**
5.1 Introduction 83
5.2 Theoretical Model 85
  5.2.1 Coherence Time $T_{2,xy}$ 88
  5.2.2 Scattering Time s_{xy} 90
5.3 Carrier Transport with Electric Field 91
5.4 Effects of Temperature 95
5.5 Effects of Doping Density 98
5.6 Conclusion 101

6 QCL Structures for SIT Modelocking **103**
6.1 Introduction 103
6.2 Design Issues 104
6.3 QCL Structures 106
6.4 Ratio of Gain to Absorbing Periods 110
6.5 Conclusion 112

7 Backward-Propagating Waves and Lumped Mirror Losses **113**
7.1 Introduction 113
7.2 Theoretical Models 114
7.3 Simulation Results 117
7.4 Conclusion 120

8 Saturable Nonlinearity and Chromatic Dispersion **121**
8.1 Introduction 121
8.2 Theoretical Model 124
8.3 Nonlinearity 126
8.4 Chromatic Dispersion 132

8.5 Saturable Nonlinearity and Chromatic Dispersion . . . 135
8.6 Conclusion . . . 137

9 Conclusions **139**

Bibliography **144**

List of Figures

2.1 Schematic diagram for self-induced transparency. If a 2π hyperbolic-secant pulse is input to a resonant absorber, the leading edge of the pulse (dashed) is absorbed but the trailing edge of the pulse is amplified (solid). 11

2.2 The McCall-Hahn area theorem. Several branches of the solution to Eq. (2.1) are shown by plotting envelope area $A(z)$ against the distance of propagation z inside the medium. The value of z that corresponds to the entry face of the absorber is determined by the input area of the pulse. 12

2.3 Schematic illustration of active modelocking. 14

2.4 Actively modelocked pulse in the time domain and the time dependence of the net gain. When the gain, which is constant (indicated by a blue line) exceeds the loss, which varies sinusoidally (indicated by the red line), then the pulses can grow. 15

2.5 Schematic illustration of passive modelocking. 16

2.6 Schematic illustration of passive modelocking of laser with a slow saturable gain and a slow saturable loss. We show time dependence of pulse and the net gain. 17

2.7 Schematic diagram of the band structure and dispersion relation for an (a) interband laser and (b) intersubband laser. 20

2.8 Schematic illustration of the proposal of Kazarinov and Suris [1] to obtain light amplification from a semiconductor superlattice. We show a hypothetical I-V for this device, along with the conduction band diagrams and the location of the subbands in energy space under different bias conditions. Electron transport in the electrically-pumped structure is due to resonant tunneling. 24

2.9 First observation of sequential resonant-tunneling in a semiconductor ($In_{0.53}Ga_{0.47}As/In_{0.52}Al_{0.48}As$) superlattice with 35 periods [2]. Conduction band schematic illustrations corresponding to two different bias points in the I-V curve are shown. The I-V curve shown here is a qualitative sketch of the measured I-V curve in [2]. Note that at all biases, the ground state 1 in the quantum wells will have the largest population due to fast electron-LO phonon scattering from levels $3 \rightarrow 2$, $3 \rightarrow 1$, and $2 \rightarrow 1$. 27

2.10 Conduction band diagram and modulus-squared wavefunctions of a GaAs/AlGaAs quantum cascade laser. Levels 1–3 are in the active region and level 4 is the ground level in the injector. Level $4'$ is the ground level in the next injector. 28

3.1 Schematic illustration of a QCL structure with gain and absorbing periods. On the left, we show a cutaway view of QCL structure. The active region is shown as a filled-in rectangle. We are looking in the direction along which light would propagate. Electrodes would be affixed to the top and bottom, so that electrons flow vertically. The heterostructure would also be stacked vertically as shown on the right. We show one absorbing period for every four gain periods, corresponding schematically to the case in which the electron density in the gain periods (N_g) $\simeq$ 4×the electron density in the absorbing periods (N_a), and we show absorbing periods that are twice as large as gain periods to indicate schematically that the dipole moment in the absorbing periods (μ_a) $\simeq$ 2×the dipole moment in the gain periods (μ_g). 34

3.2 Schematic illustration of the (a) gain and (b) absorbing media. Black straight-line arrows indicate the direction of electron flow. Red wavy arrows indicate radiative transitions. 34

3.3 (a) Electric field and population inversion profile in the presence of a π pulse. An initially inverted medium becomes completely uninverted. (b) Electric field and population inversion in presence of a 2π pulse. An initially uninverted medium first becomes inverted and then becomes uninverted again. In both cases, the intensity has been normalized by the peak of the π pulse and the time has been normalized by the (full width half maximum) / 1.763 duration of the pulse. 35

3.4 Stability limits of the normalized absorption ($\bar{a}$) vs. the normalized gain ($\bar{g}$) coefficients with different values of Δ_{g0} and Δ_{a0}. The ratio T_1/T_2 is infinite in all cases. For a given $\bar{\tau}$ and $\bar{a}$, the required $\bar{g}$ increases as Δ_{g0} and $|\Delta_{a0}|$ decrease. 41

3.5 Stability limits of the normalized absorption ($\bar{a}$) vs. the normalized gain ($\bar{g}$) coefficients with different values of T_{2a}/T_{2g}. We set $T_{1g} = T_{1a} = \infty$ in all cases. At equilibrium, the gain medium is completely inverted, i.e., $\Delta g0 = 1.0$, and the absorbing medium is completely uninverted, i.e., $\Delta_{a0} = -1.0$. 42

3.6 Stability limits of the normalized absorption ($\bar{a}$) vs. the normalized gain ($\bar{g}$) coefficients with different values of T_1/T_2. In equilibrium, the gain medium is completely inverted, i.e., $\Delta_{g0} = 1.0$, and the absorbing medium is completely uninverted, i.e., $\Delta_{a0} = -1.0$. In each bundle of dashed lines, corresponding to a fixed value of $\bar{\tau}$, T_1/T_2 decreases from left to right. 46

3.7 Pulse evolution in the system. (a) Gain and absorption coefficients are in the stable regime, $\bar{g} = 4.0, \bar{a} = 3.5$. (b) Gain and absorption coefficients are in the regime in which continuous waves are unstable, $\bar{g} = 4.0, \bar{a} = 1.0$. (c) Gain and absorption coefficients are in the regime in which any initial pulse attenuates, $\bar{g} = 4.0, \bar{a} = 7.8$. The ratio T_1/T_2 equals 10 in all cases. In equilibrium, the gain medium is completely inverted, i.e., $\Delta_{g0} = 1.0$, and the absorbing medium is completely uninverted, i.e., $\Delta_{a0} = -1.0$. 47

3.8 Stability limits of the normalized absorption ($\bar{a}$) vs. the normalized gain ($\bar{g}$) coefficients with different values of T_{1a}/T_{1g}. We set $T_{2g} = T_{2a}$ and $T_{1g}/T_{2g} = 10$ in all cases. In equilibrium, the gain medium is completely inverted, i.e., $\Delta_{g0} = 1.0$, and the absorbing medium is completely uninverted, i.e., $\Delta_{a0} = -1.0$. 48

3.9 Stability limits of the ratio of dipole moments in absorbing and gain media ($\bar{\mu}$) vs. normalized gain coefficient ($\bar{g}$) for three cases of normalized absorption ($\bar{a}$). The ratio T_1/T_2 is 10 in all cases. In equilibrium, the gain medium is completely inverted, i.e., $\Delta_{g0} = 1.0$, and the absorbing medium is completely uninverted, i.e., $\Delta_{a0} = -1.0$. 49

3.10 Input pulse energy limits vs. normalized input pulse width (τ_i/T_2) for two different cases of $\bar{g}$ and $\bar{a}$. In both the cases, we set $T_1/T_2 = 10$. In equilibrium, the gain medium is completely inverted, i.e., $\Delta_{g0} = 1.0$, and the absorbing medium is completely uninverted, i.e., $\Delta_{a0} = -1.0$. 51

4.1 (a) Schematic illustration of the intersubband LO-phonon scattering process. (b) The in-plane momentum between the initial wavevector $\mathbf{k}_i$ and final wavevector $\mathbf{k}_f$ is conserved by the phonon wavevector $\mathbf{q}_\parallel$. 73

4.2 (a) Schematic illustration of some of the seven intersubband electron-electron scattering processes that are possible between two levels. There are many more possibilities since up to four levels can be involved. 75

4.3 (a) Schematic illustration of the intrasubband electron-electron scattering processes. 76

4.4 A sketch of a GaAs/AlGaAs quantum well showing the variation of the well thickness, which is the source of interface roughness. The dotted lines represent ideal interfaces. 78

4.5 Schematic illustration and the corresponding Hamiltonian for (a) the tight-binding resonant tunneling model with an interaction $-\Delta_0/2$ and (b) the analogous two-level model with a dipole interaction $-\mu E(t)$. 80

5.1 Schematic illustration of the carrier transport model. We show how the carrier density in a level in the active region is related to the other levels in the system. The blue straight arrows represent incoherent scattering mechanisms. The red wavy arrows indicate coherent carrier transport. We use double arrows for both incoherent and incoherent mechanisms to signify that the carrier transport can be in either direction. 86
5.2 Conduction band diagram and modulus-squared wavefunctions of the QCL of Sirtori *et al.* [3]. The applied electric field is (a) 40 kV/cm, (b) 50 kV/cm, (c) 60 kV/cm, and (d) 70 kV/cm. 92
5.3 Time evolution of carrier density at different levels in the QCL structure of Sirtori *et al.* [3]. The applied electric field is (a) 40 kV/cm, (b) 50 kV/cm, (c) 60 kV/cm, and (d) 70 kV/cm. The total carrier density per period is 2×10^{11} cm^{-2}. 93
5.4 Current density through the QCL as a function of the applied electric field. The total carrier density per period is 2×10^{11} cm^{-2}. . . . 95
5.5 Time evolution of carrier density at different levels in the QCL of Sirtori *et al.* [3]. The applied electric field is 60 kV/cm, and the total carrier density per period is 2×10^{11} cm^{-2}. The temperature is (a) $T = 100$ K, (b) $T = 200$ K, (c) $T = 300$ K, and (d) $T = 400$ K. 96
5.6 Carrier density at different levels vs. temperature. The applied electric field is 60 kV/cm, and the total carrier density per period is 2×10^{11} cm^{-2}. 98
5.7 Coherence time between the upper lasing level (level 3) and the injector ground level (level 4) vs. temperature. The applied electric field is 60 kV/cm and total carrier density per period is 2×10^{11} cm^{-2}. 98
5.8 Time evolution of the carrier density at different levels in the QCL of Sirtori *et al.* [3]. The applied electric field is 60 kV/cm, and the electron temperature is 200 K. The total carrier density per period is (a) $N_d = 1 \times 10^{11}$ cm^{-2}, (b) $N_d = 4 \times 10^{11}$ cm^{-2}, (c) $N_d = 7 \times 10^{11}$ cm^{-2}, and (d) $N_d = 10 \times 10^{11}$ cm^{-2}. 100
5.9 Upper lasing level (level 3) carrier density (n_3) vs. total carrier density per period (N_d) at different temperatures. The applied electric field is 60 kV/cm. 100
5.10 Coherence time between the upper lasing level (level 3) and the injector ground level (level 4) vs. total carrier density per period. The applied electric field is 60 kV/cm. 101

6.1 Conduction band diagram and modulus-squared wavefunctions for one gain and one absorbing period of the (a) 12 μm, (b) 8 μm modelocking QCL structures. The sequence of layer dimensions is (in Å, starting from left): (a) **37**, 36, **10**, 35, **10**, 34, **11**, 34, **12**, 35, **39**, 37, **12**, 62, **14**, 58, **28**, 42, **12**, 40, **13**, 37, **15**, 34, **19**, 34, **34**, 45, **11**, 65, **6**, 69; (b) **42**, 34, **9**, 33, **12**, 30, **13**, 28, **16**, 28, **41**, 27, **18**, 62, **14**, 58, **28**, 42, **12**, 40, **13**, 37, **13**, 34, **16**, 34, **34**, 9, **31**, 50, **5**, 84. The numbers in bold type indicate $\mathrm{In_{0.52}Al_{0.48}As}$ barrier layers and in roman type indicate $\mathrm{In_{0.53}Ga_{0.47}As}$ well layers. Red wavy arrows indicate radiative transitions. 108

6.2 Stability limits of $\bar{g}$ vs. $\bar{a}$ for the ~ 8 μm QCL. If the laser is operated with $\bar{a}$ above the upper red solid curve, the pulse damps, and if the laser is operated with $\bar{a}$ below the lower red solid curve, continuous waves grow. The blue dashed lines show the operating lines of the QCL with different gain to absorbing period ratios. 112

7.1 Schematic illustration of (a) Uni-directional propagation and (b) Bi-directional propagation. 114

7.2 Modelocked pulse evolution when backward-propagating waves and lumped mirror losses are considered. We set $T_{1g} = T_{1a} \equiv T_1$, $T_{2g} = T_{2a} \equiv T_2$, and $T_1/T_2 = 10$ with $T_2 = 100$ fs. 117

7.3 Stability limits of normalized gain ($\bar{g}$) versus normalized absorption ($\bar{a}$) coefficients. We set $T_{1g} = T_{1a} \equiv T_1$, $T_{2g} = T_{2a} \equiv T_2$, and $T_1/T_2 = 10$ with $T_2 = 100$ fs. The upper curves are the upper limiting values of $\bar{a}$. The bottom black line is the limiting values for continuous wave (cw) growth in both cases. 118

7.4 Stability limits for different T_1/T_2 values with $r_- = 1$ and $r_+ = 1$. Solid lines show solutions of Eq. (1), while dashed lines show solutions of Eq. (2). 119

7.5 Population inversion in the cavity. The solid lines are for $T_1/T_2 = 10$ and the dashed lines are for $T_1/T_2 = 100$. 120

8.1 Refractive index profile and resulting intensity distribution of the fundamental waveguide mode along the lateral direction of a conventional QCL waveguide in case of (a) saturable loss and (b) saturable gain. The intensity profile changes due to the strong index nonlinearity of the active region. (a) If the intensity increases, the index near the center of the waveguide increases and the mode is more tightly confined. (b) If the intensity decreases, the index near the center of the waveguide decreases and the mode is more weakly confined. 122

8.2 Modelocked pulse evolution in presence of saturable loss. The saturable nonlinearity coefficient $\gamma = 10^{-12}$ m/V^2. We set $\bar{g} = 4$ and $\bar{a} = 5$. The dispersion coefficient (β_2) is set to zero. 126

8.3 Equilibrium modelocked pulse shapes vs. the saturable nonlinearity coefficient (γ). In each case, the pulse is shown after it has propagated a distance of $1000L_c$. We set $\bar{g} = 4$ and $\bar{a} = 5$. The dispersion coefficient (β_2) is set to zero. 127

8.4 The normalized maximum intensity and pulse duration (FWHM/1.763) of the stable modelocked pulse vs. the saturable nonlinearity coefficient (γ). We set $\bar{g} = 4$ and $\bar{a} = 5$. The dispersion coefficient (β_2) is set to zero. 128

8.5 The critical values of the saturable nonlinearity coefficient (γ_c) vs. the normalized absorption coefficient ($\bar{a}$) for two values of the normalized gain coefficient ($\bar{g}$). The dispersion coefficient (β_2) is set to zero. 128

8.6 Modelocked pulse evolution in the presence of saturable gain. The saturable nonlinearity coefficient $\gamma = -10 \times 10^{-12}$ m/V^2. We set $\bar{g} = 4$ and $\bar{a} = 5$. The dispersion coefficient (β_2) is set to zero. . . . 129

8.7 Equilibrium modelocked pulse shapes vs. the saturable nonlinearity coefficient (γ). In each case, the pulse is shown after it has propagated a distance of $1000L_c$. We set $\bar{g} = 4$ and $\bar{a} = 5$. The dispersion coefficient (β_2) is set to zero. 130

8.8 The normalized equilibrium maximum intensity and pulse duration (FWHM/1.763) of the stable modelocked pulse vs. the saturable nonlinearity coefficient (γ). We set $\bar{g} = 4$ and $\bar{a} = 5$. The dispersion coefficient (β_2) is set to zero. 131

8.9 Critical values of the saturable nonlinearity coefficient (γ_c) vs. the normalized absorption coefficient ($\bar{a}$) for two values of the normalized gain coefficient ($\bar{g}$). The dispersion coefficient (β_2) is set to zero. 131

8.10 Modelocked pulse evolution in presence of chromatic dispersion. The dispersion coefficient $|\beta_2| = 5$ ps^2/m. We set $\bar{g} = 4$ and $\bar{a} = 5$. The saturable nonlinearity coefficient (γ) is set to zero. 132

8.11 Equilibrium modelocked pulse shapes vs. chromatic dispersion coefficient ($|\beta_2|$). We set $\bar{g} = 4$ and $\bar{a} = 5$. The saturable nonlinearity coefficient (γ) is set to zero. 133

8.12 The normalized maximum intensity and pulse duration (FWHM/1.763) at equilibrium vs. the dispersion coefficient (β_2). We set $\bar{g} = 4$, $\bar{a} = 5$. The saturable nonlinearity coefficient (γ) is set to zero. . . . 133

8.13 The critical values of the dispersion coefficient ($|\beta_{2c}|$) vs. the normalized absorption coefficient ($\bar{a}$) for two values of the normalized gain coefficient ($\bar{g}$). The saturable nonlinearity coefficient (γ) is set to zero. 134

8.14 Contour plot of the normalized maximum intensity vs. the saturable nonlinearity coefficient ($\gamma > 0$) and chromatic dispersion coefficient (β_2). The maximum intensity has been calculated after the pulse has propagated a distance of $1000L_c$. We set $\bar{g} = 4$ and $\bar{a} = 5$. . . . 135

8.15 Contour plot of the duration vs. the saturable nonlinearity coefficient ($\gamma > 0$) and chromatic dispersion coefficient (β_2). The duration has been calculated after the pulse has propagated a distance of $1000L_c$. We set $\bar{g} = 4$ and $\bar{a} = 5$. 136
8.16 Contour plot of the normalized maximum intensity vs. the saturable nonlinearity coefficient ($\gamma < 0$) and chromatic dispersion coefficient (β_2). The maximum intensity has been calculated after the pulse has propagated a distance of $1000L_c$. We set $\bar{g} = 4$ and $\bar{a} = 5$. . . . 137
8.17 Contour plot of the duration vs. the saturable nonlinearity coefficient ($\gamma < 0$) and chromatic dispersion (β_2). The duration has been calculated after the pulse has propagated a distance of $1000L_c$. We set $\bar{g} = 4$ and $\bar{a} = 5$. 138

List of Tables

5.1 Resonance energy splitting between the injector and active region levels. 93

Acronyms

CW	**C**ontinuous **W**ave
FWHM	**F**ull **W**idth **H**alf **M**aximum
LO	**L**ongitudinal **O**ptical
NDR	**N**egative **D**ifferential **R**esistance
QCL	**Q**uantum **C**ascade **L**aser
RNGH	**R**isken-**N**ummedal-**G**raham-**H**aken
SIT	**S**elf-**I**nduced **T**ransparency

Physical Constants

Speed of Light	c	$=$	$2.997\ 924\ 58 \times 10^{8}$ m/s
Dielectric Constant	ϵ_0	$=$	$8.854\ 187\ 817 \times 10^{-12}$ F/m
Planck Constant	$\hbar$	$=$	$1.054\ 572\ 66 \times 10^{-34}$ J-s
Electron Charge	q_e	$=$	$-1.602\ 177\ 33 \times 10^{-19}$ C
Electron Mass	m_e	$=$	$9.109\ 389\ 7 \times 10^{-31}$ kg
Boltzmann Constant	k_b	$=$	$1.380\ 658 \times 10^{-23}$ J/K

To my parents
for their unconditional support

Chapter 1

Introduction

In 1971, Kazarinov and Suris [1] proposed that light amplification is possible in a transition between two subbands of an energy band in a semiconductor with quantum wells. This proposal followed Esaki and Tsu's seminal paper of 1970 [4], presenting the concept of a superlattice. In a superlattice, thin layers that are only a few monolayers thick of two alternating materials that have different energy gaps are grown, producing barrier-well structures for the potential energy of the carriers. These quantum wells confine the carriers along the growth axis of the heterostructure [5]. In their scheme, Kazarinov and Suris [1] proposed that electrons tunnel from the ground state of a quantum well to the excited state of the neighboring well, emitting a photon in the process; this process is often called photon-assisted tunneling. After emitting a photon, the electrons relax nonradiatively to the ground state and then tunnel into the excited state of the next stage to emit another photon. This process may be repeated many times.

Unfortunately, the structure proposed by Kazarinov and Suris cannot produce gain. When several stages are cascaded, this structure cannot achieve a uniform electric field or the structure will become electrically unstable due to the formation of space charge domains when electrons are injected from the contacts [6]. The understanding of electron tunneling and relaxation rates was still in its infancy. Additionally, the known ultra-fast nonradiative relaxation of electrons by emitting longitudinal optical (LO) phonons — relaxation times are typically in the order of a picosecond — made it appear unlikely that a laser could be achieved with a subband spacing larger than the optical phonon energy. A spontaneous emission time in the nanosecond range, i.e., several orders of magnitude slower than the nonradiative scattering events, supported the notion of a highly inefficient optical system. The stimulated optical emission time, however, easily approaches the fast nonradiative scattering times.

Recognizing that the fast nonradiative LO phonon emission rate, rather than being a hindrance for intersubband laser action can be harnessed for the laser process, Faist *et al.* [7] demonstrated the first intersubband laser, i.e., the quantum cascade laser (QCL), in 1994 through careful band-structure engineering. They added injectors to the basic Kazarinov and Suris [1] active regions that would inject electron into the upper lasing level and would collect them from the lower lasing levels when an appropriate bias voltage is applied across the structure. These injector regions act as electron reservoirs as they are pre-doped to be n-type when the structure is grown. The population inversion was achieved by engineering the lifetime between the two lasing levels and introducing a level below the lower lasing level at the LO phonon resonance, so that the lower level is quickly depopulated by emitting LO phonons. The first demonstrated QCL emitted light at a wavelength of 4.3 μm and produced a power of 10 mW in pulse-mode and at cryogenic temperatures. The first QCL was grown using state-of-the-art molecular beam epitaxy (MBE) technology [8, 9].

The QCL's unique properties compared to other semiconductor lasers, such as the ease of generating light at a design wavelength, tunable gain spectrum [10], and ultra-fast carrier dynamics, make them the most important semiconductor lasers that operate today in the mid-infrared. Since their invention, QCLs have undergone great developments in tailoring the emission wavelength so that they can operate in the near- and far-infrared region, increasing their power so that it is possible to generate several watts, making them increasingly efficient, enabling them to emit single-mode and multi-mode, and increasing their tuning over a wide wavelength range [11, 12]. The successes have been made possible by employing improved band-structure engineering, new material systems that give different conduction band offsets, waveguide engineering, and by increased knowledge of the basic physics of QCLs, especially carrier transport. However, efforts are underway to make the QCLs lase at a wavelength beyond the presently obtainable range, e.g., at $\lambda < 3$ μm, to increase their output powers, to make them more efficient, and to make them tunable over a broader range. In addition, efforts have been made to modelock QCLs in order to obtain short pulses. Active modelocking of QCLs that produces ~ 3 ps pulses has recently been achieved [13]. However, it has not proved possible to date to passively modelock QCLs and obtain sub-picosecond pulses.

Modelocking is a technique to generate stable trains of ultrashort light pulses with large instantaneous intensities from a laser [14]. These pulses are the key elements for many important applications such as nonlinear frequency conversion [15–17], time-resolved measurements [18, 19], coherent control [20, 21], and frequency combs [22]. To date, the most common approach to generate short pulses in the mid-infrared (3.5–20 μm) molecular "fingerprint" region relies on the down-conversion of short-wavelength modelocked lasers through nonlinear processes, such as optical parametric generation [23–25] and four-wave mixing [26]. These systems are usually bulky, expensive, and typically require a complicated optical arrangement.

There are two basic approaches to modelocking. First is active modelocking [14], in which the laser is electronically modulated using an electro-optic modulator or some other means at a harmonic of a light pulse's round-trip in the laser. In this approach, there is a tradeoff between the pulse duration and the repetition rate, so that it is not possible to obtain sub-ps pulses from a semiconductor laser. The second approach is passive modelocking [14], also called self-modelocking, in which the formation of short pulses is energetically more favorable than the formation of dispersive waves. That can be accomplished, for example, by combining a fast saturable loss with a slow saturable gain. Using passive modelocking, it is possible to obtain pulses with a duration below 100 fs [27]. While QCLs have been actively modelocked [13], they have never been passively modelocked.

Conventional passive modelocking techniques are difficult to apply to QCLs because of their inherently narrow linewidths and large coherence times T_2 relative to other semiconductor lasers and their very fast gain recovery time T_1 compared to the cavity round-trip time T_{rt} [28, 29]. The gain linewidth in QCLs is narrow compared to other semiconductor lasers because the lasing transition takes place between two subbands within the conduction band [30]. The gain recovery time of a conventional QCL is generally on the order of a ps due to carrier transport by resonant tunneling and LO phonon relaxation [31, 32], while the round-trip in a typical 3-mm-long cavity of conventional QCLs takes around 50 ps. The condition $T_1 \ll T_{\mathrm{rt}}$ makes it difficult to form a pulse and the laser often becomes unstable when operated above threshold due to the Risken-Nummedal-Graham-Haken (RNGH) instability [27, 33, 34]. If the gain recovery time is longer than the cavity round-trip time, then a single laser pulse oscillating in the cavity depletes the gain and prevents the formation of other pulses; if the gain recovery time is much shorter than the cavity round-trip time, multiple pulses that are separated by the gain recovery time or more can propagate in the laser cavity. If the gain recovery time is faster than the pulse duration, the gain reacts nearly instantaneously to the intensity of the pulse. In this case, the peak of the pulse saturates the gain, and the wings of the pulse, which have too low an intensity to saturate the gain, experience more gain than the peak of the pulse. This process leads to lengthening of the pulse, i.e., the suppression of intensity fluctuation, which suppresses modelocking and leads to continuous-wave (CW) lasing. The latter situation is what occurs in most QCLs.

There have been several reports of modelocking in QCLs [13, 35–38]. However, the evidence for modelocking reported in [35–38] were based on broadband optical spectra with a large number of longitudinal modes and a narrow microwave beat note in the power spectrum at the laser round-trip frequency, which indicated that the electric field waveform circulating in the laser cavity and thus the phase relationship between the longitudinal modes was stable over a large number of round-trips. However, due to the lack of a suitable apparatus for second-order autocorrelation measurements, no direct evidence was given to demonstrate that the circulating waveform was indeed a periodic sequence of isolated pulses, which would result from all modes having equal and stable phases. Subsequent pulse characterization using autocorrelation techniques showed that under the previous conditions, the output of free running QCLs was not composed of one isolated pulse per round-trip [28, 29]. The physics of multimode behavior observed in those lasers is described by spatial hole burning and the RNGH instability [28, 29], rather than by modelocking. Only Wang *et al.* [13] reported unequivocal demonstration of modelocked pulses from a mid-infrared QCL. Wang *et al.*'s [13] success came through using a two-section specially engineered QCL in which they actively modulated the gain of the smaller section while applying a fixed bias to the larger section. Using this active approach, they obtained pulse with a 3 ps duration.

The fundamental objective of the research work presented in this dissertation is to find a new approach to modelock quantum cascade lasers in their usual parameter regime, which will allow in principle the generation of sub-ps pulses. We propose that the self-induced transparency (SIT) effect can be used to modelock QCLs. For this purpose, one must grow QCLs with absorbing periods in addition to the gain periods. The absorbing periods help stabilize the pulses by preferentially absorbing continuous waves, while allowing sub-ps pulses to pass through the laser with a smaller loss. In this dissertation, we will discuss the physical concept of SIT modelocking, we will present the results of analytical and computational studies that demonstrate the viability of this concept, we will present QCL designs that satisfy the requirements for SIT modelocking, and we will demonstrate the robustness of SIT modelocking when backward-propagating waves, mirror losses, saturable nonlinearity, and chromatic dispersion are taken into account.

The remainder of the dissertation is organized as follows:

Chapter 2 introduces self-induced transparency, modelocking, and quantum cascade lasers. In this chapter, we describe SIT, present the McCall-Hahn area theorem, and then discuss the pulse shaping capability of SIT. Next, we discuss the basics of different (i) active and (ii) passive modelocking approaches, and draw a line from the first proposal of light amplification from an intersubband transition by Kazarinov and Suris in 1971 [1] to the realization of the first QCL in 1994 [7]. Finally, we discuss the band-structure engineering of QCLs that has made lasing possible and the distinct features of an intersubband laser, i.e., QCLs, compared to an interband laser. Chapter 2 also gives an overview of the present status of QCL research.

Chapter 3 describes our proposal to use SIT to modelock QCLs as an alternative to the conventional passive modelocking mechanism. This proposal overcomes the difficulties with conventional passive modelocking techniques in modelocking QCLs due to the fast gain recovery time and narrow gain bandwidth relative to interband semiconductor lasers. In this chapter, we illustrate the physical concept of SIT modelocking using a simple two-level model. We present analytical modelocked solutions of the Maxwell-Bloch equations that describe the dynamics in a QCL in special cases, and we derive the conditions for stable modelocking. In Chapter 3, we give a detailed computational analysis of the stability limits of the key parameter values for stable modelocked pulse evolution. We also calculate the pulse dynamics, in order to determine the initial pulse durations and intensity that lead to stable operation.

Chapter 4 describes the theoretical and computational approaches that we use to model a QCL. We discuss the procedure to calculate the electronic states in a multi-quantum-well heterostructure like a QCL. We then describe the different transition rates that characterize a QCL and show how to calculate them. These include the intersubband radiative transition rates, inter- and intrasubband nonradiative transition rates, and tunneling rates.

Chapter 5 presents carrier transport calculations for QCLs. It introduces a model to calculate the carrier density in the energy levels of a QCL's active and injector regions. This model incorporates the carrier scattering and tunneling contributions under different design and operating conditions. We also introduce a model for the coherence time T_2 between two energy levels, which is an integral part of the model to calculate the carrier transport and is a key parameter in the operation of SIT modelocking. Chapter 5 also presents the implementation of the carrier transport model for a QCL structure. We find the time evolution of the carrier densities at different energy levels as the applied electric field, operating temperature, and total carrier density vary. The coherence time T_2 is calculated in each case to show the impact of coherence on the carrier transport of QCLs.

Chapter 6 presents practical QCL designs at two different wavelengths that satisfy the requirements for SIT modelocking. This chapter discusses the issues that must be addressed when designing these structures. We present the calculation of the ratio of number of the gain to absorbing periods to determine the actual number of gain and absorbing periods that are required for stable operation.

Chapter 7 discusses the impact of backward-propagating waves and lumped mirror losses on SIT modelocking. The discussion in Chapter 3 does not take into account the backward-propagating waves and averages the lumped mirror losses over the length of the cavity. By contrast, Chapter 7 treats a realistic geometry in which waves propagate in both directions and lose a significant amount of their energy at each mirror, depending on the reflection coefficients.

Chapter 8 discusses the impact of saturable nonlinearity and chromatic dispersion on SIT modelocking. The discussion in Chapter 3 does not take into account the intensity-dependent modulation of the index of refraction in the laser cavity and chromatic dispersion in the laser medium. Due to the intensity dependence of the index of refraction, a propagating pulse may experience saturable loss or saturable gain. A narrow pulse may broaden while propagating through a dispersive medium. Since the generation of very intense and narrow pulses is the focus of this dissertation, these effects should be investigated. Chapter 8 presents and discusses these results.

Chapter 9 summarizes the results and concludes.

Chapter 2

Self-Induced Transparency, Modelocking, and Quantum Cascade Lasers

2.1 Introduction

The principal objective of this dissertation is to theoretically demonstrate that quantum cascade lasers (QCLs) operating in their standard parameter regime can be self-modelocked and sub-picosecond pulses can be obtained without using the conventional passive techniques. QCLs cannot be modelocked using conventional passive modelocking technique due to their fast gain recovery times relative to the round-trip time in the lasers and their narrow gain bandwidths relative to other semiconductor lasers. We will instead propose a new technique, self-induced transparency (SIT) modelocking, to modelock these lasers, and we will show that stable modelocking with sub-ps pulses is obtained. Hence, three basic concepts — (i) self-induced transparency, (ii) modelocking, and (iii) quantum cascade lasing — are inter-weaved in this dissertation. In this chapter, we will describe these three concepts.

The remainder of this chapter is organized as follows: Sec. 2.2 introduces the concept of SIT. We will describe how SIT can be used to compress pulses in accordance with the area theorem. In Sec. 2.3, we will introduce the basic modelocking concept and describe different conventional ways to modelock lasers. In Sec. 2.4, we will present QCLs. We will give a brief introduction of the history of QCLs, describe the key features of QCLs, and explain how quantum cascade strucutres are engineered to produce light.

2.2 Self-Induced Transparency

McCall and Hahn [39, 40] observed that a pulse with a duration τ that is short compared to the coherence time T_2 of a saturable resonant medium will pass through the medium as if the medium were transparent, as long as the pulse energy exceeds a critical value. They gave this effect the name self-induced transparency (SIT). When the pulse energy is below the critical value, the pulse damps. SIT reshapes pulses in the correct energy range, so that they have a hyperbolic-secant shape with a well-defined energy and duration. In a two-level resonant absorber, ideal transparency persists when stimulated absorption of pulse energy during the first half of the pulse is coherently followed by stimulated emission during the second half of the pulse, as shown schematically in Fig. 2.1. The pulse velocity is smaller than the velocity of nonresonant light in the medium because of the continual absorption of energy from the pulse's leading edge and emission of energy into the pulse's trailing edge.

McCall and Hahn [39, 40] derived a theorem for $A(z)$ the integral of the intensity envelope's magnitude of a resonant propagating light pulse multiplied by $\mu/\hbar$, where μ is the medium's dipole moment and $\hbar$ is Planck's constant. This theorem is generally referred to as the area theorem. According to the area theorem, $A(z)$ obeys the relation

$$\frac{dA(z)}{dz} = -\frac{\alpha}{2}\sin A(z), \tag{2.1}$$

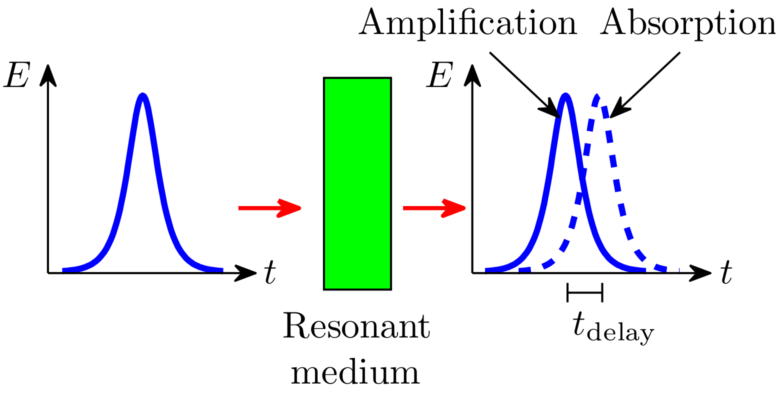

FIGURE 2.1: Schematic diagram for self-induced transparency. If a 2π hyperbolic-secant pulse is input to a resonant absorber, the leading edge of the pulse (dashed) is absorbed but the trailing edge of the pulse is amplified (solid).

where α is the linear optical attenuation coefficient for the material. The area theorem implies the following: (i) When the pulse is weak, $\sin A \sim A$. Therefore, the pulse will decay exponentially. (ii) A pulse whose initial area equals positive integral multiples of π, i.e., $A(z = 0) = n\pi$, $n = 1, 2, \ldots$ will maintain the same area during propagation. (iii) A pulse with another initial area will evolve until its area reaches the nearest even multiple of π. Hence, areas with even multiples of π are stable, and areas with odd multiples of π are unstable. The evolution of the pulse envelope area $A(z)$ has been plotted in Fig. 2.2. We see that pulses with an initial area of slightly less than π, e.g., with an area of 0.9π, damp, while pulses with an initial area of 1.1π and 2.9π both evolve to pulses having an area of 2π. The area theorem also shows that 2π is not the only solution; rather, any integer multiple of 2π is a solution.

McCall and Hahn [39, 40] verified their initial theoretical predictions of SIT with experimental observations in a ruby sample at resonance with a pulsed ruby-laser beam. They observed single and multiple 2π pulse outputs, and they measured pulse areas in the range of 2π. A number of experimental observations of SIT in different laser systems followed in the literature [41–45]. Patel and Slusher [41] were the first to present results for a gaseous absorber. They demonstrated

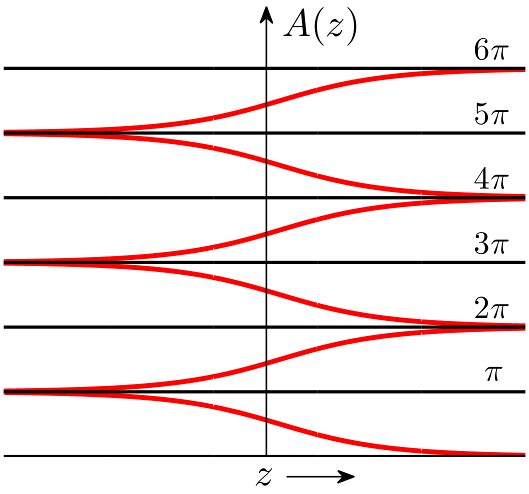

FIGURE 2.2: The McCall-Hahn area theorem. Several branches of the solution to Eq. (2.1) are shown by plotting envelope area $A(z)$ against the distance of propagation z inside the medium. The value of z that corresponds to the entry face of the absorber is determined by the input area of the pulse.

delay times of about 0.2 μsec in SF_6, and found output pulses that appeared more symmetric than the input pulses produced from a CO_2 laser. However, their work was questioned, particularly by Rhodes *et al.* [42], because of the level degeneracy in SF_6 and because of the possibility of bleaching or incoherent saturation. In a subsequent work, Patel [43] argued against the idea that incoherent bleaching was the explanation of the results by showing that the optical delay was intensity-dependent, and that at higher SF_6 pressures the delay began to decrease after passing a maximum. Gibbs and Slusher [44] carried out detailed experiments on the propagation of coherent optical pulses in dilute Rb vapor, a nodegenerate resonant absorber. They verified most of the basic aspects of SIT including the area theorem.

Due to the inherent pulse-shaping of SIT characterized by the area theorem, it has been used to compress optical pulses. Gibbs and Slusher [46] have compressed and amplified strong pulses by sending them through an absorbing medium, and they reported a compression of an order of magnitude. Their starting point was a pulse with an area slightly less than 3π, which according to Fig. 2.2 will reshape into a pulse of area 2π. Bonafico *et al.* [47] showed theoretically that the SIT effect can generate short pulses when pulses that are short compared to the coherence time in the medium propagate through a medium with both nonlinear absorption and gain.

2.3 Modelocking

The word modelocking implies the locking of multiple axial modes in a laser cavity. By enforcing coherence between the phases of the different modes, pulsed radiation can be produced. Modelocking is a resonant phenomenon. A pulse is initiated by a relatively weak modulation synchronous with the round-trip time of the radiation circulating in the laser and then grows shorter on every pass through the resonator. Eventually the shortening process is limited by frequency-domain filtering that is due to the finite modulation depth in the case of active modelocking, the finite gain bandwidth in the case of conventional passive modelocking, and — as we will show — the Rabi frequency in the case of SIT modelocking. The history of laser modelocking dates back more than 40 years, and, since its discovery, there has been a continuous effort to generate shorter pulses using new and better techniques [48–60].

The first indications of modelocking appear in the work of Gürs and Müller [48, 49] on ruby lasers, and Statz and Tang [50] on He-Ne lasers. The first papers clearly identifying a modelocking mechanism were written in 1964 by DiDomenico [51], Hargrove *et al.* [52], and Yariv [53]. Hargrove *et al.* [52] achieved active modelocking by internal loss modulation inside the resonator. Mocker and Collins [54] showed that the saturable dye used in ruby lasers to Q-switch a laser could also be used for modelocking. Crowell [61] reported both theoretically and experimentally the passive generation of short pulses by mode-coupling in a gas laser resulting from a time-varying loss within the optical cavity or from the nonlinear characteristics of the inverted population. Ippen *et al.* [55] generated the first cw saturable absorber modelocking using a saturable dye in a dye laser. Shortly thereafter,

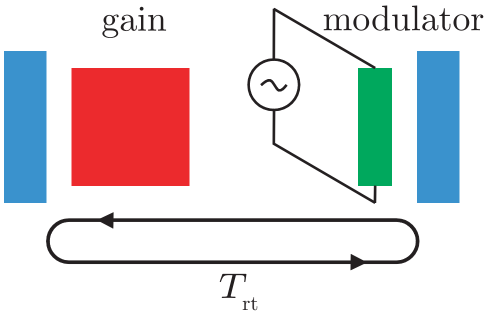

FIGURE 2.3: Schematic illustration of active modelocking.

this work led to the production of sub-picosecond pulses [56]. The work on dye lasers continued unabated for the next decade producing increasingly short pulses [57–59]. Ultimately, a record 6-fs pulse duration was achieved by Fork *et al.* [60] using pulse compression external to the cavity.

2.3.1 Modelocking methods

Methods for producing modelocking in a laser to date have been classified as either (i) active or (ii) passive [14, 27]. Active methods use an external electrical signal and an electro-optic modulator to induce a modulation of the intra-cavity light. Passive methods do not use an external signal, but rely on elements in the laser cavity that cause a self-modulation of the light by making the production of short pulses more energetically favorable than continuous waves. The theory of active modelocking was firmly established in a classic paper by Kuizenga and Siegman [62], while the theory of passive modelocking was developed by Haus [63, 64].

Active modelocking

The most common active modelocking technique uses an amplitude modulator (AM) in the laser cavity that sinusoidally modulates the light, as shown in Fig. 2.3. This process is most easily analyzed in the frequency domain. If a mode has optical frequency ν and is modulated at a frequency f, the resulting signal has sidebands at optical frequencies $\nu - f$ and $\nu + f$. If the modulator is driven at the same

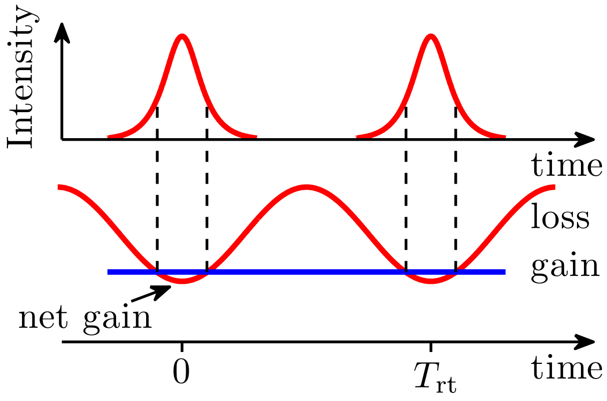

Figure 2.4: Actively modelocked pulse in the time domain and the time dependence of the net gain. When the gain, which is constant (indicated by a blue line) exceeds the loss, which varies sinusoidally (indicated by the red line), then the pulses can grow.

frequency as the cavity-mode spacing $\Delta\nu$, which is the round-trip frequency $1/T_{\mathrm{rt}}$, then these sidebands correspond to the two cavity modes adjacent to the original mode. Since the sidebands are driven in phase, the central mode and the adjacent modes will be phase-locked together. Further operation of the modulator on the sidebands produces phase-locking of the $\nu - 2f$ and $\nu + 2f$ modes and so on until the loss exceeds the gain.

The active modelocking process can also be considered in the time domain. The amplitude modulator produces a time window in which the gain exceeds the loss and therefore acts on the light bouncing between the mirrors of the cavity like a weak shutter, attenuating the light when it is “closed,” and letting it through when it is “open.” If the modulation rate f is synchronised to the cavity round-trip time T_{rt}, then a single pulse of light will bounce back and forth in the cavity, as shown schematically in Fig. 2.4. The actual strength of the modulation does not have to be large; a modulator that attenuates 1% of the light when “closed” will modelock a laser [14], since the light is repeatedly attenuated as it traverses the cavity.

It is possible to use frequency modulation (FM) rather than amplitude modulation to actively modelock a laser [62, 65, 66]. This approach uses a standing

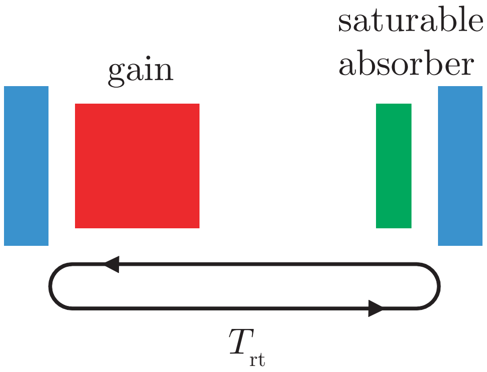

FIGURE 2.5: Schematic illustration of passive modelocking.

wave modulator based on the acousto-optic effect. This device induces a small, sinusoidally varying frequency shift in the light passing through it. If the frequency of the modulation is matched to the round-trip time of the cavity, then some light in the cavity experiences repeated up-shifts in frequency, and some of the light experiences repeated down-shifts. After many repetitions, the up-shifted or down-shifted light is swept out of the bandwidth that experiences net gain. The only light that is unaffected is the light that passes through the modulator when the induced frequency shift is zero, which forms a short pulse of light.

A third method of active modelocking is synchronous modelocking or synchronous pumping [67–71]. In this approach, the pump source (energy source) for the laser is itself modulated, effectively turning the laser on and off to produce pulses. Typically, the pump source is itself another modelocked laser. This technique requires accurately matching the cavity lengths of the pump laser and the driving laser.

Passive modelocking

Passive modelocking techniques do not require a signal external to the laser, such as the driving signal of a modulator, to produce pulses. Rather, the light in the cavity changes one or more intracavity elements, which in turn produces a change in the intracavity light. Commonly, one combines a slow saturable gain with either

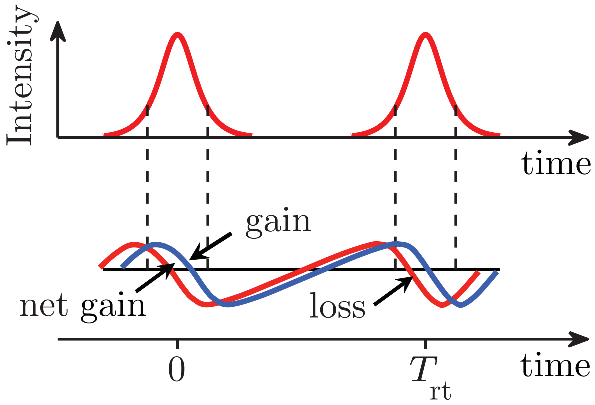

FIGURE 2.6: Schematic illustration of passive modelocking of laser with a slow saturable gain and a slow saturable loss. We show time dependence of pulse and the net gain.

a fast or a slow saturable loss, as shown in Fig. 2.5. In any combination, the light dynamically affects the cavity gain in a way that favors the production of short pulses rather than continuous waves.

In Fig. 2.6, we show a schematic illustration of a passively modelocked system that combines a slow saturable gain with a slow saturable loss. In this case, the pulse creates its own narrow time window in which the gain exceeds the loss. Hence, short pulses are stable. In some cases in which continuous waves are modulationally unstable, the modelocking will self-start from noise. In other cases, one must seed the modelocking with a mechanical or electrical shock.

Passively modelocked lasers of current importance that use slow saturable loss include semiconductor lasers and fiber lasers with semiconductor saturable absorbing mirrors (SESAMs) [72–74] and carbon nanotubes [75]. Passively modelocked lasers of current importance that use fast saturable absorbers include fiber lasers that are locked using nonlinear polarization rotation [76] and nonlinear optical loop mirrors (NOLMs) [77] and solid-state lasers like Ti:Sapphire lasers that are locked using Kerr lens modelocking [78–80]. In all cases, the lasers use a slow saturable gain.

Active modelocking does not lead to ultrashort pulses. Near the peak of the gain modulation, the gain varies in time as $g(t) = g_0(1 - 4\pi^2 f^2 t^2)$, where f is the modulation frequency and g_0 is the peak gain. As the pulse duration decreases, the effect of the modulation diminishes quadratically, so that it eventually becomes ineffective. By contrast, since a passively modelocked pulse directly modulates the gain that it experiences, the modulation remains effective as the pulse duration decreases. Ultimately the bandwidth of the gain medium and the mirrors limit the pulse duration.

2.4 Quantum Cascade Lasers

QCLs are electrically pumped unipolar photonic devices in which light emission takes place due to intersubband optical transitions in two-dimensional quantum wells of semiconductor heterostructures. QCLs are an example of "bandgap engineering." In these lasers, the energy spacing between the subbands that are involved in the lasing transition, and hence the frequency of the light emission, can be engineered by varying the thickness of the quantum wells. Another key characteristic of QCLs is the use of periodically-repeated multiple quantum well structures, in which each period has an active region and can generate a photon. Thus, an electron will generate multiple photons as it passes through the QCL.

The most commonly used technology for creating superlattice and quantum well semiconductor structures is molecular beam epitaxy (MBE) [8, 9], where layers as thin as several monolayers can be grown with atomic precision. Milestones in the realization of QCLs include the invention of the concept of a superlattice by Esaki and Tsu [4], the proposal for light amplification in an intersubband transition by Kazarinov and Suris [1], the first observation of intersubband absorption in a quantum well in 1985 [81], and the first observation of sequential resonant tunneling in a superlattice in 1986 [2]. Helm *et al.* were the first to observe intersubband emission in a superlattice, initially pumped by thermal excitation [82] and then by resonant tunneling [83]. However, it took two decades until the first laser based on intersubband transitions, i.e., the QCL, was experimentally demonstrated by Faist *et al.* [7]. This first demonstrated laser worked at 10 K in pulsed mode with a peak power of 10 mW. The emission wavelength was $\lambda \sim 4.3$ μm.

QCLs have achieved dramatic performance improvements since their invention and have become the dominant semiconductor laser sources in the mid-infrared spectral range. An overview of the history of the QCL's development as well as descriptions of state-of-the-art designs, will be given in this section. More detailed discussions may be found in the review papers by Capasso *et al.* [84], Faist *et al.* [85], and Gmachl *et al.* [86].

QCLs emitting at a wavelength as short as 3 μm has been demonstrated to lase at 80 K [87], while room temperature pulsed mode operation has been achieved down to 3.5 μm [88], and room temperature CW operation has been achieved at 3.8 μm [89]. Terahertz QCLs have been demonstrated in the range of $\sim$ 60–300 μm [90–93] at an operating temperature up to 178 K [94] and can also operate at 300 K when THz frequencies are generated via difference frequency generation [95]. There have been breakthrough advances toward realization of high power CW operation above room temperature, including stable single-mode operation. A CW output power as high as 300 mW at 298 K in the wavelength range of $\lambda \sim 4.8 - 6.0$ μm was demonstrated using a strain-balanced GaInAs/AlInAs heterostructure [96, 97]. A record temperature of 400 K at 8.38 μm has been achieved [98].

2.4.1 Intersubband vs. Interband Semiconductor Lasers

In Fig. 2.7, we schematically show two-dimensional quantum heterostructures for intersubband and interband transitions. In an interband laser, a transition occurs in which an electron in the conduction band combines with a hole in the valence band and energy is released. Therefore, an interband laser is inherently bipolar in nature. The frequency of the radiation is determined by the bandgap energy E_g of the quantum well material (which is on the order of 1 eV or $\lambda \sim 1.24$ μm).

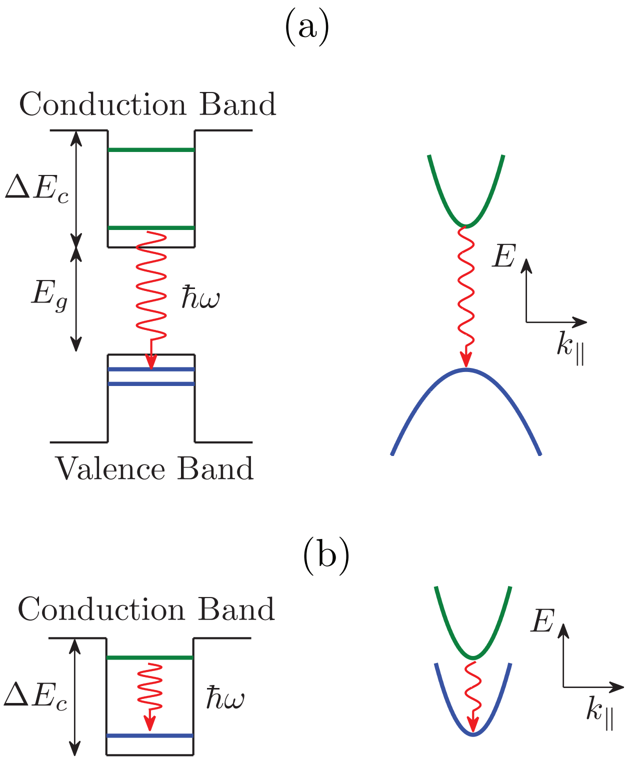

FIGURE 2.7: Schematic diagram of the band structure and dispersion relation for an (a) interband laser and (b) intersubband laser.

However, a small fractional tuning of the emission wavelength can be obtained by varying the quantum well thickness. The joint density of states for the optical transition is constant, which is typical of the two-dimensional density of states for a parabolic $E(k_{\parallel})$ dispersion with opposite curvatures in the conduction and valence bands. Therefore, the gain spectrum is typically broad at temperatures where the thermal distribution of the carriers have a pronounced effect.

On the contrary, an intersubband transition happens between two subbands within a single energy band. Therefore, intersubband lasers are inherently unipolar since they use only electrons in the conduction band or holes in the valence band. Intersubband lasers have two major advantages. First, the emission wavelength is no longer a function of the bandgap energy of the material, but depends on the quantum well thickness, which can be engineered. The shorter wavelength limit is set by the conduction band offset ΔE_c of the materials used in the heterostructure for the quantum well and barrier, and the longer wavelength limit is set by the wavelength of the optical phonons, design complexity, and temperature. Second, as the subbands lie within the same band, they have the same curvature in the energy dispersion relation. If non-parabolicity in the energy dispersion relation is neglected, the subbands have a joint density of states that can be expressed as $\rho(E) = \delta(E - \hbar\omega)$, where $\delta(x)$ is the Dirac delta function. Therefore, all the inverted carriers emit light at nearly the same wavelength. As a consequence, the gain can potentially be very large, since the gain $g(E) \propto \rho(E)$. However, this advantage is offset by the short nonradiative lifetimes for intersubband transitions that are on the order of a ps, as compared to the nonradiative electron-hole recombination times in an interband diode-laser that are on the order of a ns, mostly due to fast polar longitudinal optical (LO) phonon intersubband scattering in semiconductor heterostructures. The relatively short lifetimes of the intersubband transitions limit the amount of population inversion that can be achieved. One may compensate in part for this disadvantage by engineering the lifetime of the two lasing levels using a multi-quantum well structure. In addition, a cascade of the basic period is used that increases the gain by a multiple of the number of periods used. The unipolar nature of intersubband transitions makes this cascade possible.

Based on these basic operating principles, there are several characteristics that distinguish interband lasers from intersubband lasers. For an intersubband laser such as a QCL, despite having close to a delta-function-distributed joint density of states, the gain spectrum has a finite width due to homogeneous broadening from collisions as well as inhomogeneous broadening from fluctuations in the material growth of the subbands. By contrast, in an interband laser, the broadening of the gain spectrum is principally due to the thermal distribution of the carriers. Typical full-width half-maximum (FWHM) spontaneous-emission linewidths observed for QCLs have been 2–20 meV, as compared to $\sim$ 50 meV or more for the interband quantum-well diode lasers [99]. An intersubband laser usually has an even, Lorentzian-shaped gain spectrum around the peak gain frequency. Consequently, the Kramers-Kronig relations dictate that the contribution of the imaginary part of the laser transition to the index of refraction must be odd about the peak gain frequency, and hence zero at the center. As a result, the linewidth enhancement factor in an intersubband laser is smaller than in an interband diode-laser by at least an order of magnitude [100]. A small linewidth enhancement factor allows an intersubband laser to maintain optical coherence over large device areas [101], which is important for the development of high-power surface-emitting lasers, among other applications.

The short nonradiative relaxation time leads to distinctive features in the high frequency modulation response of QCLs. Experimental observation shows that the relaxation oscillations that are typically observed in the modulation response of interband diode-lasers are absent in QCLs [102]. However, the modulation bandwidth of QCLs, like that of interband lasers, is limited by the photon lifetime in the cavity, which is on the order of 10 GHz. This lifetime is the longest of all the lifetimes that determine the modulation response. As a consequence, an intersubband laser offers no particular advantages over interband diode lasers, despite having nonradiative carrier relaxation mechanisms that are orders of magnitude faster.

Another distinctive feature of QCLs is their multi-mode behavior due to spatial hole burning. QCLs use a standing wave configuration, in which the forward- and backward-going waves interfere each other and produce standing waves [14]. As the gain recovery time is orders of magnitude shorter than the diffusion time, spatial hole burning may be observed when the input current is above the lasing threshold [29]. The fast gain recovery time also plays a negative role when modelocking QCLs. Since the gain recovery time is on the order of 1 ps and the cavity round-trip time is on the order of 50 ps, stable modelocked pulses cannot be generated [27]. Instead, the lasers become unstable due to the Risken-Nummedal-Graham-Haken effect [28, 29].

2.4.2 Realization of Quantum Cascade Lasers

In 1960, before the invention of the diode laser, a semiconductor laser based on transitions between Landau levels in a strong magnetic field was proposed by Lax [103]. This proposed semiconductor laser was the first in which the optical transition occurs between low-dimensional states of the same band (conduction or valence) rather than across the semiconductor bandgap. The idea of a unipolar laser was then ignored for many years since only two years after Lax's proposal, the first diode laser was demonstrated [104].

In 1970, Esaki and Tsu published a seminal paper presenting the concept of a superlattice [4]. A year later, Kazarinov and Suris suggested that optical gain could be obtained by using transitions between two-dimensional states in a superlattice biased by an external electric field [1]. This structure, which was very different from other semiconductor lasers, introduced the concept of a unipolar device in which the optical transitions could be completely engineered by the judicious choice of the quantum well thickness and barrier materials, regardless of the material's bandgap.

Though the present day QCLs differ significantly from the original structure that Kazarinov and Suris proposed [1], we will discuss their proposed structure since this structure laid the foundation of QCLs, and understanding the physics of this simple structure helps in understanding the physics of the more complicated QCL structures. In Fig. 2.8, we show schematically the proposed structure of Kazarinov and Suris [1]. The structure basically consists of a semiconductor superlattice of multiple repeated quantum wells. The quantum wells are electrically pumped as electrons transport through the one-dimensional periodic potential of the heterostructure. The energy separation between the first excited state 2 and the ground state 1 is approximately at the LO phonon emission energy $\hbar\omega_{\mathrm{LO}}$. Therefore, electrons within the wells scatter very fast from the excited state to the ground state by emitting LO phonons. The excited states have a lifetime much less than one ps. By contrast, the carrier transport between the wells through the barrier is mainly due to tunneling. The transport rate due to tunneling depends on the barrier thickness, barrier height, and the applied electric field. The combination of resonant-tunneling and intersubband scattering for electron transport in multiple quantum wells is often described as sequential resonant-tunneling.

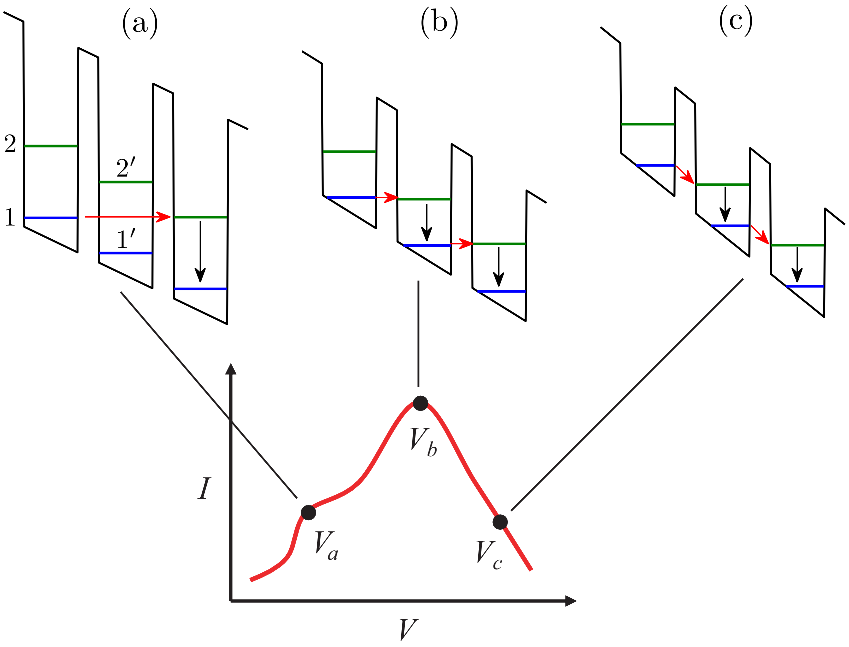

FIGURE 2.8: Schematic illustration of the proposal of Kazarinov and Suris [1] to obtain light amplification from a semiconductor superlattice. We show a hypothetical I-V for this device, along with the conduction band diagrams and the location of the subbands in energy space under different bias conditions. Electron transport in the electrically-pumped structure is due to resonant tunneling.

Due to the fast nonradiative transition to the ground state in which an LO phonon is emitted, the ground state has a larger population than the excited state for any bias. When the bias applied to the structure is changed, the ground state of a quantum well may align with the excited state of another quantum well. For example, when a bias V_a is applied, the ground state of the n-th quantum well aligns with the excited state of the (n+2)-th quantum well; leading to a peak in the I-V characteristics. However, the current flow reaches its maximum when the ground state of n-th quantum well aligns with the excited state of the (n+1)-th quantum well, which occurs when $V = V_b$. At biases larger than V_b, the interaction between the ground state and the excited state of the adjoining well is sufficient to lead to coherent electric-dipole oscillations diagonally across the barrier. Light amplification at $\hbar\omega = E_{12'}$, where $2'$ is the excited state in the $(n+1)$-th quantum well, can be obtained since a population inversion is maintained between levels 1 and $2'$ due to the short lifetime of level $2'$ ($\ll 1$ ps), and the long lifetime of level 1 ($\sim$ 1–10 ps depending on the thickness and height of the barriers between the quantum wells). Moreover, the energy of the radiative transition $E_{12'}$ may be tuned by changing the bias over a relatively wide range.

Motivated by Kazarinov and Suris's proposal [1], intense research was carried out in the 1980s to study electrical transport phenomena in semiconductor superlattices. However, the proposed idea was not practical in its original form. Kazarinov and Suris [1] originally proposed to use undoped superlattices, which meant that electrons were to be injected in the periodic structure from the contact regions at the ends of the superlattice. Injected electrons in this way leads to formation of space charge domains across the structure and prevents the development of a homogeneous static electric field, ultimately leading to electrical instability in the device. This problem, which is due to the unipolar nature of the device and the specific electrical-pumping scheme, can be solved by doping the superlattice within each of its periods, such that the positive charges on the ionized donors compensate for the steady-state electron population within each quantum well. However, this device has yet another problem. The operating bias point for a photon-assisted tunneling transport mechanism at V_c is beyond the peak-current bias at V_b, which is in a negative-differential resistance (NDR) region on the I-V curve. An NDR region is inherently unstable for an electrically-pumped superlattice that has multiple repeated modules, since the modules separate into high-field domains in an NDR region [6, 105]. This separation occurs because there is no mechanism that can enforce a homogeneous field distribution across the structure, and complex nonlinear charge oscillations occur in the NDR. Hence, even though a population inversion is guaranteed at the bias V_c, the superlattice cannot be biased at that point. It may be noted that even though a single quantum well structure could be electrically biased in the NDR, a superlattice with multiple quantum wells is almost necessary to achieve sufficient intersubband gain for lasing.

While resonant-tunneling through a double barrier was observed as early as 1974 [106], attesting to the high quality of molecular beam epitaxy (MBE) already achieved at that time, it took several years before Capasso *et al.* [2] were able to observe sequential resonant-tunneling through a semiconductor superlattice in 1985. Part of the reason for this delay was the inherent difficulty in electrically biasing a superlattice beyond the NDR regions. To ensure a rigorously controlled and spatially homogeneous electric field throughout the structure, the superlattice was placed in the i region of a reverse-biased p^+-i-n^+ junction [2]. This scheme was critical to the success of their experiment since it prevented domain formation in the NDR regions of the I-V curve. In Fig. 2.9, we show a schematic illustration of that structure and a qualitative sketch of the low-temperature I-V curve, similar to the one that was actually measured. The peaks corresponding to the two dominant resonant-tunneling transitions were clearly resolved in the experiment [2], providing evidence of the high quality of the material growth and paving the way for unique device applications based on resonant-tunneling phenomena in semiconductor superlattices.

Multiple proposals to achieve intersubband lasing were considered in the late 1980s and early 1990s [107]. The structure of Capasso *et al.* [2], based on the schematic illustration in Fig. 2.9, merits further discussion since it bears the closest resemblance to the first superlattice-based intersubband laser, i.e. the QCL, that was invented a few years later [7]. In their subsequent paper [108], the authors considered the idea of achieving population inversion between levels 2 and 3 within the same well. At the 1-3$'$ resonance (bias point V_b) in Fig. 2.9, the second excited state 3$'$ in the $(n+1)$-th well is selectively populated by the ground state 1 of the n-th well through resonant-tunneling. If a population inversion is established between levels 3 and 2 in a well, stimulated emission is possible through a vertical intrawell radiative transition. It may be noted that this scheme differs significantly

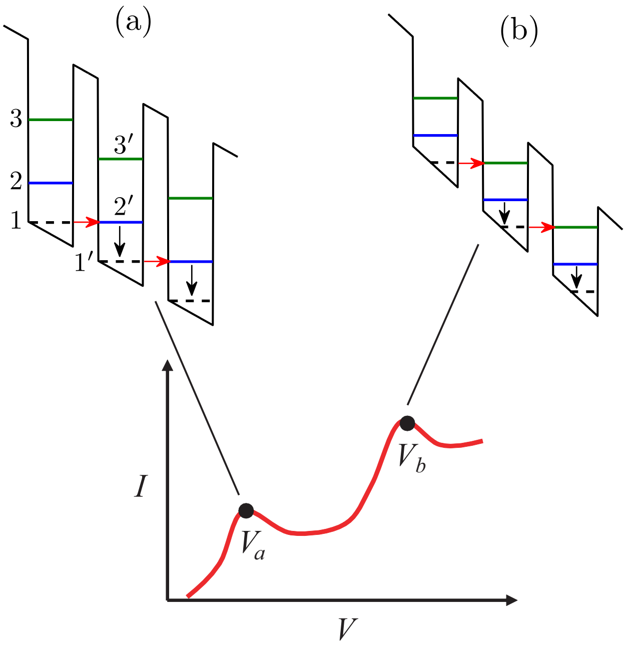

FIGURE 2.9: First observation of sequential resonant-tunneling in a semiconductor ($In_{0.53}Ga_{0.47}As/In_{0.52}Al_{0.48}As$) superlattice with 35 periods [2]. Conduction band schematic illustrations corresponding to two different bias points in the I-V curve are shown. The I-V curve shown here is a qualitative sketch of the measured I-V curve in [2]. Note that at all biases, the ground state 1 in the quantum wells will have the largest population due to fast electron-LO phonon scattering from levels 3 → 2, 3 → 1, and 2 → 1.

from the original Kazarinov and Suris proposal shown in Fig. 2.8, where the radiative transition is an interwell diagonal transition. However, as Capasso *et al.* [108] noted, it is difficult to obtain population inversion with this scheme because of fast (sub-ps) electron-LO-phonon scattering times between levels 3 → 2, 3 → 1, and 2 → 1.

The electron-LO phonon scattering matrix element for two dimensional subbands is proportional to $1/|\Delta k|$, where $|\Delta k|$ is the momentum exchanged in the scattering process [107]. If the subbands in the scheme of Fig. 2.9 are designed with an energy spacing such that $E_{32} \gg \hbar\omega_{\mathrm{LO}}$, the momentum exchange required for an electron-LO phonon scattering event from level 3 → 2 or 3 → 1 is an order of magnitude greater than it is from level 2 → 1, where $E_{21} \approx \hbar\omega_{\mathrm{LO}}$, so that the scattering matrix element is significantly reduced. This reduction is necessary to

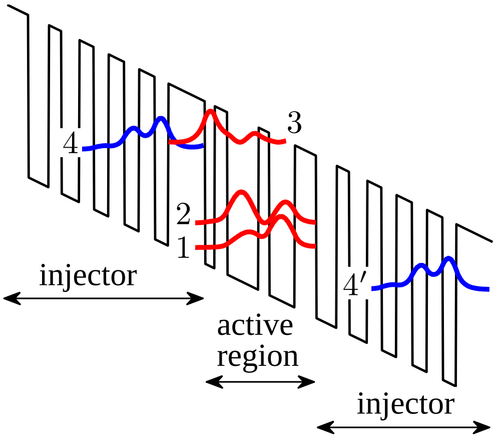

FIGURE 2.10: Conduction band diagram and modulus-squared wavefunctions of a GaAs/AlGaAs quantum cascade laser. Levels 1–3 are in the active region and level 4 is the ground level in the injector. Level 4′ is the ground level in the next injector.

obtain inversion.

2.4.3 A Typical Quantum Cascade Laser Structure

Despite the fast carrier relaxation between the subbands in the conduction band, a population inversion that ultimately allows laser action can be achieved between these states by means of "band-structure engineering" [109]. By engineering the thicknesses of the quantum wells and by properly choosing the materials for the wells and the barriers, it is possible to manipulate the fundamental properties of the electronic states, carrier scattering rates, optical dipole matrix elements, and the tunneling rates of carriers from one state to another through the barriers. With an engineered multiquantum well structure, the "quantum engineer" may optimize the population inversion and gain at a desired emission wavelength.

In Fig. 2.10, we show the conduction band diagram of a typical quantum cascade laser when an external bias is applied. Typical quantum cascade lasers consist of 20–30 periods, each of which contains an injector region and an active region. To minimize space-charge effects caused by carrier injection under applied bias, the injector region is n-type doped. The doping concentration per period is typically 2–4 $\times$ 10^{11} cm^{-2}. Here, the active region acts as a three-level laser system. Four-level active regions are also used in QCLs [110]. To achieve population inversion between subband 3 and subband 2, the active region is designed so that the energy separation between subband 2 and subband 1 is nearly resonant with the LO phonon energy. Hence, intersubband relaxation from subband 2 to subband 1 by emission of LO phonons is strongly enhanced, resulting in a lifetime of subband 2 on the order of $\tau_2 \approx 0.3$ ps, while the lifetime of subband 3 is typically $\tau_3 > 1$ ps. Electrons leave the active region by tunneling through a thin exit barrier into the following injector region. The injector region acts as an electron reservoir. It is a superlattice that typically consists of 5–7 quantum wells. It is designed so that with an applied bias the coupling between adjacent quantum wells leads to the formation of minibands, which ensures an efficient carrier transport. The minigap in the injectors prevents electrons residing in the upper laser subband 3 from leaking into the continuum states. A crucial point is the carrier injection from the injector into the upper laser subband 3 in the active region. With an appropriate bias, the injector subband 4 becomes resonant with subband 3. This leads to an efficient carrier injection via resonant tunneling. However, the very high carrier density in the injector leads to high carrier-carrier scattering rates, resulting in a strong damping of the coherent wavepacket propagation and, thus, a less efficient carrier injection. We will discuss this point in more detail in Chapter 5.

Chapter 3

Self-Induced Transparency Modelocking of Quantum Cascade Lasers

3.1 Introduction

In quantum cascade lasers (QCLs), the light is generated by a transition between two subbands in the conduction band, in contrast to interband semiconductor lasers, in which the light is generated by a recombination of an electron-hole pair. Two subbands in the conduction band have approximately same curvature in the energy-momentum relation, while the conduction and valence bands have opposite curvatures, as shown in Fig. 2.7. As a consequence, QCLs have narrow linewidths and long coherence times T_2 compared to interband lasers. In QCLs, values of T_2 on the order of 100 fs are achievable [30]. The coherence time is mainly determined by intrasubband electron-electron, electron-LO phonon, and electron-interface roughness scattering [111, 112]. Another important feature of the QCLs is their rapid gain recovery times T_1 compared to inter-band semiconductor lasers, due to fast carrier transport through quantum cascade structure by coherent tunneling and incoherent scattering mechanisms [31]. Typical values of T_1 are in the range 1–10 ps, which is short compared to T_{rt}, the round-trip time in the cavity. Typical values of T_{rt} are on the order of 50 ps.

The narrow linewidths and fast recovery times of QCLs make it difficult to achieve conventional passive modelocking. Gain bandwidths that are significantly larger than the pulse bandwidths are required, and that is hard to obtain when the linewidths are narrow, as in QCLs. A saturable gain with a recovery time that is long compared to T_{rt} is also required for conventional modelocking in order to suppress continuous waves, and the typical gain recovery times in QCLs are shorter than the round-trip times. Thus, conventional passive modelocking cannot work in QCLs that operate in a standard parameter regime.

Self- or passive modelocking of lasers [61, 113] was discovered experimentally at almost the same time as SIT, and there was speculation that the modelocking was due to SIT [114, 115]. However, subsequent work made it clear that SIT could not account for the observed modelocking [116, 117]. Conventional passively modelocked system operate in regimes in which the pulse bandwidth is smaller than the gain bandwidth, so that typically coherence times T_2 are short compared to the pulse duration. With the development of the standard theory of passive modelocking [63, 64], work on SIT modelocking almost ceased. An exception is work by Kozlov [118], who pointed out the importance for SIT modelocking of including an absorbing medium, in which the pulse is a 2π pulse, along with a gain medium in which the pulse is a π pulse. The absorbing medium acts as a saturable absorber, suppressing the generation of continuous waves and the Risken-Nummedal-Graham-Haken instability [33].

We have found that QCLs are an ideal tool to realize SIT modelocking [119, 120]. We proposed that absorbing periods should be interleaved with the gain periods as shown in Fig. 3.1 and that absorbing periods should have a dipole moment approximately twice as large as the dipole moment in the gain periods. Therefore, the π pulses in the gain periods become 2π pulses in the absorbing periods. As in standard QCLs with just gain periods, the electrons are injected into the upper resonant levels in the gain periods, to produce gain. However, electrons are injected into the lower resonant levels in the absorbing periods, so that the light pulses experience SIT in the absorbing medium (see Fig. 3.2). We have found analytical modelocked solutions when there is no frequency detuning, the absorbing periods have a dipole moment twice that of the gain periods, the input pulse is a π pulse in the gain medium, and the gain recovery times in the gain and the absorbing periods are much longer than the coherence time T_2 and are short compared to the round-trip time. However, the analytical results are only of practical interest if they continue to hold under realistic circumstances. In practice, gain recovery times in a QCL are on the order of a ps, the population inversion in both the gain and absorbing periods will be incomplete, and the initial pulse will have an energy that does not correspond exactly to a π pulse, and an initial pulse duration that is on the order of a ps. Therefore, we computationally solved the Maxwell-Bloch equations and carried out an extensive parameter study. We determined the stability regimes for SIT modelocking, and our results showed that SIT modelocking for QCLs is robust [119–121].

In this chapter, we will discuss the physics of SIT modelocking in QCLs using two-level models for the gain and absorbing periods; we will present analytical modelocked solutions of the Maxwell-Bloch equations in special cases that describe the dynamics of a QCL having both gain and absorbing periods; we will derive conditions for stable modelocked pulses. We will then solve the Maxwell-Bloch equations computationally for more general cases and determine the stability limits of all key parameters for stable modelocking. We will show that SIT modelocking is stable for a broad regime when the parameters are varied around the typical values for conventional QCLs.

3.2 Physical Picture of SIT Modelocking

In order to obtain SIT modelocking, it is necessary to have two highly-coherent resonant media with nearly equal resonant frequencies. In one medium, denoted the gain medium, electrons should be injected into the upper lasing state so that the resonant states are nearly inverted. In the other medium, denoted the absorbing medium, electrons should be injected into the lower state so that the resonant states are not inverted. Also, the dipole strength in the absorbing medium should be nearly equal to twice the dipole strength in the gain medium. At the same time, the ratio of the gain per unit length to the absorption per unit length should be small enough so that the growth of continuous waves is suppressed, but large enough so that a modelocked pulse can stably exist. It is possible to simultaneously satisfy all these conditions by interleaving gain and absorbing periods that have the required dipole strengths as shown schematically in Fig. 3.1. By appropriately choosing the number of gain periods and the number of absorbing periods, one can in principle obtain any desired ratio for the gain and absorption per unit length. As long as there are many periods within the transverse wavelength of the lasing mode, the gain and absorbing periods will experience the same light intensity.

In Fig. 3.2, we show simplified two-level resonant structures for the gain and absorbing media. In the gain medium, electrons are injected into level 2g and are extracted from level 1g. The carrier lifetime in 2g should be longer than the modelocked pulse duration, and the equilibrium population inversion should be nearly complete. When an optical pulse with a photon energy equal to the resonant energy impinges on the gain medium with its polarization oriented in the direction perpendicular to the layers, electrons scatter to level 1g and photons are emitted. Then, the electrons are nonradiatively extracted from level 1g. In the absorbing medium, electrons are injected into the lower level 1a. The lifetime of state 1a should again be longer than the pulse duration. When a light pulse of the appropriate wavelength and polarization impinges on the absorbing medium, photons are absorbed and electrons scatter to level 2a. If a light pulse is sufficiently

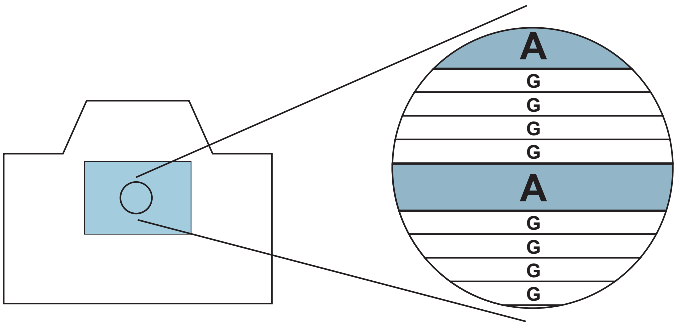

FIGURE 3.1: Schematic illustration of a QCL structure with gain and absorbing periods. On the left, we show a cutaway view of QCL structure. The active region is shown as a filled-in rectangle. We are looking in the direction along which light would propagate. Electrodes would be affixed to the top and bottom, so that electrons flow vertically. The heterostructure would also be stacked vertically as shown on the right. We show one absorbing period for every four gain periods, corresponding schematically to the case in which the electron density in the gain periods (N_g) $\simeq$ 4×the electron density in the absorbing periods (N_a), and we show absorbing periods that are twice as large as gain periods to indicate schematically that the dipole moment in the absorbing periods (μ_a) $\simeq$ 2×the dipole moment in the gain periods (μ_g).

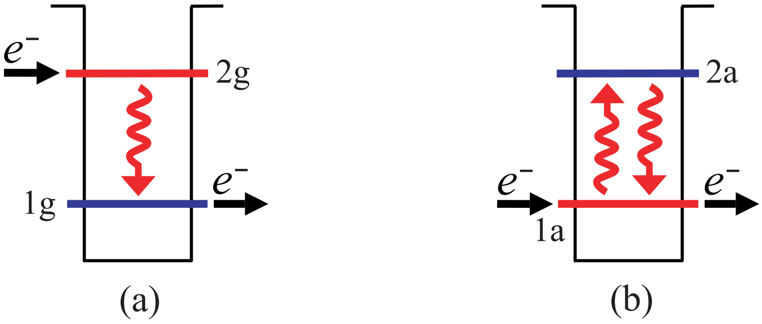

FIGURE 3.2: Schematic illustration of the (a) gain and (b) absorbing media. Black straight-line arrows indicate the direction of electron flow. Red wavy arrows indicate radiative transitions.

intense, then photons are re-emitted with no overall loss in one Rabi oscillation. In order for these processes in the gain medium and absorbing medium to occur simultaneously, the energy spacing between the resonant levels should be nearly the same in both media.

In the theory of resonant two-level media, both π pulses and 2π pulses play an important role [122]. A π pulse is a pulse with sufficient energy to exactly invert the lower state population of a two-level medium if the medium is initially

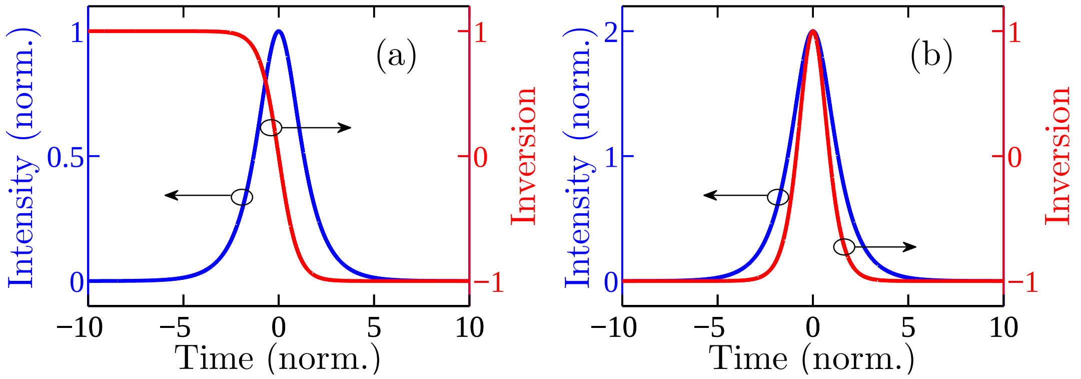

FIGURE 3.3: (a) Electric field and population inversion profile in the presence of a π pulse. An initially inverted medium becomes completely uninverted. (b) Electric field and population inversion in presence of a 2π pulse. An initially uninverted medium first becomes inverted and then becomes uninverted again. In both cases, the intensity has been normalized by the peak of the π pulse and the time has been normalized by the (full width half maximum) / 1.763 duration of the pulse.

uninverted, or, conversely, to uninvert the upper state if the medium is initially inverted, as shown in Fig. 3.3(a). In the former case, the pulse experiences loss and rapidly attenuates, but, in the latter case, the pulse experiences gain. The pulse duration is approximately half a Rabi oscillation period. If a pulse lasts a longer time than required to drive the population from the upper level to the lower, then the medium will amplify the first part of the pulse and attenuate the latter part, in a way that shortens the pulse. Conversely, if a pulse is initially too short, it is lengthened. Because a π pulse experiences gain, it is natural that shortly after the initial observations of passive modelocking in lasers, it was proposed that the pulses in these lasers are actually SIT-induced π pulses [114, 115]. However, these pulses are not suitable for use on their own as passively modelocked laser pulses. Where one π pulse can exist, there is nothing to prevent continuous waves from generating multiple pulses, leading to chaos rather than a single stable pulse oscillating in a laser cavity.

One can in principle circumvent this difficulty by combining a gain medium in which the optical pulse is a π pulse with an absorbing medium in which the optical pulse is a 2π pulse [118]. A 2π pulse is a pulse with sufficient energy so that in an uninverted medium the lower state population is first inverted and then returned to the lower state in approximately one Rabi oscillation, as shown in Fig. 3.3(b). Like a π pulse, a 2π pulse is stable. If its initial duration is too long, the duration decreases, and, if its initial duration is too short, the duration increases. The 2π pulse propagates through the medium without loss, in contrast to continuous waves at the resonant optical frequency, which experience loss. This remarkable property is what led to the name "self-induced transparency" [39, 40]. Because of this property, the absorbing medium acts like the saturable loss in a conventional passively modelocked system, suppressing the growth of continuous waves, while allowing a short pulse to propagate.

It is evidently important that both the gain medium and the absorbing medium act on the optical pulse simultaneously. We may achieve this simultaneous interaction by designing a QCL structure that has the gain and absorbing periods interleaved along the growth axis of the structure, as shown in Fig. 3.1. By making the dipole moment in the absorbing periods twice that of the gain periods, a π pulse in the gain periods is a 2π pulse in the absorbing periods. Therefore, an injected π pulse completely depletes the gain medium as it makes its way through the QCL, whereas, the absorbing medium becomes transparent. We will show that by controlling the amount of gain and absorption per unit length in the gain and absorbing media, pulse durations can be controlled.

In order to suppress spatial hole burning, the RNGH instability, or the growth of multiple pulses, we do not want continuous waves to grow in an SIT modelocked laser. The absorption parameter should be large enough to keep the laser operating below the threshold for the growth of continuous waves. Therefore, the laser cannot self-start, and it is necessary to use external means to start the modelocking. Essentially, we need a seed pulse that has sufficient energy and a duration on the order of T_1. We suggest two optical approaches. First, we can seed the pulse from an external source by injection-locking, or, second, we can use active modelocking to generate an initial pulse that will have a suitable energy and initial duration for SIT modelocking. It may also be possible to use a mechanical or an electrical impulse to start the modelocking.

3.3 Maxwell-Bloch Equations

Wang *et al.* [28] and Gordon *et al.* [29] have observed evidence for Rabi oscillations and the RNGH instability in QCLs that only have gain periods. They demonstrated that the two-level Maxwell-Bloch equations [122, 123] apply to QCLs in some parameter regimes, although they also showed that saturable absorption affects the behavior quantitatively, significantly reducing the RNGH threshold. They attributed the saturable absorption to Kerr lensing that increases the mode overlap with the active region and reduces the losses in the cladding. These effects depend sensitively on the details of the QCL geometry. They also observed that spatial hole burning due to the interaction of forward- and backward-propagating waves has an important effect on the pulse spectrum. They did not find it necessary to include chromatic dispersion or other nonlinearities. Motivated by these results, we started by using a simple two-level model based on the standard one-dimensional Maxwell-Bloch equations [122, 123] for the analysis of our proposed SIT modelocking in QCLs. However, we extended our model to include the saturable nonlinearity and chromatic dispersion, and we will discuss their effects on SIT modelocking of QCLs in Chapter 8. The Maxwell-Bloch equations that describe the light propagation and light-matter interaction in a QCL having interleaved gain and absorbing periods may be written as

$$\frac{n}{c}\frac{\partial E}{\partial t} = -\frac{\partial E}{\partial z} - i\frac{kN_g\Gamma_g\mu_g}{2\epsilon_0 n^2}\eta_g - i\frac{kN_a\Gamma_a\mu_a}{2\epsilon_0 n^2}\eta_a - \frac{1}{2}lE, \tag{3.1a}$$

$$\frac{\partial \eta_g}{\partial t} = \frac{i\mu_g}{2\hbar}\Delta_g E - \frac{\eta_g}{T_{2g}}, \tag{3.1b}$$

$$\frac{\partial \Delta_g}{\partial t} = \frac{i\mu_g}{\hbar}\eta_g E^* - \frac{i\mu_g}{\hbar}\eta_g^* E + \frac{\Delta_{g0} - \Delta_g}{T_{1g}}, \tag{3.1c}$$

$$\frac{\partial \eta_a}{\partial t} = \frac{i\mu_a}{2\hbar}\Delta_a E - \frac{\eta_a}{T_{2a}}, \tag{3.1d}$$

$$\frac{\partial \Delta_a}{\partial t} = \frac{i\mu_a}{\hbar}\eta_a E^* - \frac{i\mu_a}{\hbar}\eta_a^* E + \frac{\Delta_{a0} - \Delta_a}{T_{1a}}, \tag{3.1e}$$

where the subscripts g and a in Eq. (3.1) refer to quantities in the gain and absorbing periods, respectively. The independent variables z and t are length along the light-propagation axis of the QCL and time. The dependent variables E, η, and Δ denote the envelopes of the electric field, polarization, and inversion. The parameter μ denotes the dipole moment between the resonant levels. The parameters Δ_{g0} and Δ_{a0} denote the equilibrium inversion away from the modelocked pulse. The parameters n and c denote the index of refraction and the speed of light. The parameters N and Γ denote the electron density and the overlap factor of the optical mode with the active region. The parameters k, l, ϵ_0, and $\hbar$ denote the wavenumber in the active region, the linear loss including the mirror loss, the vacuum dielectric permittivity, and Planck's constant. The notation closely follows that of Wang *et al.* [28] and Gordon *et al.* [29], with the differences that we have an absorbing as well as a gain medium, and we are considering uni-directional propagation, as is often done in the literature to study the evolution of modelocked pulses [27].

3.4 Analytical Solutions and Stability Limits

Assuming that T_{1g} and T_{1a} are large enough so that they may be set equal to ∞ in Eqs. (3.1c) and (3.1e), and focusing on the special case in which $\mu_a = 2\mu_g$ and the pulse is a π pulse in the gain medium, Eq. (3.1) has an exact analytical solution that we may write

$$E = \frac{\hbar}{\mu_g \tau} \operatorname{sech} x, \tag{3.2a}$$

$$\eta_g = \frac{iB_g}{2} \Delta_{g0} \operatorname{sech} x, \tag{3.2b}$$

$$\Delta_g = B_g \Delta_{g0} \left(\frac{\tau}{T_{2g}} - \tanh x \right), \tag{3.2c}$$

$$\eta_a = \frac{iB_a}{2} \Delta_{a0} \left(-\operatorname{sech} x \tanh x + \frac{\tau}{3T_{2a}} \operatorname{sech} x \right), \tag{3.2d}$$

$$\Delta_a = \frac{B_a}{2} \Delta_{a0} \left(1 + \frac{\tau^2}{3T_{2a}^2} \right) - B_a \Delta_{a0} \left(\operatorname{sech}^2 x + \frac{2\tau}{3T_{2a}} \tanh x \right), \tag{3.2e}$$

where

$$x = \frac{t}{\tau} - \frac{z}{v\tau}. \tag{3.3}$$

We also set

$$B_g = \frac{1}{1+\tau/T_{2g}} \qquad \text{and} \qquad B_a = \frac{2}{(1+\tau/3T_{2a})(1+\tau/T_{2a})}, \tag{3.4}$$

so that $\Delta_g \to \Delta_{g0}$ and $\Delta_a \to \Delta_{a0}$ as $t \to -\infty$, and the equilibrium population completely recovers on every pass of the pulse through the laser. Hence, Eq. (3.2) shows that stable modelocked operation can be achieved in QCL structures that satisfy the SIT modelocking requirements.

The following governing equations can be derived for the parameters τ and v that correspond to the pulse duration and the pulse velocity, respectively, by substituting Eqs. (3.2a), (3.2b), and (3.2d) in Eq. (3.1a):

$$\frac{\tau/T_{2g}}{1+\tau/T_{2g}} g\Delta_{g0} + \frac{\tau^2/3T_{2a}^2}{(1+\tau/T_{2a})(1+\tau/3T_{2a})} a\Delta_{a0} - l = 0 \tag{3.5}$$

and

$$\frac{1}{v} = \frac{n}{c} - a\tau \frac{\tau/2T_{2a}}{(1+\tau/T_{2a})(1+\tau/3T_{2a})} \Delta_{a0}. \tag{3.6}$$

The full-width at half-maximum (FWHM) pulse duration τ_{FWHM} equals 1.763τ. We now consider in more detail the special case $T_{2g} = T_{2a} \equiv T_2$. Writing $\bar{g} = g/l$, $\bar{a} = a/l$, and $\bar{\tau} = \tau/T_2$, we find that the equation for the pulse duration becomes

$$\frac{3}{\bar{\tau}} = \frac{3\bar{g}\Delta_{g0} - 4}{2} + \left[\left(\frac{3\bar{g}\Delta_{g0} - 4}{2} \right)^2 + 3(\bar{g}\Delta_{g0} + \bar{a}\Delta_{a0} - 1) \right]^{1/2}. \tag{3.7}$$

Equation (3.7) only has a solution when $\bar{a} < (3\bar{g}\Delta_{g0} - 2)^2/12|\Delta_{a0}|$, where we note that $\Delta_{a0} < 0$.

In order to achieve SIT modelocking, the growth of continuous waves must be suppressed. In order to suppress continuous waves, the gain must be below threshold. To derive this condition, we set $\Delta_g = \Delta_{g0}$ and $\Delta_a = \Delta_{a0}$ in steady state, where there is no evolution in z. We then find from Eqs. (3.1b) and (3.1d),

$$\eta_g = i\frac{\mu_g}{2\hbar}T_{2g}\Delta_{g0}E, \quad \eta_a = i\frac{\mu_a}{2\hbar}T_{2a}\Delta_{a0}E, \tag{3.8}$$

where we are considering continuous waves, so that there is no dependence on t and the t-derivatives vanish. After substitution in Eq. (3.1a), we obtain in steady state

$$\frac{kN_g\Gamma_g\mu_g^2T_{2g}\Delta_{g0}}{2\epsilon_0 n^2\hbar} + \frac{kN_a\Gamma_a\mu_a^2T_{2a}\Delta_{a0}}{2\epsilon_0 n^2\hbar} - l = 0, \tag{3.9}$$

which may also be written $g\Delta_{g0} + a\Delta_{a0} - l = 0$, where

$$g = \frac{kN_g\Gamma_g\mu_g^2T_{2g}}{2\epsilon_0 n^2\hbar}, \quad a = \frac{kN_a\Gamma_a\mu_a^2T_{2a}}{2\epsilon_0 n^2\hbar}. \tag{3.10}$$

Physically, the parameter g corresponds to the gain per unit length from the gain periods of the QCL, and the parameter a corresponds to the absorption per unit length from the absorbing periods. The condition for the linear gain to remain below threshold is $g\Delta_{g0} + a\Delta_{a0} - l < 0$. In the case of a fully inverted gain medium, so that $\Delta_g = \Delta_{g0} = 1$ and a fully uninverted absorbing medium so that $\Delta_a = \Delta_{a0} = -1$, the condition to suppress continuous waves becomes $g - a - l < 0$. Writing $\bar{g} = g/l$, $\bar{a} = a/l$, and $\bar{\tau} = \tau/T_2$, we find that the condition to suppress the growth of continuous waves becomes $\bar{g}\Delta_{g0} + \bar{a}\Delta_{a0} - 1 < 0$.

The conditions for stability may be summarized,

$$\frac{(\bar{g}\Delta_{g0} - 1)}{|\Delta_{a0}|} < \bar{a} < \frac{(3\bar{g}\Delta_{g0} - 2)^2}{12\ |\Delta_{a0}|}. \tag{3.11}$$

When $\bar{a}$ is above the upper limit in Eq. (3.11), we have found by solving Eq. 3.1 computationally that an initial pulse damps away. When $\bar{a}$ is below the lower limit, continuous waves grow, we have computationally found that multiple pulses are generated [120].

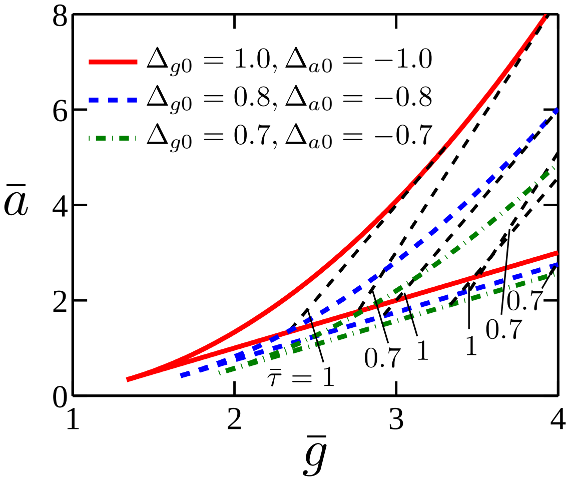

FIGURE 3.4: Stability limits of the normalized absorption ($\bar{a}$) vs. the normalized gain ($\bar{g}$) coefficients with different values of Δ_{g0} and Δ_{a0}. The ratio T_1/T_2 is infinite in all cases. For a given $\bar{\tau}$ and $\bar{a}$, the required $\bar{g}$ increases as Δ_{g0} and $|\Delta_{a0}|$ decrease.

Equation (3.11) defines a parameter regime in which stable modelocked operation is possible. In Fig. 3.4, we present the stability limits when the population inversion in the gain and absorbing periods vary. In all cases, the lower lines indicate the limiting values for $\bar{a}$, below which continuous waves grow, and the upper lines indicate the limiting values for $\bar{a}$, above which initial pulses damp. Figure 3.4 shows that the minimum value of $\bar{g}$ that is required for stable operation increases when Δ_{g0} decreases and Δ_{a0} increases by the same amount. There is also a slight decrease in the lower limit for $\bar{a}$ and a larger decrease in the upper limit. Since the upper limit drops more than the lower limit, the stable parameter region becomes smaller. We also show contours of the pulse duration, normalized by the coherence time T_{2g}, denoted $\bar{\tau}$, as given by Eq. (3.7). Pulse durations are approximately on the order of T_{2g} when $\bar{g} \approx 2.5$ and $\bar{a} \approx 2.0$. We also note that pulses become shorter as $\bar{g}$ and $\bar{a}$ increase. However, both $\bar{g}$ and $\bar{a}$ are directly proportional to the current; so, to increase the gain and absorption in a fixed ratio, one must increase the current. At the same time, we note that $\bar{g}$ and $\bar{a}$ are directly proportional to T_2. Hence, it is possible to reduce the required current by increasing T_2.

We have studied what happens to the stability limits if T_{2a}/T_{2g} vary, and we show the results in Fig. 3.5. In Fig. 3.5, we have varied T_{2a} keeping T_{2g} constant.

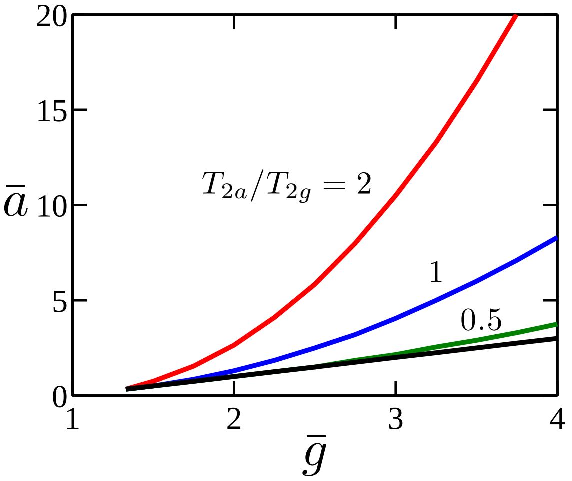

FIGURE 3.5: Stability limits of the normalized absorption ($\bar{a}$) vs. the normalized gain ($\bar{g}$) coefficients with different values of T_{2a}/T_{2g}. We set $T_{1g} = T_{1a} = \infty$ in all cases. At equilibrium, the gain medium is completely inverted, i.e., $\Delta g0 = 1.0$, and the absorbing medium is completely uninverted, i.e., $\Delta_{a0} = -1.0$.

In a QCL, typical values of T_{2g} and T_{2a} are on the order of 100 fs. A change in T_{2a} affects the stability limits more than does a change in T_{2g}, as is evident from Eq. (3.5). When T_{2a}/T_{2g} increases, the upper stability limits increase. When $\bar{g} = 4.0$, we find that the upper limit for $\bar{a}$ varies from 3.75 to 8.3 to 24 as T_{2a}/T_{2g} varies from 0.5 to 1.0 to 2.0. The lower limit for $\bar{a}$ remains unchanged.

We now derive an energy-balance equation that describes the energy input limits for stable operation when $\tau \ll T_2$. We define $\Theta(z,t) = \int_{-\infty}^{t} E(z,t')\,dt'$. Then, Eqs. (3.1b) and (3.1c) may be written as

$$\frac{\partial \eta_g(z,t)}{\partial t} = \frac{i\mu_g}{2\hbar}\Delta_g(z,t)\frac{\partial \Theta(z,t)}{\partial t} \tag{3.12}$$

and

$$\frac{\partial \Delta_g(z,t)}{\partial t} = 2\frac{i\mu_g}{\hbar}\eta_g(z,t)\frac{\partial \Theta(z,t)}{\partial t}. \tag{3.13}$$

In the gain medium, the polarization and population inversion may be written in terms of a single angle α as $2i\eta_g = \cos\alpha$ and $\Delta_g = \sin\alpha$. We integrate both sides of Eq. (3.12) or Eq. (3.13), after substituting these expressions for η_g and Δ_g and assuming that $\Delta_g(z, t \to -\infty) = 1$. We then obtain $\alpha(z,t) = \pi/2 + (\mu_g/\hbar)\Theta(z,t)$.

We may similarly write $2i\eta_a = \cos\beta$ and $\Delta_a = \sin\beta$ in the absorbing medium, and we then find $\beta(z,t) = -\pi/2 + (\mu_a/\hbar)\Theta(z,t)$, where we have set $\Delta_a(z, t \to -\infty) = -1$. We now consider Eq. (3.1a) in steady state, where there is no evolution in z, and in the limit $t \to \infty$, where there is no evolution in t. We also define a normalized pulse energy

$$\bar{\theta}(z) = (\mu_g/\hbar)\Theta(z, t \to \infty). \tag{3.14}$$

Equation (3.1a) now becomes

$$g \sin[\bar{\theta}(z)] = a\,\frac{\mu_g}{\mu_a}\,\frac{T_{2g}}{T_{2a}}\,\sin\left[\frac{\mu_a}{\mu_g}\bar{\theta}(z)\right], \tag{3.15}$$

where we note that the linear loss may be neglected in the limit $\tau \ll T_2$. In the special case $\mu_a = 2\mu_g$ and $T_{2g} = T_{2a} \equiv T_2$, we find $a(\mu_g/\mu_a)(T_{2g}/T_{2a})\sin[(\mu_a/\mu_g)\bar{\theta}] = a\cos\bar{\theta}\sin\bar{\theta}$, so that Eq. (3.15) becomes $\cos\bar{\theta} = g/a$, which defines the limits of the input energy that is required to generate a single pulse,

$$\cos^{-1}(g/a) < \bar{\theta} < 2\pi - \cos^{-1}(g/a). \tag{3.16}$$

When the initial value of $\bar{\theta}$ is within these limits, a single pulse with a final value of $\bar{\theta} = \pi$ is generated. When the initial value of $\bar{\theta}$ is below this value, the lower limit in Eq. (3.16), the initial pulse damps. When the initial value of $\bar{\theta}$ is above the upper limit, the initial pulse splits into multiple pulses.

In the analysis up to now it has been assumed that the central carrier frequency of the light pulse and the transition frequency in both the gain and absorbing media are the same. Since the frequency of the light is largely determined by the gain medium, it is reasonable to assume that there is no detuning between the light and the gain medium. Even if the modelocking is seeded by injection-locking, as in the experiment of Choi *et al.* [124], the injection-locking laser can be tuned to the gain resonance. In principle, there may be a small detuning between the gain and absorbing media due to design or growth issues; however, it is possible to design the gain and absorbing media so that detuning is nearly absent. QCLs are currently being grown with high accuracy and experimentally-observed wavelengths agree closely with the designed values.

If there is a detuning of Δ_ω between the gain and the absorbing periods and the light pulses are tuned to the gain periods, as would normally occur in a laser, then Eq. (3.1d) becomes

$$\frac{\partial \eta_a}{\partial t} = \frac{i\mu_a}{2\hbar} E \Delta_a - \left(\frac{1}{T_2} - i\Delta_\omega \right) \eta_a. \tag{3.17}$$

Analytical solutions for η_a and Δ_a may be found in presence of detuning Δ_ω when $\tau \ll T_2$, so that the term proportional to $1/T_2$ may be neglected in the polarization equation. In this case, the solutions become

$$\eta_a = \frac{\Delta_\omega \tau}{1 + (\Delta_\omega \tau)^2} \operatorname{sech} x + i \frac{1}{1 + (\Delta_\omega \tau)^2} \operatorname{sech} x \tanh x, \tag{3.18}$$

$$\Delta_a = -1 + \frac{2}{1 + (\Delta_\omega \tau)^2} \operatorname{sech} x, \tag{3.19}$$

where $x = t/\tau - z/v\tau$ and $\Delta_{a0} = -1$ at $t \to -\infty$.

On physical grounds, it is apparent that the criterion for acceptable detuning is that $\Delta_\omega \lesssim 1/T_2$, since $\tau \lesssim T_2$ and the bandwidth of the pulse in angular frequency is $\sim \tau^{-1}$. If T_2 is 100 fs, and we demand conservatively that $\Delta_\omega < 0.1/T_2$, then $\Delta_\omega \lesssim 10^{12}$ s^{-1}, corresponding to an allowed frequency detuning of 1.6×10^{11} Hz, which is 2% of the carrier frequency of 8 μm light and is not overly demanding. We have found a more exact criterion computationally that we will present shortly.

3.5 Computational Analysis

In order for the solution reported in Eq. (3.2) to be of any practical interest, it must be robust when μ_a differs from $2\mu_g$, when T_{1g} and T_{1a} are on the order of a picosecond or less, when an initial pulse that is long compared to its final, stable duration is injected into the medium, and when the initial pulse area differs from the ideal value of π in the gain medium and 2π in the absorbing medium. The Maxwell-Bloch equations must be solved computationally to determine what happens under these conditions. For computational analysis, we normalize Eq. (3.1). We define $\bar{E} = (\mu_g T_{2g}/\hbar)E$ and we introduce the retarded time $t' = t-(n/c)z$, the normalized time $\bar{t} = t/T_{2g}$, and the normalized distance $\bar{z} = lz$, so that Eq. (3.1) becomes

$$\frac{\partial \bar{E}}{\partial \bar{z}} = -i\bar{g}\eta_g - i\frac{\bar{a}}{(T_{2a}/T_{2g})\bar{\mu}}\eta_a - \frac{1}{2}\bar{E}, \tag{3.20a}$$

$$\frac{\partial \eta_g}{\partial \bar{t}} = \frac{i}{2}\Delta_g \bar{E} - \eta_g, \tag{3.20b}$$

$$\frac{\partial \Delta_g}{\partial \bar{t}} = i(\eta_g \bar{E}^* - \eta_g^* \bar{E}) + \frac{\Delta_{g0} - \Delta_g}{T_{1g}/T_{2g}}, \tag{3.20c}$$

$$\frac{\partial \eta_a}{\partial \bar{t}} = \frac{i}{2}\bar{\mu}\Delta_a \bar{E} - \frac{\eta_a}{T_{2a}/T_{2g}}, \tag{3.20d}$$

$$\frac{\partial \Delta_a}{\partial \bar{t}} = i\bar{\mu}(\eta_a \bar{E}^* - \eta_a^* \bar{E}) + \frac{\Delta_{a0} - \Delta_a}{T_{1a}/T_{2g}}, \tag{3.20e}$$

where $\bar{g} = g/l$, $\bar{a} = a/l$, and $\bar{\mu} = \mu_a/\mu_g$.

In our simulations, we used different window sizes, depending on the pulse evolution, and we verified that the pulse intensities are always zero at the window boundaries. We spaced our node points $1-5$ fs apart, and chose a step size between 1 μm and 10 μm, depending on the material parameters in the simulation. In each simulation these values were constant, and we checked that reducing these values made no visible difference in our plotted results. Finally, we verified by extending the propagation length that we were following the pulses over a sufficiently long length to reliably determine whether the pulses are stable or not.

In Fig. 3.6, we show the limits of $\bar{g}$ and $\bar{a}$ for stable operation with different values of T_1/T_2 when $T_{1g} = T_{1a} \equiv T_1$ and $T_{2g} = T_{2a} \equiv T_2$. We begin by assuming that a hyperbolic-secant-shaped pulse having an area of π is injected into the QCL. Before the pulse is injected, the population is completely in the upper lasing level in the gain medium, i.e., $\Delta_{g0} = 1.0$ and is completely in the ground level in

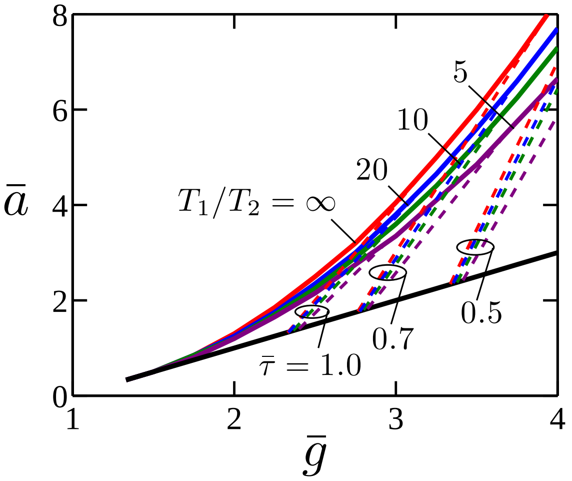

FIGURE 3.6: Stability limits of the normalized absorption ($\bar{a}$) vs. the normalized gain ($\bar{g}$) coefficients with different values of T_1/T_2. In equilibrium, the gain medium is completely inverted, i.e., $\Delta_{g0} = 1.0$, and the absorbing medium is completely uninverted, i.e., $\Delta_{a0} = -1.0$. In each bundle of dashed lines, corresponding to a fixed value of $\bar{\tau}$, T_1/T_2 decreases from left to right.

the absorbing medium, i.e., $\Delta_{a0} = -1.0$. In Fig. 3.6, the black solid line at the bottom defines the lower limits of $\bar{a}$ for any T_1/T_2. The solid curves on the top are the loss-limited boundaries for different values of T_1/T_2. The injected pulses are only stable when the gain and absorption parameters are set between these two boundary limits. Stable pulses propagate in the laser cavity with no change in shape and energy. In Fig. 3.7, we show the pulse evolution in the stable regime and the two unstable regimes. Figure 3.7(a) shows stable pulse evolution when $\bar{g} = 4.0$ and $\bar{a} = 3.5$. The laser becomes unstable when operated with $\bar{a}$ smaller than the lower limits given in Fig. 3.6 due to the growth of continuous waves. In this case, the net gain of the laser becomes positive, i.e., $\bar{g}-\bar{a}-1 > 0$, and multiple pulses may form in the cavity, leading to the generation of multiple pulses in our simulations. We give an example of this behavior in Fig. 3.7(b). In this case, we set $\bar{g} = 4.0$ and $\bar{a} = 1.0$; the laser becomes unstable when $\bar{z} = 20$, and the laser cavity develops more than one pulse. With $\bar{a}$ greater than the upper limit, the gain medium cannot compensate for absorption and the linear loss. As a result, pulses damp. In Fig. 3.7(c), which exhibits this behavior, we have set $\bar{g} = 4.0$, and $\bar{a} = 7.8$. The upper limit for $\bar{a}$ decreases when T_1/T_2 decreases as shown

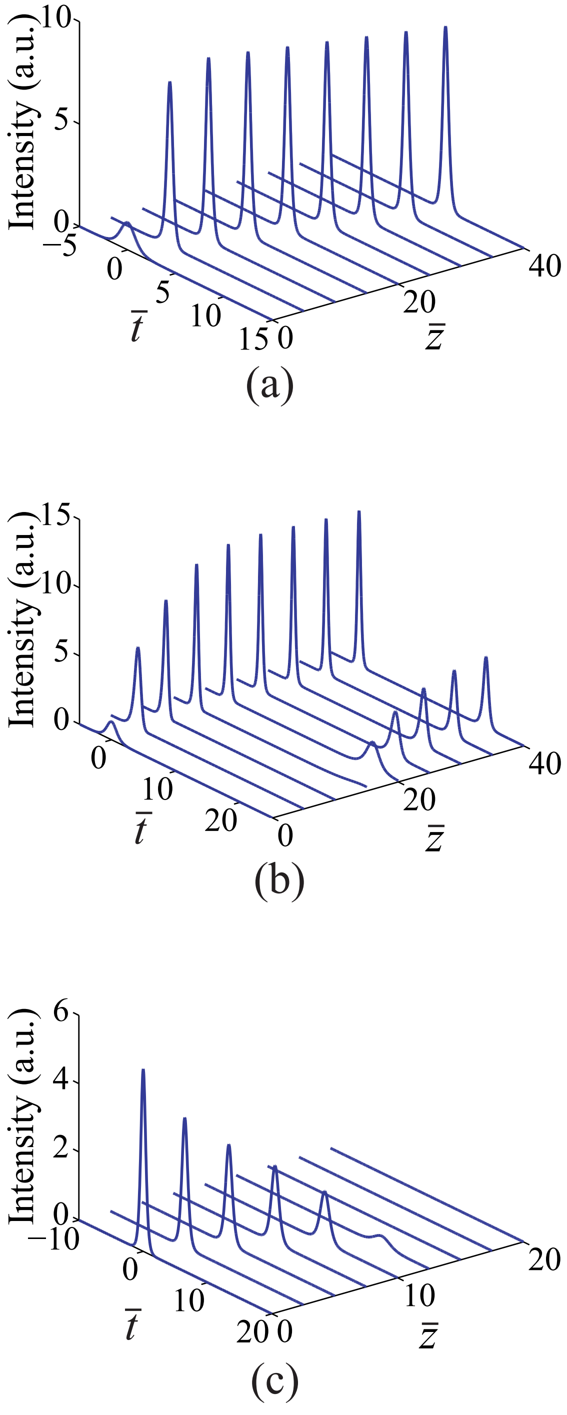

FIGURE 3.7: Pulse evolution in the system. (a) Gain and absorption coefficients are in the stable regime, $\bar{g} = 4.0, \bar{a} = 3.5$. (b) Gain and absorption coefficients are in the regime in which continuous waves are unstable, $\bar{g} = 4.0, \bar{a} = 1.0$. (c) Gain and absorption coefficients are in the regime in which any initial pulse attenuates, $\bar{g} = 4.0, \bar{a} = 7.8$. The ratio T_1/T_2 equals 10 in all cases. In equilibrium, the gain medium is completely inverted, i.e., $\Delta_{g0} = 1.0$, and the absorbing medium is completely uninverted, i.e., $\Delta_{a0} = -1.0$.

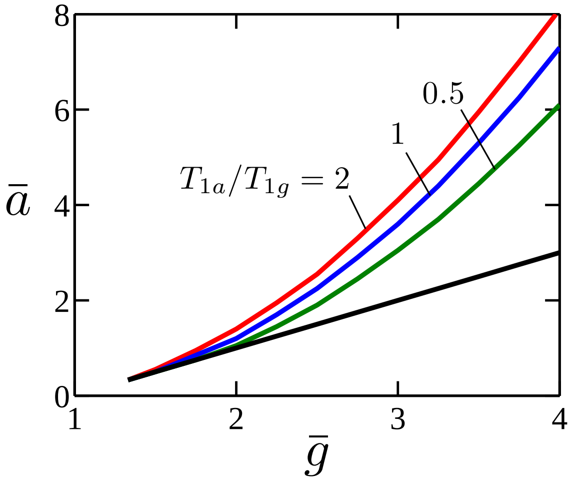

FIGURE 3.8: Stability limits of the normalized absorption ($\bar{a}$) vs. the normalized gain ($\bar{g}$) coefficients with different values of T_{1a}/T_{1g}. We set $T_{2g} = T_{2a}$ and $T_{1g}/T_{2g} = 10$ in all cases. In equilibrium, the gain medium is completely inverted, i.e., $\Delta_{g0} = 1.0$, and the absorbing medium is completely uninverted, i.e., $\Delta_{a0} = -1.0$.

in Fig. 3.6, because the damping increases. We also show contours of the stable normalized pulse duration, $\bar{\tau} = \tau_{\mathrm{FWHM}}/(1.763T_2)$, with dashed lines in Fig. 3.6. Pulse durations are on the order of T_2 when $\bar{g} \gtrsim 2.5$ and $\bar{a} \gtrsim 2.0$. The pulse durations can be made arbitrarily short by increasing $\bar{g}$ and $\bar{a}$. However, $\bar{g}$ and $\bar{a}$ are proportional to the current, so that the current must also be increased. If T_1/T_2 decreases, then $\bar{g}$ must increase if $\bar{a}$ is constant in order to maintain $\bar{\tau}$ at a constant value.

In a practical QCL design, the gain recovery times in the gain and absorbing periods will not be equal, i.e., $T_{1g} \neq T_{1a}$. For generality, we consider here the stability limits as T_{1a}/T_{1g} varies between 0.5 and 2.0. Figure 3.8 shows the stability limits of $\bar{g}$ and $\bar{a}$ as T_{1a}/T_{1g} is varied. The solid black line at the bottom is the lower limit of $\bar{a}$ and remains the same for any T_{1a}/T_{1g}. However, the upper limit of $\bar{a}$ decreases when T_{1a}/T_{1g} decreases.

The analytical solution of the Maxwell-Bloch equations given in Eq. (3.2) assumes that the absorbing medium has a dipole moment twice that of the gain medium, i.e., $\mu_a = 2\mu_g$. The condition $\mu_a = 2\mu_g$ will not be exactly satisfied due to design constraints and growth limitations. The QCL gain is determined by μ_g

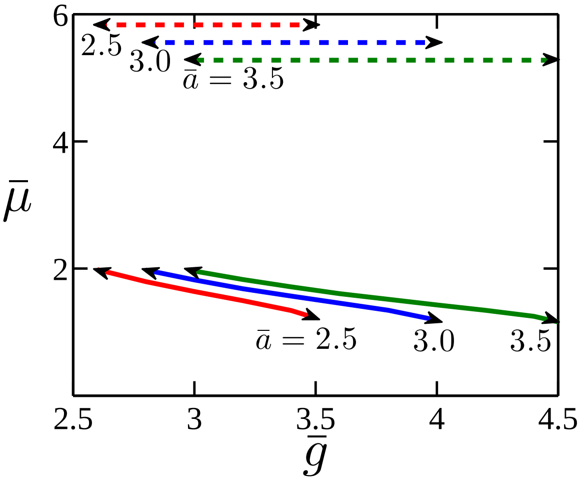

FIGURE 3.9: Stability limits of the ratio of dipole moments in absorbing and gain media ($\bar{\mu}$) vs. normalized gain coefficient ($\bar{g}$) for three cases of normalized absorption ($\bar{a}$). The ratio T_1/T_2 is 10 in all cases. In equilibrium, the gain medium is completely inverted, i.e., $\Delta_{g0} = 1.0$, and the absorbing medium is completely uninverted, i.e., $\Delta_{a0} = -1.0$.

and T_{1g}. To produce large gain, it is preferable that μ_g is large. In a vertical-transition QCL, the dipole moment is generally $\gtrsim$ 2 nm. In diagonal-transition QCLs, the dipole moment is $\gtrsim$ 1.4 nm, which is smaller. Despite the smaller value of μ_g with diagonal transitions, we must have $\mu_a/e = 2.8$ nm to satisfy the condition $\mu_a = 2\mu_g$. Therefore, it is useful in practice if SIT modelocking is possible when $\mu_a < 2\mu_g$. We determine the stability limits of $\bar{\mu} = \mu_a/\mu_g$ for stable operation. Figure 3.9 shows the lower and upper stability limits of $\bar{\mu}$ vs. $\bar{g}$ as $\bar{a}$ varies. The solid lines in Fig. 3.9 indicate the lower limits for $\bar{\mu}$, while the dashed lines indicate the upper limits. The two ends of each of the lines are at the stability boundaries for $\bar{g}$ at each particular $\bar{a}$. In each of the cases, the minimum value of $\bar{\mu}$ is approximately 2 when $\bar{g}$ is near its minimum, below which an input pulse attenuates. As $\bar{g}$ increases towards the limit at which continuous waves become unstable, the minimum value of $\bar{\mu}$ required for stable operation decreases significantly. Pulses are stable with $\bar{\mu} \sim 1.2$ when $\bar{g}$ = 3.5, 4.0, and 4.5 with $\bar{a}$ = 2.5, 3.0, and 3.5, respectively, with $\bar{g}$ just below the stability limit for generating continuous waves. However, the stable pulse duration increases significantly as $\bar{\mu}$ decreases. When $\bar{\mu}$ is below the solid lines in Fig. 3.9, pulses attenuate. The minimum value of $\bar{\mu}$ required for stable operation increases as $\bar{a}$ increases for any fixed $\bar{g}$. We have found no hard upper limit to stability as $\bar{\mu}$ increases, although the pulses are increasingly distorted. The dashed lines in Fig. 3.9 indicate the values of $\bar{\mu}$ at which the pulses become double peaked.

We simulated a number of cases in which we investigated the effect of detuning the absorbing medium from the gain medium and the carrier frequency of the light. Setting $T_1/T_2 = 10$, $\Delta_{g0} = 1.0$, and $\Delta_{a0} = -1.0$, we found that stable operation can be obtained with a detuning $\Delta_\omega T_2 \leq 0.53$ when $\bar{g} = 3.5$, $\bar{a} = 3.5$. Stable operation can be obtained with $\Delta_\omega T_2 \leq 0.36$ when $\bar{g} = 3.5$, $\bar{a} = 3.0$, and with $\Delta_\omega T_2 \leq 0.15$ when $\bar{g} = 3.5$, $\bar{a} = 2.5$.

3.5.1 Injection-Locked Pulse Dynamics

An initial pulse can be externally injected into the QCL [124]. Its duration and energy are critical parameters that must match the requirements to generate a modelocked pulse. We have derived an energy balance equation in Eq. (3.16) that defines the limits of the input energy for stable operation. However, Eq. (3.16) assumes that input pulse has a duration, $\tau_i = \tau_{\mathrm{FWHM}}/1.763 \ll T_2 \ll T_1$, so that the effects of a finite coherence time T_2 and damping due to finite T_1 may be ignored. If this condition is not satisfied, then Eq. (3.16) is no longer valid. From a practical standpoint, an input pulse having a duration on the order of T_2 or longer than T_2 is advantageous. We have calculated the dependence of the minimum and maximum input energy on the input pulse duration for two different combinations of gain and loss. We show the results in Fig. 3.10. The input pulse duration is normalized to $T_2 = T_{2g} = T_{2a}$ and is plotted on a logarithmic scale. The value of T_1/T_2 has been set to 10. When $\tau_i/T_2 = 0.1$, we find that the minimum normalized energy $\bar{\theta} = (\mu_g/\hbar)\int_{-\infty}^{\infty} E dt = \int_{-\infty}^{\infty} \bar{E} d\bar{t}$ that is required for stable operation is 0.30π when $\bar{g} = 3.5$ and $\bar{a} = 3.0$. However, as we increase τ_i/T_2, the minimum normalized pulse energy that is required for stable operation increases significantly due to the pulse's decorrelation over its duration. It increases to 0.42π when $\tau_i/T_2 = 1$, 1.31π

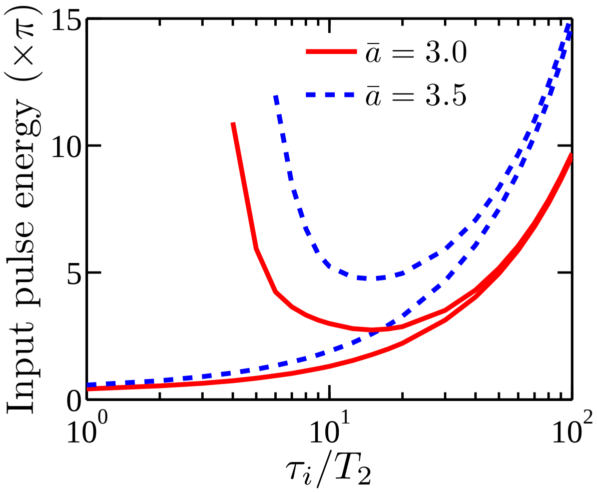

FIGURE 3.10: Input pulse energy limits vs. normalized input pulse width (τ_i/T_2) for two different cases of $\bar{g}$ and $\bar{a}$. In both the cases, we set $T_1/T_2 = 10$. In equilibrium, the gain medium is completely inverted, i.e., $\Delta_{g0} = 1.0$, and the absorbing medium is completely uninverted, i.e., $\Delta_{a0} = -1.0$.

when $\tau_i/T_2 = 10$, and 9.59π when $\tau_i/T_2 = 100$. Pulses are stable for an input energy of at least 20π when $\tau_i/T_2 \lesssim 3$.

We find that pulses split into multiple pulses when the input pulse energy $\gtrsim 2\pi$. However, as the stable pulse duration $\bar{\tau} \sim 0.5$ for the parameters $\bar{g} = 3.5$, $\bar{a} = 3.0$, only one pulse is stable, and the others damp even with an initial normalized energy of 20π when $\tau_i/T_2 < 4$. When $\tau_i/T_2 \gtrsim 4$, continuous waves become unstable. We find that multiple pulses are generated when the input energy is $\geq 3\pi$ with $\tau_i/T_2 = 10$. The upper stability limit for the input energy decreases as τ_i/T_2 increases when $\tau_i/T_2 \lesssim 10$. However, beyond that point, the upper stability limit increases with τ_i/T_2 as damping due to T_1 comes into effect. The stability limits for the input normalized energy when $\bar{g} = 3.5$ and $\bar{a} = 3.5$ show a similar trend with the exception that both the stability limits are shifted upward due to an increase in absorption.

3.6 Conclusion

In this chapter, we showed that by combining absorbing with gain periods in a QCL, one can create nearly ideal conditions to observe SIT modelocking and thereby obtain pulses that are less than 100 fs long from a mid-infrared laser. We presented detailed computational studies of the Maxwell-Bloch equations, in which we extensively investigated the stability of the solutions as the equation parameters vary. The solutions demonstrate the robustness of the SIT modelocking technique and that QCLs can be modelocked using the SIT effect within practically achievable parameter regimes.

In this work, we have treated g and a as parameters. While we expect them both to increase proportional to the current, it is important to calculate the contributions of the individual gain and absorbing periods, so that we know how many of each kind of period should be grown. These calculations require a complete calculation of the carrier distribution and coherence times in all the QCL levels. We have developed a complete carrier transport model, and we have implemented it to determine the raio of gain obtained from one gain period to absorption obtained from one absorbing period, so that we can estimate the number of gain and absorbing periods that will be required for stable modelocked operation. These results will be presented in Chapter 6.

The uni-directional, two-level Maxwell-Bloch equations that we have used in our study are a good starting point for the investigation of SIT modelocking. However, effects that are not included in the model are expected to affect the stability limits. First, it is not possible to determine the effect of edge reflections with a uni-directional model, and we cannot realistically investigate the consequences when continuous waves become unstable. For that reason, we have implemented a bi-directional model like that of Wang *et al.* [28] and Gordon *et al.* [29], but keeping both gain and absorbing media. We will present and discuss the results in Chapter 7. Second, nonlinear saturation and chromatic dispersion will set limits on the validity of our theory as they become large. The results of Wang *et al.* [28]

and Gordon *et al.* [29] indicate that these effects are not large enough in practice to seriously impact the validity of our model, but the limits that these effects impose merit further study. Therefore, we have extended our model by including the effects of the saturable nonlinearity and chromatic dispersion, and we have studied their effects on the stability of SIT modelocing in QCLs. Those results will be presented and discussed in Chapter 8.

Chapter 4

Quantum Cascade Laser Theory and Modeling

4.1 Introduction

Esaki and Tsu's invention of the superlattice in 1970 [4], together with the progress in crystal growth techniques such as molecular beam epitaxy (MBE) or metal-organic chemical vapor deposition (MOCVD) [125], opened up the possibility of creating new devices that have ultra-low dimensions with characteristics that can be precisely controlled. Quantum confinement of the electrons and the possibility of band-gap engineering [109] in heterostructures with thin layers have led to the development of novel semiconductor laser sources, detectors, and light modulators. The fundamental properties of these devices can be engineered by selective doping of the heterostructures at the time of growth. Heterostructures with appropriate doping concentrations can bend the potential energy profile across the device, and, upon application of an external electric field, the charged particles (electrons or holes) can contribute to the conduction current, so that the mobility of the devices can be enhanced.

It is important to understand the physics that underlies the electronic and optical properties of these ultra-low dimensional heterostructures, in order to create novel devices that fully utilize these properties. A quantum cascade laser (QCL) is a semiconductor heterostructure device that takes advantage of the ability to engineer the physics of quantum wells and superlattices and that exploits modern semiconductor growth technologies. When sufficiently thin layers (~ 100 Å) are alternatively grown with different material compositions, the band edge discontinuity leads to quantum confinement along the growth direction and modifies the density of states [5]. Since the photon generation in a QCL is based on an intersubband transition within the conduction band, the radiation energy can be tailored by choosing different layer thicknesses and material compositions for the quantum well and barrier.

When layer thicknesses approach the de Broglie wavelength, one must solve the Schrödinger equation to obtain the quantized energy levels and eigenstates. Next, one uses these energy levels and eigenstates to determine the radiative and nonradiative transition rates, including the tunneling rates from the injector regions into the active regions and vice versa. This modeling approach is routinely used to design QCLs [107].

In this chapter, we first present the theoretical concepts, followed by a discussion of the modeling approach. We then use this approach to design and understand the characteristics of SIT-modelocked QCLs.

4.2 Electronic States in Heterostructures

Intersubband lasers such as QCLs are composed of thin, atomically abrupt layers of two alternating materials that have different band-gap energies. Therefore, at the interfaces of two such materials, there is an offsest in the band energies. When the layers are made sufficiently thin, i.e., on the order of a de Broglie wavelength, electron motion is restricted in the growth direction $\hat{\mathbf{z}}$ and its energy is quantized [5].

To obtain the electronic states in heterostructures, we will use the effective mass approach in the envelope function approximation, and we will use the Γ-point effective mass to describe the conduction band curvature [126–129]. In general, the wavefunction for the electron is given by

$$\psi(\mathbf{r}) = F(\mathbf{r})U_{n,0}(\mathbf{r}), \tag{4.1}$$

where $U_{n,0}(\mathbf{r})$ is the lattice-periodic Bloch state wavefunctions at the band minimum, n is the subband index, and $F(\mathbf{r})$ is the envelope function that depends on the shape of the quantum well potential or other external potentials such as the electric or magnetic fields. The variation of the material composition is included in the model by using a spatially varying effective mass $m^*(z)$ and potential $E_c(z)$. This potential represents the conduction band edge profile, including any externally applied field and local variations due to space charge. Under the assumption that the lattice-periodic function is the same in all constituent materials, a Schrödinger equation for the envelope function may be written as

$$\left[-\frac{\hbar^2\nabla_{\|}^2}{2m^*(z)} - \frac{\hbar^2}{2}\frac{\partial}{\partial z}\frac{1}{m^*(z)}\frac{\partial}{\partial z} + E_c(z)\right]F(\mathbf{r}) = EF(\mathbf{r}), \tag{4.2}$$

where $\nabla_{\|}$ is the in-plane differential operator [130] and E is the corresponding energy. We may write the envelope function $F(\mathbf{r})$ as [128]

$$F(\mathbf{r}) = \frac{1}{\sqrt{S_{\|}}}\exp(i\mathbf{k}_{\|}\cdot\mathbf{r}_{\|})\psi_n(\mathbf{k}_{\|}, z), \tag{4.3}$$

where $\mathbf{k}_{\|}$ is the in-plane wavevector, $S_{\|}$ is the sample area, and $\psi_n(\mathbf{k}_{\|}, z)$ is the one-dimensional wavefunction of the n-th energy level at a fixed value of z. We find that $\psi_n(\mathbf{k}_\parallel, z)$ satisfies

$$\left[-\frac{\hbar^2}{2}\frac{d}{dz}\frac{1}{m^*(z)}\frac{d}{dz} + E_c(z) + \frac{\hbar^2 k_\parallel^2}{2m^*(z)}\right]\psi_n(\mathbf{k}_\parallel, z) = E_n(\mathbf{k}_\parallel)\psi_n(\mathbf{k}_\parallel, z), \tag{4.4}$$

where $k_\parallel^2 = \mathbf{k}_\parallel \cdot \mathbf{k}_\parallel$. The spatially dependent effective mass introduces a coupling between the in-plane direction and the z-direction. This coupling is usually neglected, and Eq. (4.4) becomes the one-dimensional Schrödinger equation

$$\left[-\frac{\hbar^2}{2}\frac{d}{dz}\frac{1}{m^*(z)}\frac{d}{dz} + E_c(z)\right]\psi_n(z) = E_n\psi_n(z), \tag{4.5}$$

where the total energy is given by

$$E_n(\mathbf{k}_\parallel) = E_n + \frac{\hbar^2 k_\parallel^2}{2m^*} \tag{4.6}$$

and m^* is the well material effective mass. The energy $E_n(\mathbf{k}_\parallel)$ is the sum of the z-direction energy and the in-plane free particle kinetic energy. We can justify the neglect of coupling between the in-plane and z-directions by noting that inclusion of this coupling in Eq. (4.5) would effectively change the barrier height $E_c(z)$ by the energy

$$\Delta E_c = \frac{\hbar^2 k_\parallel^2}{2m^*}\left[\frac{m^*}{m^*(z)} - 1\right], \tag{4.7}$$

as can be derived from Eq. (4.4), assuming the form of Eq. (4.5) for $E_n(\mathbf{k}_\parallel)$. As long as the in-plane kinetic energy is within the barrier height, it is reasonable to neglect this coupling. The form of the kinetic energy operator is chosen to preserve continuity of the envelope functions and current density across material interfaces.

If the layer thickness becomes smaller than the de Broglie wavelength, then there will be a large contribution of the individual atomic potentials to the crystal potential. However, for most QCLs, the use of an envelope function and the validity of the envelope function can be justified using the mathematical approach developed by Bastard [126–128].

In this work, we solve Eq. (4.5) using a finite-difference scheme, where the structure of interest is divided into nodes with constant material parameters. QCL material compositions usually consist of an InGaAs alloy for the quantum well and an InAlAs alloy for the barrier lattice matched to an InP substrate and a GaAs alloy for the quantum well and an AlGaAs alloy for the barrier lattice matched to GaAs.

The electron population in the quantized energy levels introduces space charge that affects the conduction band profile $E_c(z)$. For this reason, it is sometimes necessary to solve the Poisson equation

$$\frac{d}{dz}\left[\epsilon(z)\frac{d}{dz}\Phi(z)\right] = -\rho(z), \tag{4.8}$$

where $\Phi(z)$ is the electrostatic potential, $\epsilon(z)$ is the spatially varying permittivity, and $\rho(z)$ is the charge density, yielding $E_c(z) = E_{c,0}(z) - e\Phi(z)$, where $E_{c,0}(z)$ is the intrinsic conduction band profile and e is the charge of an electron. The Poisson and Schrödinger equations are iteratively solved to obtain a self-consistent solution. However, for designs where the electron density is sufficiently low that the $E_c(z)$ is not significantly perturbed, a self-consistent solution is not necessary [131].

In a QCL, the electronic energy levels are designed to force the electrons to move into the lower subband minima. As a consequence, in-plane motion of the electrons is close to the bulk conduction minimum, so that the band non-parabolicity can be neglected in most cases. However, this approximation can be improved by expanding the E vs. $k_\parallel$ relation by adding additional even polynomial terms [132]. Inclusion of band non-parabolicity is often described in terms of a $k_\parallel$-dependent — or equivalently E-dependent — effective mass given by [133]

$$m^*(E) = m^*(0)[1 + \gamma(E - V)], \tag{4.9}$$

rather than a constant effective mass, where V is the barrier height. The nonparabolicity coefficient γ is given by

$$\gamma = \left[1 - \frac{m^*(0)}{m_0}\right]^2 E_g^{-1}, \tag{4.10}$$

where E_g is the bandgap of the material and m_0 is the mass of an electron.

4.3 Strained Heterostructures

The introduction and improvement of novel growth techniques, particularly, MBE, have made it possible to produce high-quality epitaxial interfaces, not only between lattice-matched semiconductors, but even between materials that differ in their lattice constants by several percent. Such a lattice mismatch can be accommodated by a uniform lattice strain in sufficiently thin layers [134]. The resulting "pseudomorphic" interface is characterized by an in-plane lattice constant that remains the same throughout the structure. These strains can cause profound changes in the electronic properties, and therefore provide extra flexibility in device design. In particular, the conduction band offset can be increased, and hence light of new wavelengths can be generated. In this section, we will discuss a simple model — the deformational potential theory — that is often used to describe the effects of strain on the band structure.

The strains in a pseudomorphic system can be determined by minimizing the macroscopic elastic energy with the constraint that the lattice constant in the plane, $a_{\|}$, is the same throughout the structure. We will derive the strain tensors in each of the materials. For a system in which h_1 and h_2 are the respective thicknesses of the unstrained layers of semiconductors 1 and 2, we can write [135]

$$a_{\parallel} = \frac{a_1 G_1 h_1 + a_2 G_2 h_2}{G_1 h_1 + G_2 h_2}, \tag{4.11a}$$

$$\epsilon_{i\parallel} = \frac{a_{\parallel}}{a_i} - 1, \tag{4.11b}$$

$$a_{i\perp} = a_i[1 - D_i(a_{\parallel}/a_i - 1)], \tag{4.11c}$$

$$\epsilon_{i\perp} = \frac{a_{i\perp}}{a_i} - 1, \tag{4.11d}$$

where i denotes the material (1 or 2), a_i denotes the equilibrium lattice constants, $\epsilon_{i\parallel}$ and $\epsilon_{i\perp}$ denote the parallel and perpendicular components of the strain tensor, and G_i is the shear modulus given by

$$G_i = 2(c_{11}^i + 2c_{12}^i)(1 - D_i/2). \tag{4.12}$$

The constant D depends on the elastic constants c_{11}, c_{12}, and c_{44} of the respective materials, and on the interface orientation

$$D^{001} = 2\frac{c_{12}}{c_{11}}, \tag{4.13a}$$

$$D^{110} = \frac{c_{11} + 3c_{12} - 2c_{44}}{c_{11} + c_{12} + 2c_{44}}, \tag{4.13b}$$

$$D^{111} = 2\frac{c_{11} + 2c_{12} - 2c_{44}}{c_{11} + 2c_{12} + 4c_{44}}. \tag{4.13c}$$

Equation (4.11a) implies that when $h_1/h_2 \to \infty$, then $a_{\parallel} \to a_1$, which corresponds to a substrate of semiconductor 1 with a strained overlayer of semiconductor 2. In general, if a thin overlayer is grown on a substrate, the value of $a_{\parallel}$ is determined by the substrate and may be varied by using different substrates. However, in the general case, $a_{\parallel}$ must be determined using Eq. (4.11a). Once $a_{\parallel}$ is known, $a_{i\perp}$ can be obtained using Eq. (4.11c).

Van de Walle's [135] model-solid theory gives the expressions for relative shifts of conduction and valence bands that are valid for both diamond and zinc-blende lattices in terms of model-solid deformation potentials

$$\Delta E_c = a_c \frac{\Delta\Omega}{\Omega}, \tag{4.14}$$

$$\Delta E_{v,\mathrm{av}} = a_v \frac{\Delta\Omega}{\Omega}, \tag{4.15}$$

where E_c is the conduction band energy, $E_{v,\mathrm{av}}$ is the average of the three top valence bands, a_c and a_v are respectively the conduction and valence band deformation potentials, and, $\Delta\Omega/\Omega = Tr(\hat{\epsilon}) = (\epsilon_{xx} + \epsilon_{yy} + \epsilon_{zz})$ is the fractional volume change.

Heterostructures are often based not only on pure materials, but also on alloys. Varying the composition of an alloy yields variations in the lattice constant. These variations are well-described by a linear interpolation such as in the virtual-crystal approximation. Varying the compositions provides additional flexibility in tailoring the electronic properties of the alloy. When the constituent materials are not lattice-matched, one should actually also consider a strain contribution, since in an alloy $A_xB_{1-x}C$, with lattice constant $a_0 = xa_0(AC) + (1-x)a_0(BC)$ one material is effectively expanded, while the other is compressed. For an energy E, with deformation potential a_i, this effect leads to the following expression [136]

$$\begin{aligned} E(x) =& xE(AC) + (1-x)E(BC) \\ &+ 3x(1-x)[-a_i(AC) + a_i(BC)]\frac{\Delta a}{a_0}, \end{aligned} \tag{4.16}$$

where $\Delta a = a_0(AC) - a_0(BC)$.

4.4 Intersubband Radiative Transitions

The optical gain for a QCL is provided by stimulated emission of photons from electron transitions between subbands in the multi-quantum well structure. Neglecting non-parabolicity, the initial and final subbands have the same curvature, and hence the joint density of states for an intersubband transition is a Dirac delta function at the subband separation $\hbar\omega = E_i - E_f$. The following section will review the calculation of the spontaneous and stimulated transition rates. The discussion given here is standard and has been adapted from [5, 137, 138].

Transitions between conduction subbands in quantum wells occur at a rate given by Fermi's golden rule

$$W_{i\to f} = \frac{2\pi}{\hbar} \left|\langle f, n_{\mathbf{q},\sigma} \left|H'\right| i, m_{\mathbf{q},\sigma}\rangle\right| \delta[E_f(\mathbf{k}_f) - E_i(\mathbf{k}_i) \pm \hbar\omega_{\mathbf{q}}], \tag{4.17}$$

where

$$H' = -\frac{e}{m^*}\mathbf{A}\cdot\mathbf{p} \tag{4.18}$$

is the interaction Hamiltonian. In Eq. (4.18), $\mathbf{A}$ is the vector potential of the incoming light and $\mathbf{p}$ is the momentum operator. The initial and final states $|i, n_{\mathbf{q},\sigma}\rangle$ and $|f, m_{\mathbf{q},\sigma}\rangle$ are product states of the electron conduction band envelope function eigenstates i, f and the photon eigenstates with n and m photons in each mode. The modes are given by the photon wavevector $\mathbf{q}$ at frequency $\omega_{\mathbf{q}}$, and the polarization state discribed by $\sigma = 1, 2$. The parameter m^* is the effective mass in the well. In this discussion, we neglect the non-parabolicity of the band structure. The inclusion of the band non-parabolicity will modify the oscillator strengths and selection rules. More complete expressions that include the spatial dependence of the effective mass and non-parabolicity are given in [133] and [139].

The Lorentz-gauge vector potential $\mathbf{A}$ for a harmonic interation can be written in terms of the creation and annihilation operators $a^\dagger_{\mathbf{q},\sigma}$ and $a_{\mathbf{q},\sigma}$ as

$$\mathbf{A} = \sqrt{\frac{\hbar}{2\epsilon\omega_{\mathbf{q}}V}}\hat{\mathbf{e}}_{\mathbf{q}\sigma}\left[a_{\mathbf{q},\sigma}\mathrm{exp}(i\mathbf{q}\cdot\mathbf{r}) + a^\dagger_{\mathbf{q},\sigma}\mathrm{exp}(-i\mathbf{q}\cdot\mathbf{r})\right]. \tag{4.19}$$

In this expression, ϵ is the permittivity, V is the volume of the cavity, and $\hat{\mathbf{e}}_{\mathbf{q},\sigma}$ is the polarization vector. Application of the creation and annihilation operators yield an expression for the matrix element

$$\begin{aligned}\left|\left\langle H'_{i\to f}\right\rangle\right|^2/C =& m_{\mathbf{q},\sigma}\delta_{m_{\mathbf{q},\sigma}-1,n_{\mathbf{q},\sigma}}\left|\langle f\left|\exp(i\mathbf{q}\cdot\mathbf{r})\hat{\mathbf{e}}_{\mathbf{q},\sigma}\cdot\mathbf{p}\right|i\rangle\right|^2\\ &+(m_{\mathbf{q},\sigma}+1)\delta_{m_{\mathbf{q},\sigma}+1,n_{\mathbf{q},\sigma}}\left|\langle f\left|\exp(-i\mathbf{q}\cdot\mathbf{r})\hat{\mathbf{e}}_{\mathbf{q},\sigma}\cdot\mathbf{p}\right|i\rangle\right|^2, \end{aligned}\tag{4.20}$$

where

$$C=\frac{e^2\hbar}{2m^{*2}\epsilon\omega_{\mathbf{q}}V}. \tag{4.21}$$

The first term in Eq. (4.20) corresponds to absorption of a photon, and the second term corresponds to emission of a photon. The terms proportional to the number of photons in the mode $m_{\mathbf{q},\sigma}$ correspond to stimulated emission, and the field-independent term corresponds to spontaneous emission.

The initial and final electron states can be written in coordinate space $\mathbf{r}=(x,y,z)$ as the product of a transverse and longitudinal envelope function as in Eq. (4.3), where the in-plane coupling has been neglected, so that $\psi_n(\mathbf{k}_\parallel,z)=\psi_n(z)$. We then find,

$$F_i(\mathbf{r})=\langle\mathbf{r}|i\rangle=\frac{1}{\sqrt{S_\parallel}}\exp(i\mathbf{k}_{\parallel,i}\cdot\mathbf{r}_\parallel)\psi_i(z), \tag{4.22a}$$

$$F_f(\mathbf{r})=\langle\mathbf{r}|f\rangle=\frac{1}{\sqrt{S_\parallel}}\exp(i\mathbf{k}_{\parallel,f}\cdot\mathbf{r}_\parallel)\psi_f(z), \tag{4.22b}$$

where $S_\parallel$ is the normalization area.

Since the cell period is by assumption small compared to the oscillation period of the envelope, we can adopt the dipole approximation $\exp(i\mathbf{q}\cdot\mathbf{r})\simeq 1$. Then the dipole interaction between the conduction subbands may be written as

$$\begin{aligned}&\langle f\left|\exp(\pm i\mathbf{q}\cdot\mathbf{r})\hat{\mathbf{e}}_{\mathbf{q},\sigma}\cdot\mathbf{p}\right|i\rangle\cong\langle f\left|\hat{\mathbf{e}}_{\mathbf{q},\sigma}\cdot\mathbf{p}\right|i\rangle\\ &=(\hat{\mathbf{e}}_{\mathbf{q},\sigma}\cdot\mathbf{k}_{\parallel,i})\frac{\hbar}{S_{xy}}\int d\mathbf{r}_\parallel\exp[i(\mathbf{k}_{\parallel,i}-\mathbf{k}_{\parallel,f})\cdot\mathbf{r}_\parallel]\int dz\ \psi_f^*(\mathbf{k}_{\parallel,f},z)\psi_i(\mathbf{k}_{\parallel,i},z)\\ &-\hat{\mathbf{z}}\frac{i\hbar}{S_{xy}}\int d\mathbf{r}_\parallel\exp[i(\mathbf{k}_{\parallel,i}-\mathbf{k}_{\parallel,f})\cdot\mathbf{r}_\parallel]\int dz\ \psi_f^*(\mathbf{k}_{\parallel,f},z)\frac{\partial\psi_i(\mathbf{k}_{\parallel,i},z)}{\partial z}\\ &=(\hat{\mathbf{e}}_{\mathbf{q},\sigma}\cdot\hat{\mathbf{z}})\delta_{\mathbf{k}_{\parallel,f},\mathbf{k}_{\parallel,i}}\langle\psi_f|p_z|\psi_i\rangle.\end{aligned}\tag{4.23}$$

The first term in the second form of Eq. (4.23) vanishes due to the orthonormality of the envelope functions ψ_i and ψ_f. The disappearance of this term is an example of the intersubband selection rule: Only transitions with the **E**-field polarized along the growth axis $\hat{\mathbf{z}}$ are permitted. The delta-function in Eq. (4.23) ensures conservation of in-plane momentum over a transition.

Equation (4.23) is more commonly written in terms of the dipole interaction $e\mathbf{r} \cdot \mathbf{E}$. We can rewrite the matrix elements by making use of the commutation relation for the unperturbed Hamiltonian H_0

$$\frac{i}{\hbar}[H_0, z] = \frac{p_z}{m^*}, \tag{4.24}$$

where $[H_0, z]$ is the commutation operator $H_0 z - z H_0$. We then obtain

$$\langle f|p_z|i\rangle = \frac{im^*}{\hbar}(E_f - E_i)\langle\psi_f|z|\psi_i\rangle, \tag{4.25}$$

where the integral $\langle\psi_f|z|\psi_i\rangle$ is the dipole matrix element $z_{i\to f}$. Inserting this matrix element into Eq. (4.17) and Eq. (4.21) gives the following spontaneous and stimulated transition rates $W^{\mathrm{sp}}_{i\to f/\mathrm{mode}}$ and $W^{\mathrm{st}}_{i\to f/\mathrm{mode}}$ per mode between the initial i and final f states,

$$W^{\mathrm{sp}}_{i\to f/\mathrm{mode}} = \frac{\pi e^2 \omega_{\mathbf{q}}}{\epsilon V} \left|\hat{\mathbf{e}}_{\mathbf{q},\sigma} \cdot \hat{\mathbf{z}}\right|^2 |z_{i\to f}|^2 \delta(E_f - E_i + \hbar\omega_{\mathbf{q}}), \tag{4.26a}$$

$$W^{\mathrm{st}}_{i\to f/\mathrm{mode}} = \frac{\pi e^2 \omega_{\mathbf{q}}}{\epsilon V} \left|\hat{\mathbf{e}}_{\mathbf{q},\sigma} \cdot \hat{\mathbf{z}}\right|^2 |z_{i\to f}|^2 \delta(E_f - E_i + \hbar\omega_{\mathbf{q}}) m_{\mathbf{q},\sigma}, \tag{4.26b}$$

where the Kronecker delta functions conserving in-plane momentum and photon number have been dropped to simplify the notation.

4.4.1 Spontaneous Emission

To obtain the total spontaneous emission rate $W^{\mathrm{sp}}_{i\to f}$, we must sum Eq. (4.26a) over all of the photon modes and polarizations in the cavity. The number of electromagnetic modes in a differential volume $d^3\mathbf{q}$ in $\mathbf{q}$-space is given by

$$\rho(\mathbf{q})d^3\mathbf{q} = \frac{d^3\mathbf{q}}{8\pi^3/V} = \frac{q^2 dq \sin\theta d\theta d\phi V}{8\pi^3}, \tag{4.27}$$

when it is assumed that the cavity dimensions are much larger than the wavelength.

If we choose the polarization direction such that $\hat{\mathbf{e}}_{\mathbf{q},\sigma=1}$ lies in the plane defined by $\hat{\mathbf{z}}$ and $\mathbf{q}$, we can write $|\hat{\mathbf{e}}_{\mathbf{q},\sigma=2}\cdot\hat{\mathbf{z}}|^2 = 0$ and $|\hat{\mathbf{e}}_{\mathbf{q},\sigma=1}\cdot\hat{\mathbf{z}}|^2 = \sin^2\theta$. Then, it is only necessary to sum over one set of polarizations. We obtain

$$\begin{aligned} W^{\mathrm{sp}}_{i\to f} &= \frac{e^2}{8\pi^2\epsilon\hbar}|z_{i\to f}|^2 \int_0^\infty \int_0^\pi \int_0^{2\pi} \left(\frac{n\omega_{\mathbf{q}}}{c}\right)^3 \sin^3\theta\, \delta(E_f - E_i + \hbar\omega_{\mathbf{q}}) d\hbar\omega d\theta d\phi \\ &= \frac{e^2 n\omega_0^3}{3\pi\epsilon_0\hbar c^3}|z_{i\to f}|^2 = \frac{e^2 n\omega_0^2}{6\pi m^*\epsilon_0 c^3} f_{i\to f}, \end{aligned} \tag{4.28}$$

where n is the index of refraction at the center transition frequency $\omega_0 = (E_i - E_f)/\hbar$, c is the speed of light in vacuum, and $f_{i\to f}$ is the scaled oscillator strength. As shown above, the spontaneous emission rate can be expressed in terms of the dipole matrix element or the scaled oscillator strength. The scaled oscillator strength is given by

$$f_{i\to f} = \frac{m^*}{m_0} f_{i\to f,\mathrm{unscaled}} = \frac{2m^*(E_f - E_i)|z_{i\to f}|^2}{\hbar^2}, \tag{4.29}$$

where $f_{i\to f,\mathrm{unscaled}}$ is the unscaled oscillator strength. The scaled oscillator strength is $f \equiv 1$ for a classical Hertzian dipole. It is convenient to use the scaled oscillator strength $f_{i\to f}$ since it is proportional to the gain, and it is a measure of the strength of a transition. Furthermore, one can use the commutation rules $[z, p_z] = i\hbar$ and $im^*[z, H] = \hbar p_z$ to obtain the Thomas-Reiche-Kuhn sum rule for the scaled oscillator strength

$$\sum_{f\neq i} f_{i\to f} = 1. \tag{4.30}$$

Note that these commutation relations hold strictly only in the case of a single effective mass m^*, rather than a spatially dependent one. Modifications to this sum rule due to a spatially dependent effective mass and non-parabolicity are discussed in Sirtori *et al.* [133].

In a typical QCL structure, the spontaneous emission time $\tau^{\mathrm{sp}}_{i\to f}$ is longer than a microsecond and $\tau^{\mathrm{sp}}_{i\to f}$ scales as ω^{-2}. Therefore, radiative transitions are expected to play no role in subthreshold transport, since nonradiative lifetimes are on the order of picoseconds.

4.4.2 Stimulated Emission

The stimulated emission rate can be found by using the single mode transition rate Eq. (4.26b) to examine the interaction of the dipole with the l-th cavity mode whose central frequency is ν_l. Since each energy level has a finite width due to its finite lifetime, it is useful to replace the Dirac delta-function with a normalized lineshape function $\gamma(\nu)$ for the transition. A homogeneously broadened transition will have a Lorentzian lineshape

$$\gamma(\nu) = \frac{\Delta\nu/2\pi}{(\nu-\nu_l)^2 + (\Delta\nu/2)^2}, \tag{4.31}$$

where $\Delta\nu$ is the full width half maximum linewidth of the transition centered about ν_l.

The stimulated emission rate $W^{\mathrm{st}}_{i\to f}$ is given by

$$W^{\mathrm{st}}_{i\to f} = \frac{\eta\lambda^2 I_\nu}{8\pi h\nu n^2 \tau^{\mathrm{sp}}_{i\to f}}\gamma(\nu), \tag{4.32}$$

where we have substituted the incident wave intensity

$$I_{\nu l} = \frac{c m_l h\nu_l}{nV} \tag{4.33}$$

that corresponds to m_l photons in the l-th cavity mode. The interaction of the incident field with the atom-like dipoles is described by the parameter

$$\eta = \frac{3|z_{i\rightarrow f}|^2}{|\mathbf{r}_{i\rightarrow f}|^2}, \tag{4.34}$$

where $\mathbf{r}_{i\rightarrow f} = \langle \psi_f(\mathbf{r})|\mathbf{r}|\psi_i(\mathbf{r})\rangle$. As long as the incident radiation is z-polarized, as is the case for intersubband spontaneous noise input, we find that $\eta = 3$ for intersubband stimulated transitions because all of the multi-quantum well "dipoles" are oriented in the same direction, rather than being randomly oriented as in atomic media.

4.4.3 Intersubband Gain

It is now possible to obtain an equation of the intersubband optical gain using the expressions for spontaneous and stimulated emission. Let us consider a two-level system with population densities N_1 and N_2 in subbands with energies E_1 and E_2, so that, in the presence of the l-th cavity mode, there will be N_2W_{21} induced transitions from $2 \rightarrow 1$, and N_1W_{12} induced transitions from $1 \rightarrow 2$. As a consequence, this is a net power flow into the propagating wave, given by

$$\frac{\text{Power}}{\text{Volume}} = [N_2W_{21} - N_1W_{12}]h\nu, \tag{4.35}$$

where $W_{12}^{\text{st}} = W_{21}^{\text{st}}$ is proportional to the field intensity I_ν as seen in Eq. (4.32). The initial and final subbands have the same density of states if we neglect the non-parabolicity. Therefore, we can neglect differences in level degeneracy. Now, if $N_2 > N_1$, the propagating wave will be amplified, so that

$$\frac{dI_\nu}{dz} = g(\nu)I_\nu. \tag{4.36}$$

The gain for intersubband transitions can be obtained by inserting the stimulated transition rate of Eq. (4.32) into Eq. (4.35). The small signal bulk gain per unit length for a transition with a population inversion per unit volume ΔN is

$$\begin{aligned} g(\nu) &= \frac{\Delta N e^2 \pi \nu_0 |z_{i\to f}|^2}{\hbar c n \epsilon_0} \gamma(\nu) \\ &= \frac{\Delta N e^2 f_{i\to f}}{4m^* c n \epsilon_0} \gamma(\nu). \end{aligned} \tag{4.37}$$

We can write the three-dimensional population inversion as $\Delta N = \Delta N^{2\mathrm{D}}/L_{\mathrm{mod}}$, where $\Delta N^{2\mathrm{D}}$ is the two-dimensional population inversion density, and L_{mod} is the length of a module. The peak gain at frequency ν_l is therefore

$$\begin{aligned} g(\nu_l) &= \frac{2\Delta N e^2 \nu_l |z_{i\to f}|^2}{\hbar c n \epsilon_0 \Delta\nu} \\ &= \frac{e^2}{2\pi m^* c n \epsilon_0} \frac{\Delta N f_{i\to f}}{\Delta\nu}. \quad \text{(SI units)}. \end{aligned} \tag{4.38}$$

Hence, according to Eq. (4.38), the intersubband gain is proportional to the population inversion ΔN and $|z_{i\to f}|^2$ or the oscillator strength $f_{i\to f}$.

When a single-mode QCL operates above threshold, the population inversion is ideally clamped at its threshold value ΔN_{th}. Since the spontaneous emission rate is independent of the photon mode number, the stimulated emission rate exponentially increases and reduces the total lifetime, while amplifying the incident wave. Thus, it is useful to relate the stimulated emission rate to the gain at threshold g_{th} and the intra-cavity photon number S.

Since the traveling intensity I_ν, according to the Eq. (4.36), is directly proportional to the photon density S, the growth of the intra-cavity photons from an initial value S to a value $S + \Delta S$ is

$$S + \Delta S = S \exp[g(z)\Delta z]. \tag{4.39}$$

If Δz is sufficiently small, then the growth rate can be approximated as $\exp[g(z)\Delta z] \simeq 1 + g(z)\Delta z$. Given $\Delta z = v_g \Delta t$, where v_g is the group velocity c/n, we find

$\Delta S = Sgv_g\Delta t$. Therefore, the photon generation rate is

$$\frac{dS}{dt} = v_g g S. \tag{4.40}$$

The expression for the gain at threshold g_{th} can be rewritten in terms of the population inversion at the threshold ΔN_{th} by using Eq. (4.32) and Eq. (4.36) to yield

$$\begin{aligned} g_{\mathrm{th}} &= \Delta N_{\mathrm{th}} \frac{\eta\lambda^2}{8\pi n^2 \tau_{i\to f}^{\mathrm{sp}} v_g}\gamma\nu \\ &= \Delta N_{\mathrm{th}} W_{i\to f}^{\mathrm{st}} \frac{h\nu}{v_g I_\nu}. \end{aligned} \tag{4.41}$$

Since $h\nu/I_\nu$ (cm^{-2}) is equal to $1/S$ (cm^{-2}), this expression gives the stimulated emission lifetime τ_{st} of the upper lasing state for the single quantum-well transition, expressed in terms of the population inversion at threshold ΔN_{th} (cm^{-2}) and intra-cavity photon density S (cm^{-2})

$$\tau_{\mathrm{st}} = \frac{\Delta N_{\mathrm{th}}}{v_g g_{\mathrm{th}} S}. \tag{4.42}$$

Since a QCL repeats this intersubband transition periodically with N_p cascaded repetitions of the same structure. The gain expression g_{th} in Eq. (4.41) corresponds to the gain in a single cascaded period; the total gain in N_p periods is $g_{\mathrm{th}}N_p$ and the corresponding stimulated emission lifetime of a QCL becomes

$$\tau_{\mathrm{st}} = \frac{\Delta N_{\mathrm{th}}}{v_g g_{\mathrm{th}} N_p S}. \tag{4.43}$$

4.5 Intersubband Nonradiative Transitions

In addition to the radiative transitions, the design of a QCL requires a thorough understanding of the nonradiative transitions. Nonradiative transitions include electron-polar longitudinal optical (LO) phonon scattering, electron-electron scattering, electron-interface roughness scattering, electron-acoustic phonon scattering, and electron-impurity scattering. These scattering mechanisms may occur between two subbands within the conduction band (intersubband) or within a single subband in the conduction band (intrasubband). If energy separation of conduction subbands is larger than the LO phonon energy (E_{LO}), then electron-LO phonon scattering is the dominant scattering mechanism for the intersubband transitions [140, 141].

For intersubband transitions where the energy separation of the subbands is less than E_{LO}, emission of LO phonons is energetically forbidden at low temperatures. In this case, nonradiative relaxation is dominated by a combination of electron-electron scattering, electron-impurity scattering, and electron-LO phonon scattering of the high energy tail of the subband electron distribution. However, even when devices are operated at liquid helium temperatures, one cannot assume that the electron gas temperature is also low. Examination of energy loss rates for cooling in a single subband suggests that the electron temperature may be anywhere from 50 $\sim$ 100 K higher than the lattice temperature [142]. Therefore, even if the subband minima have an energy spacing less than E_{LO}, there are usually thermally energetic electrons whose energy exceeds E_{LO}.

Electron-electron scattering plays a more important role in intrasubband scattering [143, 144]. As will be discussed in next chapter, coherent transport through the coupled quantum wells is often prohibited by fast intrasubband electron-electron scattering. At a high carrier density, strong electron-electron scattering contributes to the rapid decay of coherence between the injector and active region states. This coherence is needed for efficient transport. The other scattering mechanisms turn out to be less important. Acoustic phonon scattering in particular is relatively inefficient, especially at low temperatures where the phonon population is small. Typical acoustic phonon intersubband scattering times are in the 100-ps range [137, 145].

Interface roughness scattering plays an insignificant role for intersubband scattering between the radiative levels. Calculation of this mechanism is difficult since it requires detailed knowledge of the microscopic growth characteristics. Smet [137] performed calculations of interface roughness scattering and found typical intersubband scattering times greater than 100 ps in both interwell and intrawell transitions for defect concentrations of 10^{10} cm^{-2}. However, the importance of this mechanism depends strongly on the overlap of the wavefunctions with the interfaces, as well as on growth characteristics; so, this mechanism cannot be ignored. Interface roughness plays a significant role in intrasubband scattering, where it contributes to broadening of the radiative linewidth and to the tunneling coherence time [112, 146].

In this section, we will review the theory and modeling of the intra- and intersubband electron-LO phonon, electron-electron, and electron-interface roughness scattering. The theories presented in this section are standard and adapted from the discussions given in [138, 145].

4.5.1 Electron–LO Phonon Scattering

Electron scattering due to LO phonons is an important relaxation mechanism for electron transport across the active region and injector region in a QCL. In this section, we give a brief derivation of electron-LO phonon scattering rates in a polar semiconductor heterostructure. In the derivation, the phonon spectrum is assumed equal to the equilibrium bulk spectrum, and modifications due to the heterostructure are ignored. Williams [138] investigated the detailed complex phonon spectrum for the design of a THz QCL in order to utilize resonant optical phonon scattering to obtain the population inversion. However, in most mid-infrared QCLs, where the energy separation is larger than the phonon energy, the bulk phonon approximation is reasonable and is nearly dispersionless at the Γ-symmetry point when the corresponding phonon energy E_{LO} is ~ 34 meV in InGaAs and ~ 36 meV in GaAs [107].

The scattering rate for an electron initially in state $|i, \mathbf{k}_i\rangle$ (subband i, in-plane wavevector $\mathbf{k}_i$) to the final state $|f, \mathbf{k}_f\rangle$ through an interaction potential H' due to an LO phonon is evaluated using Fermi's Golden rule [145],

$$W_{i\to f}(\mathbf{k}_i, \mathbf{k}_f) = \frac{2\pi}{\hbar}\left|\left\langle f, \mathbf{k}_f \middle| H'_{\mathrm{e-ph}} \middle| i, \mathbf{k}_i \right\rangle\right|^2 \delta[E_f(\mathbf{k}_f) - E_i(\mathbf{k}_i) \pm \hbar\omega_{\mathrm{LO}}], \tag{4.44}$$

where $\hbar\omega_{\mathrm{LO}}$ is the electron-LO phonon energy and $H'_{\mathrm{e-ph}}$ is the electron-LO phonon interaction Hamiltonian. The quantity $H'_{\mathrm{e-ph}}$ may be expressed as [145]

$$H'_{\mathrm{e-ph}} = \sum_{\mathbf{q}} \left\{ \alpha(\mathbf{q}) \left[\exp(i\mathbf{q}\cdot\mathbf{r}) b_{\mathbf{q}} + \exp(-i\mathbf{q}\cdot\mathbf{r}) b^{\dagger}_{\mathbf{q}} \right] \right\}, \tag{4.45}$$

where $\alpha(\mathbf{q})$ is the electron-LO phonon interaction strength and $b_{\mathbf{q}}$, $b^{\dagger}_{\mathbf{q}}$ are the creation, annihilation operators for a phonon in mode $\mathbf{q}$. The Fröhlich interaction strength for electron-LO phonon scattering is given by [147]

$$\left|\alpha(\mathbf{q})\right|^2 = \frac{\hbar\omega_{\mathrm{LO}}}{2}\frac{e^2}{q^2}\left(\frac{1}{\epsilon_\infty} - \frac{1}{\epsilon_{\mathrm{dc}}}\right), \tag{4.46}$$

where ϵ_{dc} and ϵ_∞ are the static and high-frequency permittivities, respectively. The q^{-2} dependence reduces the scattering rate for large momentum transfers, effectively reducing the scattering between subbands with large energy separations.

The matrix element for electron-LO phonon transition is given by [138]

$$\begin{aligned}\left|\left\langle f, \mathbf{k}_f \middle| H'_{\mathrm{e-ph}} \middle| i, \mathbf{k}_i \right\rangle\right|^2 = \frac{e^2\hbar\omega_{\mathrm{LO}}}{2V}\left(\frac{1}{\epsilon_\infty} - \frac{1}{\epsilon_{\mathrm{dc}}}\right)\frac{1}{q_z^2 + q_\parallel^2}|A_{i\to f}|^2 \\ \times\, \delta_{\mathbf{k}_i, \mathbf{k}_f \mp \mathbf{q}_\parallel}(n_{\omega_{\mathrm{LO}}} + 1/2 \mp 1/2),\end{aligned} \tag{4.47}$$

where $\mathbf{q}_\parallel$ and $\mathbf{q}_z$ are the components of the phonon wavevector that are perpendicular (in-plane) and parallel to the growth axis (z-axis), respectively, $n_{\omega_{\mathrm{LO}}}$ is the Bose-Einstein phonon occupation number, and the upper and lower signs correspond to phonon absorption and emission, respectively. The delta function ensures

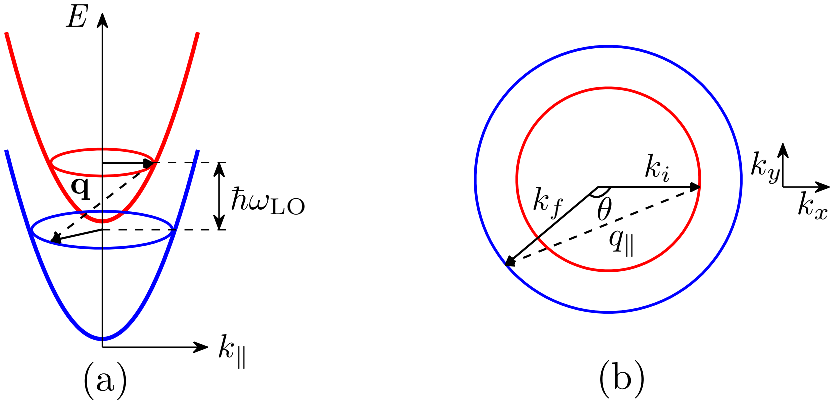

FIGURE 4.1: (a) Schematic illustration of the intersubband LO-phonon scattering process. (b) The in-plane momentum between the initial wavevector $\mathbf{k}_i$ and final wavevector $\mathbf{k}_f$ is conserved by the phonon wavevector $\mathbf{q}_{\|}$.

conservation of the in-plane momentum, and the form factor

$$A_{i\to f}(q_z) = \int_{-\infty}^{\infty} dz\ \psi_f^*(z)\psi_i(z)\ \exp(\pm i q_z z) \tag{4.48}$$

is related to the q_z-momentum uncertainty that is due to the spatially localized envelope wavefunctions $\psi_i(z)$ and $\psi_f(z)$.

This expression can then be integrated over the phonon modes $\mathbf{q}$ and final states $\mathbf{k}_f$ to yield the scattering rate $W(\mathbf{k}_i)$ from an initial wavevector. Assuming parabolic subband dispersion, the final states lie on a circle with a radius k_f that is determined by conservation of energy, so that

$$k_f^2 = k_i^2 + \frac{2m^*[E_f(0) - E_i(0) \mp \hbar\omega_{\mathrm{LO}}]}{\hbar^2}. \tag{4.49}$$

Energy conservation and the in-plane momentum conservation rule allows us to write the phonon wavevector $\mathbf{q}_{\|}$ in terms of $\mathbf{k}_i$ and $\mathbf{k}_f$

$$q_{\|}^2 = |\mathbf{k}_i - \mathbf{k}_f|^2 = k_i^2 + k_f^2 - 2k_i k_f \cos\theta, \tag{4.50}$$

where the angle θ is the angle between the in-plane wavevectors $\mathbf{k}_i$ and $\mathbf{k}_f$, as is schematically illustrated in Fig. 4.1. After summation over the phonon modes $\mathbf{q}$, Eq. (4.44) can be integrated over the final states $\mathbf{k}_f$ to yield the total scattering rate from an initial wavevector $\mathbf{k}_i$,

$$W^{\text{abs}}_{i\to f}(\mathbf{k}_i) = \frac{m^* e^2 \omega_{\text{LO}}}{8\pi\hbar^2}\left(\frac{1}{\epsilon_\infty} - \frac{1}{\epsilon_{\text{dc}}}\right) n_{\omega_{\text{LO}}} \int_0^{2\pi} d\theta\ B_{i\to f}(q_\parallel), \tag{4.51a}$$

$$W^{\text{em}}_{i\to f}(\mathbf{k}_i) = \frac{m^* e^2 \omega_{\text{LO}}}{8\pi\hbar^2}\left(\frac{1}{\epsilon_\infty} - \frac{1}{\epsilon_{\text{dc}}}\right) (n_{\omega_{\text{LO}}}+1) \int_0^{2\pi} d\theta\ B_{i\to f}(q_\parallel), \tag{4.51b}$$

where superscripts abs and em denote absorption and emission, respectively, and $B_{i\to f}$ is given by

$$B_{i\to f} = \int_\infty^\infty dz \int_\infty^\infty dz' \psi^*_f(z)\psi_i(z)\psi^*_i(z')\psi_f(z')\frac{1}{q_\parallel}\exp(-q_\parallel|z-z'|). \tag{4.52}$$

The total scattering time between subbands $s_{i\to f}$ can then be obtained by averaging over all possible initial states in the subband to yield [148]

$$\frac{1}{s_{i\to f}} = \frac{\int_0^\infty dE_k f_i(E_k)[1 - f_f(E_k \mp \hbar\omega_{\text{LO}})]W_{i\to f}(E_k)}{\int_0^\infty dE_k f_i[E_k]}, \tag{4.53}$$

where $E_k = \hbar^2 k_\parallel^2/2m^*$ is the in-plane kinetic energy in the initial subband, $f_i(E_k)$ is the Fermi distribution in the initial state, and $f_f(E_k)$ is the Fermi distribution in the final state.

4.5.2 Electron-Electron Scattering

While an electron-electron scattering event can change the energy of an individual electron, no energy is removed from the global electron system. Rather, the overall distribution is thermalized. Electron-electron scattering is expected to be important for intersubband transitions between closely spaced subbands at low temperatures where LO phonon scattering is suppressed. Experimentally, it has proven difficult to measure intersubband relaxation times between two subbands when the energy spacing is less than the LO phonon energy E_{LO}. These relaxation times are generally attributed to electron-electron intersubband scattering.

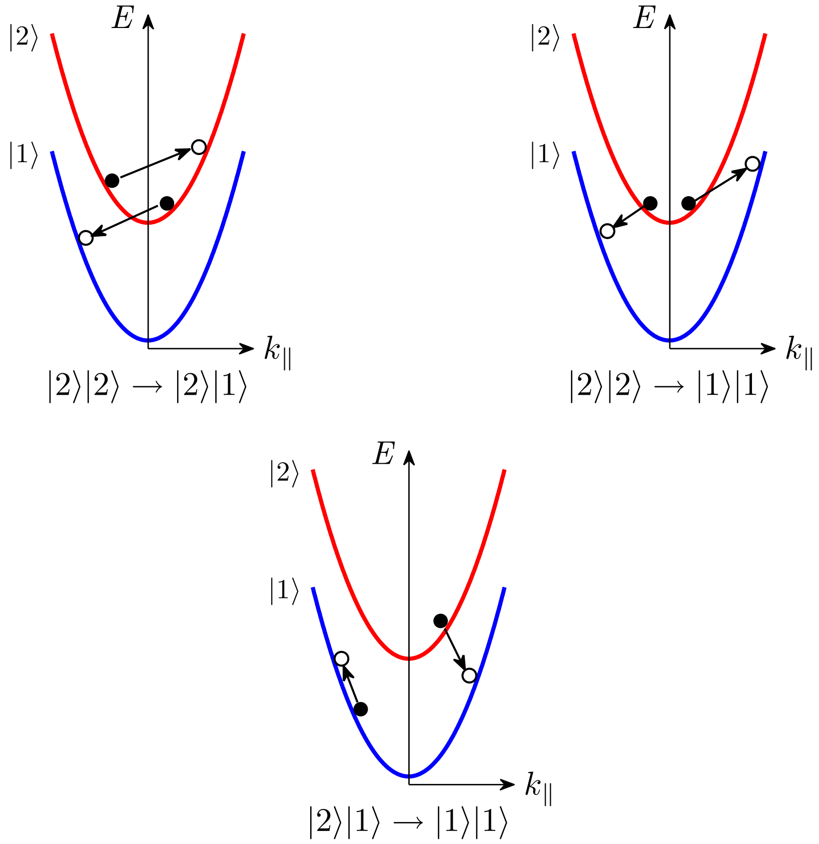

$|2\rangle|2\rangle \rightarrow |2\rangle|1\rangle$

$|2\rangle|2\rangle \rightarrow |1\rangle|1\rangle$

$|2\rangle|1\rangle \rightarrow |1\rangle|1\rangle$

FIGURE 4.2: (a) Schematic illustration of some of the seven intersubband electron-electron scattering processes that are possible between two levels. There are many more possibilities since up to four levels can be involved.

In fact, the electron-electron scattering process is complex and since four electronic states are involved, including two initial and two final states, a variety of electron-electron scattering processes exist [149–153].

In Fig. 4.2 and Fig. 4.3, we illustrate a few of the possible scenarios for intersubband electron-electron scattering and all of the scenarios for intrasubband electron-electron scattering, respectively. Among them, $|2\rangle|2\rangle \rightarrow |2\rangle|1\rangle$ and $|2\rangle|1\rangle \rightarrow |1\rangle|1\rangle$ processes are Auger-type scattering, which are important in long wavelength semiconductor lasers such as in a THz QCL, as the energy separation decreases this scattering.

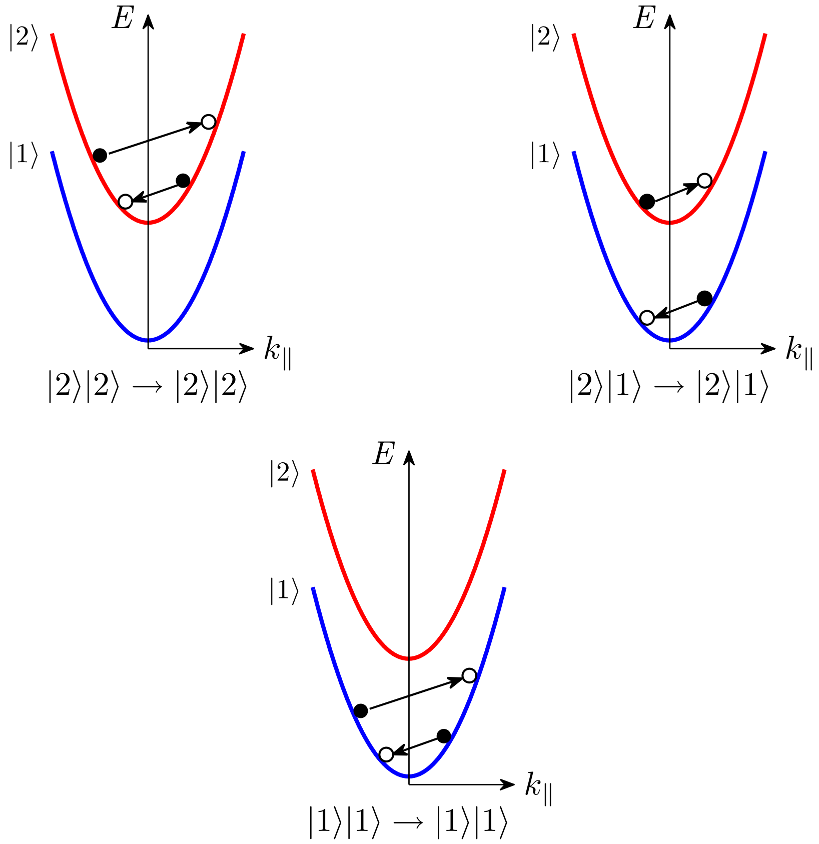

FIGURE 4.3: (a) Schematic illustration of the intrasubband electron-electron scattering processes.

Accurate calculation of electron-electron scattering rates in quantum well systems is a complicated many-body problem. Electron-electron interactions are mediated by the Coulomb potential, which is screened by the surrounding electron system. In low-density systems, where screening can be ignored, Fermi's Golden Rule is the most common method for calculating scattering rates. Because of the mathematical complexity of describing screening in a multi-subband system at a finite temperature, a simplified single-subband screening model is typically used. For intersubband transitions, the difference between a single-subband static screening model and a full dynamic, finite temperature, multi-subband dielectric function model is insignificant [138]. Calculations using both the simplified and complete models show that for moderate densities ($< 5 \times 10^{11}$ cm^{-2}), there is little difference between the intersubband rates calculated with and without screening [154].

Let us consider an electron that is initially in state $|i, \mathbf{k}_i\rangle$ that scatters due to an interaction with another electron that is initially in state $|j, \mathbf{k}_j\rangle$, so that the final states of the electrons are $|f, \mathbf{k}_f\rangle$ and $|g, \mathbf{k}_g\rangle$, respectively. The unscreened matrix element for this event is [145]

$$H'_{i,j\to f,g}(\mathbf{k}_i, \mathbf{k}_j, \mathbf{k}_f, \mathbf{k}_g) = \frac{2\pi e^2}{S_\parallel \epsilon} A_{i,j\to f,g}(q_\parallel)\delta(\mathbf{k}_f + \mathbf{k}_g - \mathbf{k}_i - \mathbf{k}_j), \tag{4.54}$$

where

$$q_\parallel = |\mathbf{k}_i - \mathbf{k}_f|, \tag{4.55}$$

and the form factor is

$$A_{i,j\to f,g}(q_\parallel) = \int_{-\infty}^{\infty} dz \int_{-\infty}^{\infty} dz' \psi_i(z)\psi_f^*(z)\psi_j(z')\psi_g^*(z')\exp(-q_\parallel|z - z'|). \tag{4.56}$$

Then the total electron-electron scattering rate is given by [145]

$$\begin{aligned} W_{i,j\to f,g}(\mathbf{k}_i) =& \frac{e^4}{2\pi\hbar\epsilon^2} \int d^2\mathbf{k}_j \int d^2\mathbf{k}_f \int d^2\mathbf{k}_g \frac{|A_{i,j\to f,g}(q_\parallel)|^2}{q_\parallel^2} f_{j,\mathbf{k}_j}(1 - f_{g,\mathbf{k}_g})(1 - f_{f,\mathbf{k}_f}) \\ & \times \delta[E_f(\mathbf{k}_f) + E_g(\mathbf{k}_g) - E_i(\mathbf{k}_i) - E_j(\mathbf{k}_j)]\, \delta(\mathbf{k}_f + \mathbf{k}_g - \mathbf{k}_i - \mathbf{k}_j). \end{aligned} \tag{4.57}$$

If we consider the effect of screening with the simplified model, then $q_\parallel^2$ in Eq. (4.57) is replaced by $\epsilon_{\text{sc}}^2(q_\parallel, T)q_\parallel^2$, where $\epsilon_{\text{sc}}^2(q_\parallel, T)$ represents the correction due to the dielectric constant that results from screening. The total electron-electron scattering time $s_{i,j\to f,g}$ can be obtained by averaging over all possible initial states in the subband

$$\frac{1}{s_{i,j\to f,g}} = \frac{\int_0^\infty dE_k^i f_i(E_k^i) W_{i,j\to f,g}(E_k^i)}{\int_0^\infty dE_k^i f_i[E_k^i]}. \tag{4.58}$$

4.5.3 Electron-Interface Roughness Scattering

Since semiconductor heterojunctions and quantum wells are composed of materials with different bandgaps, interfaces between these materials possess varying degrees of roughness. Ideally, the interfaces should be abrupt. In reality, there

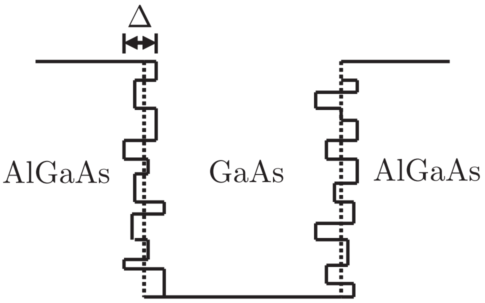

FIGURE 4.4: A sketch of a GaAs/AlGaAs quantum well showing the variation of the well thickness, which is the source of interface roughness. The dotted lines represent ideal interfaces.

is a fluctuation in the material thicknesses at the interfaces, which causes charge carriers to scatter. In Fig. 4.4, the interface roughness between GaAs and AlGaAs is presented as a variation of well thickness. The ideal interfaces are shown as dotted lines in the figure.

Electron scattering induced by the interface roughness can be calculated using the theory of Ando [146, 155, 156]. We assume that the roughness height $\Delta(\mathbf{r})$ at the in-plane position $\mathbf{r} = (x, y)$ has a correlation function

$$\langle\Delta(\mathbf{r})\Delta(\mathbf{r}')\rangle = \Delta^2 \exp\left(-\frac{|\mathbf{r}-\mathbf{r}'|^2}{\Lambda^2}\right), \tag{4.59}$$

where Δ is the mean height of roughness and Λ is the correlation length. The scattering element of an electron initially at state $|i, \mathbf{k}_i\rangle$ to the final state $|f, \mathbf{k}_f\rangle$ is given by [146]

$$\langle i, \mathbf{k}_i | H'_{\text{e-ifr}} | f, \mathbf{k}_f\rangle = \int d^2r A_{i\to f}\Delta(\mathbf{r})\exp(i\mathbf{q}\cdot\mathbf{r}) \tag{4.60}$$

with

$$A_{i\to f} = V_0 \sum_m \psi_f^*(z_m)\psi_i(z_m), \tag{4.61}$$

where V_0 is the conduction band offset, and $\psi_i(z_m)$, $\psi_f(z_m)$ are the wavefunctions of the states $|i\rangle$ and $|f\rangle$ at the interface m. Then the scattering rate due to interface-roughness is given by [146]

$$W_{i\to f}(\mathbf{k}_i) = \frac{m^*\Delta^2\Lambda^2}{2\hbar^3}V_0^2\int_0^\pi d\theta\sum_m |\psi_f^*(z_m)\psi_i(z_m)|^2 \exp(-q_\parallel^2\Lambda^2/4), \tag{4.62}$$

where $\theta = \cos^{-1}(\mathbf{k}_i\cdot\mathbf{k}_f/|\mathbf{k}_i||\mathbf{k}_f|)$ is the scattering angle. The total scattering time between subbands $s_{i\to f}$ can then be obtained by averaging over all possible initial states in the subband

$$\frac{1}{s_{i\to f}} = \frac{\int_0^\infty dE_k f_i(E_k)[1-f_f(E_k)]W_{i\to f}(E_k)}{\int_0^\infty dE_k f_i[E_k]}. \tag{4.63}$$

Scattering due to interface roughness depends largely on the interface parameters Δ and Λ. These parameters depend on the quality and environment of growth. The product $\Delta\Lambda$ has been estimated to be $\sim$1 nm^2 by comparing calculation and experiment for GaInAs/AlInAs and GaAs/AlGaAs interfaces [112, 146, 156–158].

4.6 Resonant Tunneling Transport

Resonant tunneling is an important transport mechanism in quantum cascade structures. In most QCL designs, resonant tunneling is employed to inject the electrons into the active regions and also to extract the electrons from the active regions. The role of coherent and incoherent transport in quantum cascade structures has become an active experimental and theoretical area of research [31, 159–161].

In this section, we will describe a density matrix model for resonant tunneling in a two-level system as shown in Fig. 4.5(a). Here the basic structure is repeated, and, in neighboring periods, state $|1\rangle$ is coupled to state $|2\rangle$ with a tight-binding coupling $-\Delta_0/2$. As schematically shown in Fig. 4.5(a), these localized states are eigenstates of single quantum wells only, and are not eigenstates of the coupled well system. If we diagonalize the Hamiltonian, we would obtain symmetric and antisymmetric eigenstates separated by an anti-crossing gap Δ_0. However, the

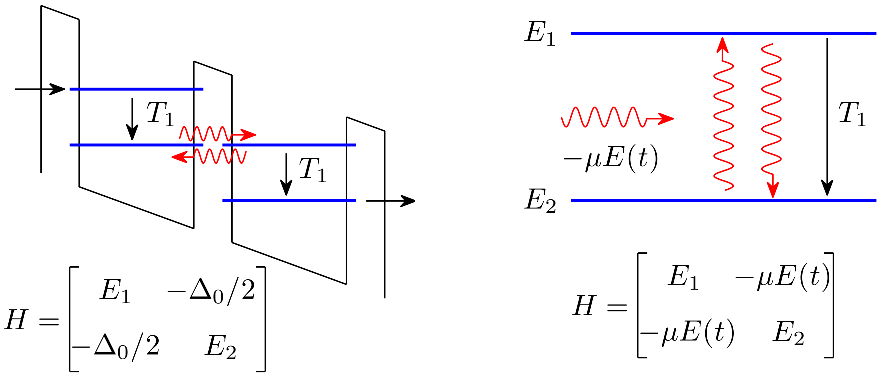
T_1
T_1
$H = \begin{bmatrix} E_1 & -\Delta_0/2 \\ -\Delta_0/2 & E_2 \end{bmatrix}$
E_1
T_1
$-\mu E(t)$
E_2
$H = \begin{bmatrix} E_1 & -\mu E(t) \\ -\mu E(t) & E_2 \end{bmatrix}$

(a) (b)

Figure 4.5: Schematic illustration and the corresponding Hamiltonian for (a) the tight-binding resonant tunneling model with an interaction $-\Delta_0/2$ and (b) the analogous two-level model with a dipole interaction $-\mu E(t)$.

use of localized states as our basis provides a physical picture where dephasing processes interrupt coherent tunneling and effectively localize the wavefunctions. The structure is periodic, so that electrons in $|2\rangle$ relax back into $|1\rangle$ with time T_1. This model for resonant tunneling is almost directly analogous to the optical Bloch equations for a two-level system in the presence of an electromagnetic field. The schematic for such an analogous two-level system is shown in Fig. 4.5(b).

Using the standard density matrix formalism, the wavefunction for an electron in the ensemble is given by

$$|\psi(t)\rangle = \sum c_i(t)|i\rangle, \tag{4.64}$$

and the density matrix ρ for a mixed state is defined by the ensemble average

$$\rho_{ij} = \langle c_i c_j^* \rangle. \tag{4.65}$$

The diagonal elements ρ_{ii} correspond to the state populations, and the off-diagonal elements ρ_{ij} represent the degree of coherence between basis states. The time evolution of ρ is described by the equation of motion

$$\frac{d}{dt}\rho = -\frac{i}{\hbar}[H,\rho], \tag{4.66}$$

where H is the Hamiltonian of the total system, as shown in Fig. 4.5(a). We obtain the following set of coupled equations that describes both the population difference $\rho_{11} - \rho_{22}$ and the off-diagonal element ρ_{21}

$$\frac{d}{dt}(\rho_{11} - \rho_{22}) = \frac{i\Delta_0}{\hbar}(\rho_{21} - \rho_{21}^*) - \frac{(\rho_{11} - \rho_{22}) - (\rho_{11} - \rho_{22})_0}{T_1}, \tag{4.67a}$$

$$\frac{d}{dt}\rho_{21} = \frac{i\Delta_0}{2\hbar}(\rho_{11} - \rho_{22}) - \frac{iE_{21}}{\hbar}\rho_{21} - \frac{\rho_{21}}{T_2}, \tag{4.67b}$$

where we note $\rho_{21} = \rho_{12}^*$. In Eq. (4.67b), the variable E_{21} denotes the detuning of E_2 and E_1 from resonance, where E_2 is the energy of $|2\rangle$, E_1 is the energy of $|1\rangle$, and $(\rho_{11} - \rho_{22})_0 = 1$ is the population difference at equilibrium. Two phenomenological terms have been added. In Eq. (4.67a), the last term allows the population to relax to its equilibrium value with time T_1; in Eq. (4.67b), the last term represents the relaxation of phase coherence with time T_2 due to scattering.

In steady state, we can solve for the elements of the density matrix and obtain an expression for the current density through the barrier

$$J = \frac{eN\rho_{22}}{T_1} = \frac{eN}{2}\frac{(\Delta_0/\hbar)T_2}{1 + (E_{21}/\hbar)^2 T_2^2 + (\Delta_0/\hbar)^2 T_1 T_2}, \tag{4.68}$$

where N is the total electron sheet density of the two levels. This expression, which is equivalent to the one reported by Kazarinov and Suris [1] and Sirtori *et al.* [162], describes the resonant current versus detuning bias E_{21} as a Lorentzian with a full width half maximum of

$$\Delta E_{21,\mathrm{FWHM}} = \frac{2\hbar}{T_2}\left[1 + \left(\frac{\Delta_0}{\hbar}\right)^2 T_1 T_2\right]^{1/2}. \tag{4.69}$$

The maximum current is obtained at resonance for $E_{21} = 0$, where

$$J_{\max} = \frac{eN}{2}\frac{(\Delta_0/\hbar)^2 T_2}{1 + (\Delta_0/\hbar)^2 T_1 T_2}. \tag{4.70}$$

The tight-binding model provides a picture in which the localized wavepacket oscillates between wells with a frequency $\omega_{\mathrm{Rabi}} = \Delta_0/\hbar$ and with a damping rate of approximately T_2^{-1}, where the wavepacket is subject to scattering with a rate T_1^{-1} every time it is in state $|2\rangle$. Examination of the expression Eq. (4.70) reveals that there are two regimes of operation. In the limit $(\Delta_0/\hbar)^2 T_1 T_2 \gg 1$, we obtain coherent tunneling in which the current density J is given by

$$J = \frac{eN}{2T_1}. \tag{4.71}$$

In this case, a wavepacket oscillates between states many times before relaxing, and thus the relaxation rate T_1^{-1} and not ω_{Rabi} is the transport bottleneck. Therefore, the population in steady-state will be distributed equally between $|1\rangle$ and $|2\rangle$.

The incoherent limit is reached when $(\Delta_0/\hbar)^2 T_1 T_2 \ll 1$, in which the current density is given by

$$J = \frac{eN}{2}\left(\frac{\Delta_0}{\hbar}\right)^2 T_2 = \frac{eN}{2}\omega_{\mathrm{Rabi}}\left(\omega_{\mathrm{Rabi}} T_2\right). \tag{4.72}$$

For the incoherent case, the current is limited by ω_{Rabi} and the coherence decay rate T_2^{-1}. In other words, only a small fraction of the electrons in the ensemble successfully tunnel through the barrier without interruption, and those that do tunnel through scatter before tunneling back. Thus tunneling transport can be considered one-way — from $|1\rangle \rightarrow |2\rangle$ — and a steady state population difference will develop between the two states. The level broadening due to scattering is larger than the anti-crossing gap, and no distinct doublet will be observed. Thus, the states can be considered localized.

Chapter 5

Carrier Transport

5.1 Introduction

In order to estimate the performance of a QCL, it is important to calculate the carrier transport rate. Moreover, understanding the basic physics of carrier transport through a QCL structure can contribute to the design of improved lasers. In general, carrier transport through a QCL is a complicated process as electrons may move due to both coherent and incoherent mechanisms [31, 160–163]. A number of scattering processes, as well as tunneling at resonance and out of resonance make the carrier distribution hard to predict without a detailed calculation. Generally, in a typical QCL structure, carriers move within an injector region and within an active region principally by scattering, while carriers move between the injector and active regions principally by tunneling.

Scattering mechanisms include electron-LO phonon scattering, electron-electron scattering, electron-acoustic phonon scattering, electron-interface roughness scattering, and electron-impurity scattering. For the usual energy spacing between the subbands in a QCL, electron scattering due to interaction with LO phonons is the dominant scattering mechanism in the intersubband transitions [140, 141]. However, electron-electron scattering may become significant if the subbands have an energy spacing that is much smaller than the LO phonon resonance energy [144]. Electron-electron scattering is also the dominant scattering mechanism in transitions that occur within a single subband [143, 144].

Recent pump-probe experiments performed on QCLs [31, 111] found evidence of coherent transport during the gain recovery of the laser, i.e., in the carrier injection from the injector into the active region. Woerner *et al.* [111] observed pronounced Rabi oscillations before the steady-state population in the upper lasing level recovered, which implies a strong coherence of the upper lasing level with the injector ground level and a long coherence time during which the electrons oscillate between these two levels. They found that the Rabi oscillations diminish when the temperature or the carrier density increases, which they attributed to the decay of the coherence between the upper lasing level and the injector ground level at an increased temperature or carrier density. A theoretical study that carefully accounts for the coherent as well as the incoherent processes is necessary to understand the physics of the phenomena observed by Woerner *et al.* [111] and to predict the carrier transport in QCLs. The strength of the coherent and incoherent processes depends strongly on the operating conditions. So, one must calculate these processes over the range of operating conditions that will appear in practice.

In this chapter, we will discuss a model of the carrier transport in QCLs. We will also introduce a model to calculate the coherence time between any two levels. The model to calculate the coherence time is an integral part of the model to calculate the carrier transport as the coherence time will affect the carrier transport due to coherent mechanism. In particular, we will implement the carrier transport calculation model for the QCL structure of Sirtori *et al.* [3]. A similar structure has been used by Woerner *et al.* [111] for their pump-probe experiments. We will calculate time-resolved carrier densities at each of the levels so that a clear illustration of the effects of the underlying physical processes can be obtained. We will show how carriers are distributed at different energy levels when a bias electric field is applied across the laser and how current increases significantly when the applied electric field brings the levels in the injector and active regions close to resonance. We will show that coherence between the injector and the active region levels decays more rapidly as the temperature increases, which reduces the carrier transfer due to tunneling. We will also show that coherence decays at a rapid rate at an increased carrier density, thereby reducing the rate of carrier transfer between the injector and active regions.

The remainder of this chapter is organized as follows: Sec. 5.2 describes the carrier transport model. A model for the calculation of the coherence time is also described and the scattering time between any two levels is defined. In Sec. 5.3, the carrier transport is studied as the applied electric field varies. We present the effects of varying the temperature on carrier transport in Sec. 5.4, while the effects of varying the doping density are discussed in Sec. 5.5. Section 5.6 summarizes the work on carrier transport of QCLs presented and discussed in this chapter.

5.2 Theoretical Model

A number of different approaches have been used in the literature to calculate carrier transport through QCLs [144, 159, 164–169]. We write the density equations in a way that correctly includes both incoherent scattering and coherent tunneling mechanisms in the model. To include the carrier transport due to tunneling, a level in the active region is coherently coupled to any level of the preceding and following injector regions. Similarly, any level in the injector region is coherently coupled to any level in the preceding and following active regions. In Fig. 5.1, we show an example how the carrier density equations are formulated in our model. The density equations can be written as

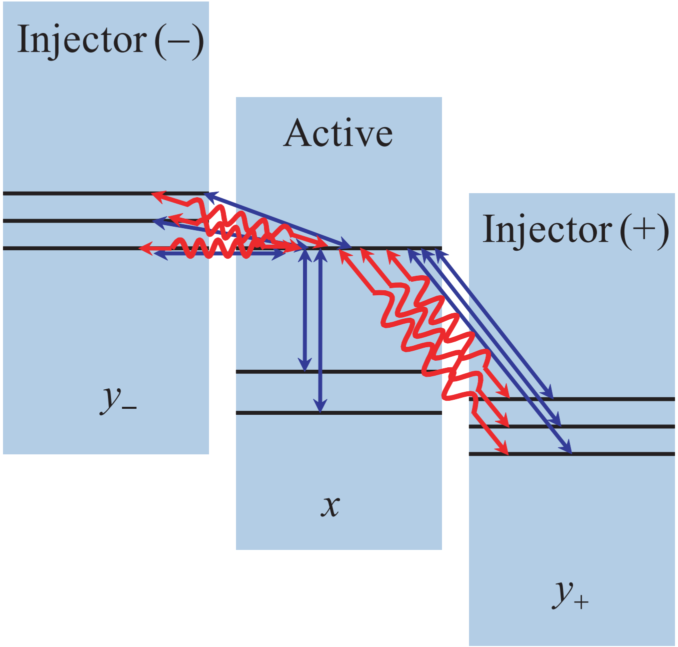

FIGURE 5.1: Schematic illustration of the carrier transport model. We show how the carrier density in a level in the active region is related to the other levels in the system. The blue straight arrows represent incoherent scattering mechanisms. The red wavy arrows indicate coherent carrier transport. We use double arrows for both incoherent and incoherent mechanisms to signify that the carrier transport can be in either direction.

$$\begin{aligned}
\frac{dn_{A,x}}{dt} &= \sum_{x'\neq x}\frac{n_{A,x'}}{s_{x'x}} + \sum_{y_-}\frac{n_{I,y-}}{s_{y_-x}} + \sum_{y+}\frac{n_{I,y+}}{s_{y+x}} - \sum_{y-}\frac{n_{A,x}}{s_{xy_-}} - \sum_{x'\neq x}\frac{n_{A,x}}{s_{xx'}} - \sum_{y+}\frac{n_{A,x}}{s_{xy+}} \\
&\quad - i\frac{\Delta_{0,xy+}}{2\hbar}\sum_{y+}(C_{xy_+} - C^*_{xy_+}) + i\frac{\Delta_{0,y_-x}}{2\hbar}\sum_{y_-}(C_{y_-x} - C^*_{y_-x}), \qquad (5.1a) \\
\frac{dn_{I,y-}}{dt} &= \sum_{y'_-\neq y_-}\frac{n_{I,y'_-}}{s_{y'_-y_-}} + \sum_{x}\frac{n_{A,x}}{s_{xy+}} + \sum_{x}\frac{n_{A,x}}{s_{xy_-}} - \sum_{x}\frac{n_{I,y_-}}{s_{y_-x}} - \sum_{x}\frac{n_{I,y+}}{s_{y+x}} - \sum_{y'_-\neq y_-}\frac{n_{I,y-}}{s_{y_-y'_-}} \\
&\quad - i\frac{\Delta_{0,y_-x}}{2\hbar}\sum_{x}(C_{y_-x} - C^*_{y_-x}) + i\frac{\Delta_{0,xy+}}{2\hbar}\sum_{x}(C_{xy_+} - C^*_{xy_+}), \qquad (5.1b) \\
\frac{dn_{I,y+}}{dt} &= \sum_{y'_+\neq y_+}\frac{n_{I,y'_+}}{s_{y'_+y_+}} + \sum_{x}\frac{n_{A,x}}{s_{xy_+}} + \sum_{x}\frac{n_{A,x}}{s_{xy_-}} - \sum_{y'_+\neq y_+}\frac{n_{I,y+}}{s_{y_+y'_+}} - \sum_{x}\frac{n_{I,y+}}{s_{y+x}} - \sum_{x}\frac{n_{I,y_-}}{s_{y_-x}} \\
&\quad - i\frac{\Delta_{0,y_-x}}{2\hbar}\sum_{x}(C_{y_-x} - C^*_{y_-x}) + i\frac{\Delta_{0,xy+}}{2\hbar}\sum_{x}(C_{xy_+} - C^*_{xy_+}), \qquad (5.1c) \\
\frac{dC_{xy_+}}{dt} &= i\frac{\Delta_{0,xy+}}{2\hbar}(n_{I,y_+} - n_{A,x}) - \frac{C_{xy_+}}{T_{2,xy+}} - i\frac{E_{xy+}}{\hbar}C_{xy_+}, \qquad (5.1d) \\
\frac{dC_{y_-x}}{dt} &= i\frac{\Delta_{0,y_-x}}{2\hbar}(n_{A,x} - n_{I,y_-}) - \frac{C_{y_-x}}{T_{2,y_-x}} - i\frac{E_{y_-x}}{\hbar}C_{y_-x}. \qquad (5.1e)
\end{aligned}$$

In the formulation of the density Eq. (5.1), we take an active region and two injector regions preceding and following the active region. In Eq. (5.1), the quantity n is the carrier density in the levels of the active and injector regions. Subscripts A and I denote active and injector regions, respectively. Indices x and y indicate the levels in the active and injector regions, respectively. Subscripts $-$ and $+$ indicate a quantity in the injector region that precedes and follows the active region, respectively. The quantity C_{xy} denotes the coherence between levels x and y. The parameter s_{xy} denotes the scattering time between levels x and y. The parameter $\Delta_{0,xy}$ denotes the energy splitting at resonance between levels x and y involved in tunneling, while E_{xy} is the detuning of the energy of level x (E_x) and the energy of level y (E_y) from resonance. The parameter $T_{2,xy}$ is the coherence time between levels x and y.

If two energy levels of two neighboring quantum wells that are separated by a potential barrier are coherently coupled, the electron wave-packets can propagate or tunnel through the barrier from one energy level to another [2, 170]. Before achieving steady-state values, electron wave-packets make Rabi oscillations between the levels [162]. This coherent transport depends on the strength of the coherence, how long the coherence exists, and the detuning of the levels from resonance. The strength of the coherence depends on the energy splitting of the levels at resonance, which in turn depends on the thickness and the height of the barrier between neighboring quantum wells [162, 171]. The greater the thickness of the barrier or the higher the height of the barrier, the weaker the coherence between the levels becomes. The barrier thickness is a design parameter, while the barrier height depends on the choice of the material system. Since in QCLs electron tunneling is most important from the injector ground level to the upper lasing level, and those two levels are in two neighboring quantum wells separated by the injection barrier, the selection of the thickness of the barrier has a significant role in determining the tunneling transport rate. The time it takes to destroy the coherence between two levels is often called the coherence time. While propagating, electronic wave-packets lose phase coherence mainly due to scattering by LO phonons, coulombic potential from other electrons in the subband, and interface roughness in the well and barrier materials. These scattering times depend on the quantum mechanical design, quality of the interfaces during the growth of the heterostructure, carrier density, and temperature. As a consequence, so does the coherence time. The detuning of the levels from resonance depends on the applied electric field. When there is no detuning, i.e. the electric field brings the levels in the injector and active regions to the same energy so that they are in resonance, then the carrier transport is maximized.

5.2.1 Coherence Time $T_{2,xy}$

The coherence between any two levels x and y decays in a time $T_{2,xy}$, as the propagating electronic wave-packets lose phase coherence mainly due to intrasubband scattering. The scattering mechanisms that dominate the coherence decay are electron-electron scattering, electron-LO phonon scattering, and electron-interface roughness scattering [111, 112]. So, the coherence time $T_{2,xy}$ between levels x and y can be written as

$$\frac{1}{T_{2,xy}} = \frac{1}{T_{2,xy}^{\text{electron}}} + \frac{1}{T_{2,xy}^{\text{phonon}}} + \frac{1}{T_{2,xy}^{\text{roughness}}}, \tag{5.2}$$

where $T_{2,xy}^{\text{electron}}$, $T_{2,xy}^{\text{phonon}}$, and $T_{2,xy}^{\text{roughness}}$ are the contributions to the coherence time $T_{2,xy}$ by scattering due to electrons, LO phonons, and interface roughness, respectively.

The scattering of an electron in subband x due to an electron or an LO phonon is uncorrelated with the scattering of an electron in subband y due to an electron or an LO phonon. Therefore, intrasubband electron-electron and electron-LO phonon transitions in levels x and y separately contribute to the loss of phase coherence and the rates add linearly. In our model, we consider the dominant intrasubband electron-electron transitions, i.e., $x, x \rightarrow x, x$ and $y, y \rightarrow y, y$, and we neglect the less significant intrasubband electron-electron scattering, such as

$x, y \rightarrow x, y$, in order to reduce the computational burden. However, we have seen that the results do not change by a noticeable amount when $x, y \rightarrow x, y$ electron-electron scattering is included in the model. Therefore, the contribution of electron-electron scattering to the coherence time can be written as

$$\frac{1}{T_{2,xy}^{\text{electron}}} = \frac{1}{s_{x,x\rightarrow x,x}^{\text{electron}}} + \frac{1}{s_{y,y\rightarrow y,y}^{\text{electron}}}, \tag{5.3}$$

where $s_{x,x\rightarrow x,x}^{\text{electron}}$ is the scattering lifetime due to $x, x \rightarrow x, x$ electron-electron transitions. For electron-LO phonon scattering, an electron may scatter by emitting an LO phonon or by absorbing an LO phonon. Though electron scattering due to LO phonon absorption is not significant in intersubband transitions, it is as significant as scattering due to LO phonon emission in intrasubband transitions [148]. Hence, scattering due to both LO phonon emission and LO phonon absorption in both x and y levels should be included to calculate $T_{2,xy}$. Therefore, we write

$$\frac{1}{T_{2,xy}^{\text{phonon}}} = \frac{1}{s_{x\rightarrow x}^{\text{phonon,abs}}} + \frac{1}{s_{x\rightarrow x}^{\text{phonon,em}}} + \frac{1}{s_{y\rightarrow y}^{\text{phonon,abs}}} + \frac{1}{s_{y\rightarrow y}^{\text{phonon,em}}}, \tag{5.4}$$

where $s_{x\rightarrow x}^{\text{phonon}}$ is the scattering lifetime due to $x \rightarrow x$ electron-LO phonon transitions, and the superscripts "abs" and "em" denote absorption and emission, respectively. The intrasubband scattering due to interface-roughness in levels x and y is correlated. Non-uniformity in a surface between two alternating materials causes a change in the energy of all the electrons that have a finite probability of existence near that interface. Therefore, the intrasubband scattering rate in level x and the intrasubband scattering rate in level y due to interface roughness cannot be linearly added when calculating the coherence time. Instead, we write [112, 146]

$$\frac{1}{T_{2,xy}^{\text{roughness}}} = \frac{1}{s_{x\rightarrow x}^{\text{roughness}}} + \frac{1}{s_{y\rightarrow y}^{\text{roughness}}} - 2\,\frac{1}{\sqrt{s_{x\rightarrow x}^{\text{roughness}}\, s_{y\rightarrow y}^{\text{roughness}}}}, \tag{5.5}$$

where $s_{x\to x}^{\text{roughness}}$ is the scattering lifetime due to $x \to x$ electron-interface roughness transitions.

5.2.2 Scattering Time s_{xy}

We next define the scattering time s_{xy} used in our model. As previously stated, electron-LO phonon intersubband scattering is the dominant intersubband scattering mechanism. However, electron-electron scattering plays a role when the level energies are sufficiently close to one another that LO phonon transitions are forbidden except for the electrons in the high energy tails at a high temperature. Though intrasubband transitions due to interface roughness may be significant, intersubband electron-interface roughness transition rates are orders of magnitude smaller than LO phonon transition rates or even electron-electron transition rates [156]. Therefore, in our model described in Eq. (5.1), we calculate the scattering time of an electron between levels x and y by

$$\frac{1}{s_{xy}} = \frac{1}{s_{xy}^{\text{phonon}}} + \frac{1}{s_{xy}^{\text{electron}}}. \tag{5.6}$$

where s_{xy}^{phonon} and s_{xy}^{electron} are the scattering lifetimes of an electron between levels x and y due to electron-LO phonon and electron-electron interactions, respectively. The contribution of the electron-LO phonon scattering to the transition rate from level x to level y in Eq. (5.1), where $x \neq y$ is given by

$$\frac{1}{s_{xy}^{\text{phonon}}} = \frac{1}{s_{x\to y}^{\text{phonon}}}. \tag{5.7}$$

Both emission and absorption of LO phonons contribute to $1/s_{x\to y}^{\text{phonon}}$, and both depend on the relative energies of levels x and y. To determine the contribution of electron-electron scattering to the transition rate from level x to level y in Eq. (5.1), one must sum the contributions from all the possible transitions in which one electron leaves level x, decreasing the population there by one electron, and then one must sum the contribution when one electron arrives in level y, increasing the population there by one electron. Hence, we find

$$\frac{1}{s_{xy}^{\text{electron}}} = \sum_{x' \neq y, y' \neq x} \frac{1}{s_{x,x' \rightarrow y,y'}^{\text{electron}}}. \tag{5.8}$$

We calculate the time-resolved solutions of Eq. (5.1) so that transient carrier transport phenomena can be better visualized and the underlying physics can be explained. Initially, we put all the carriers of a period in the injector levels of that period. Therefore, when we start, all the active region levels are empty. With time, the carrier density in each level changes. As the scattering and coherence times depend on the carrier density, we recalculate these parameters as the carriers evolve until the carriers reach their steady-state values.

5.3 Carrier Transport with Electric Field

In this section, we will calculate the carrier density in the levels of the injector and active regions when an external applied electric field is varied. In Fig. 5.2, we present the conduction band energy diagram and the modulus-squared wavefunctions of the QCL structure with an applied electric field of (a) 40 kV/cm, (b) 50 kV/cm, (c) 60 kV/cm, and (d) 70 kV/cm. In each case, levels 1–3 are in the active region and levels 4–8 are in the injector region. The energy splitting at resonance between the injector and the lasing levels is given in Table 5.1. With an applied electric field of 40 kV/cm, the injector and active region levels are not properly aligned to allow coherent carrier transport between them. The energy of the upper lasing level (level 3) in the active region differs significantly from the energy of the injector ground level (level 4) and the lower two levels in the active region are also out of resonance with the following injector levels. With an applied electric field of 50 kV/cm, the injector and active region levels are better aligned to allow carrier transport by tunneling. Though the upper lasing level is not at resonance with the injector ground level, the detuning is small. The same is true for the lower two levels of the active region and the following injector levels. When an electric

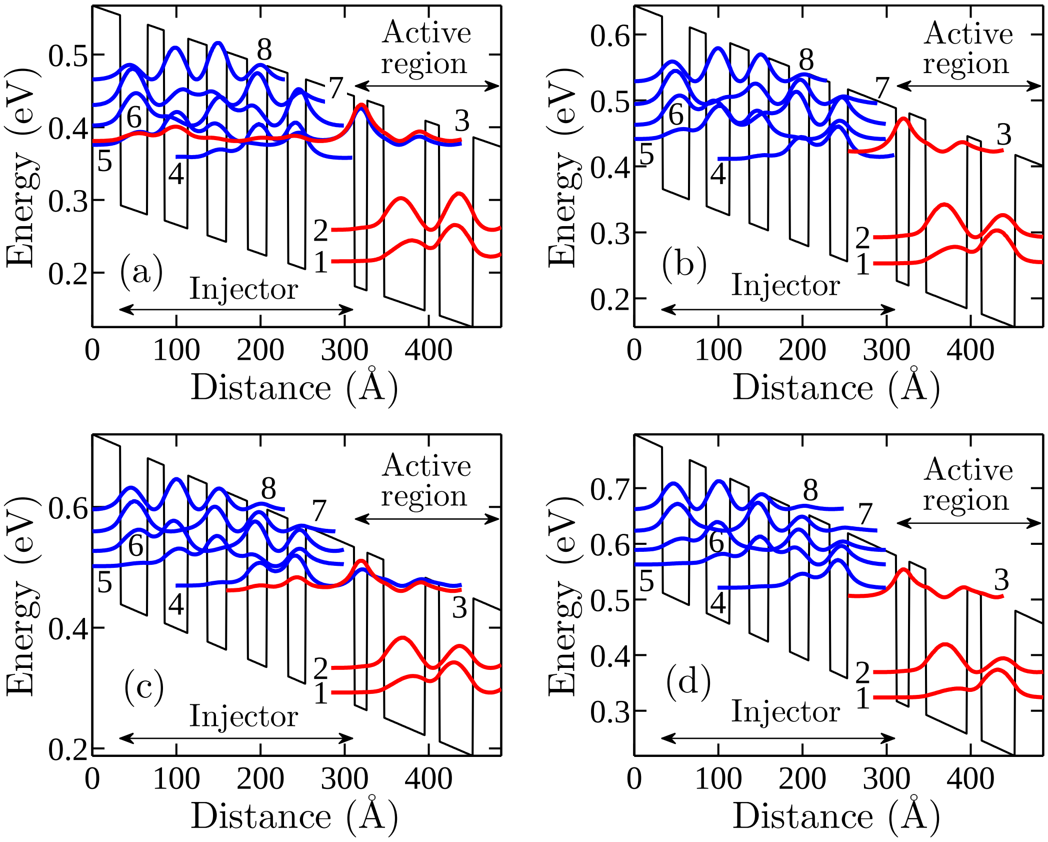

FIGURE 5.2: Conduction band diagram and modulus-squared wavefunctions of the QCL of Sirtori *et al.* [3]. The applied electric field is (a) 40 kV/cm, (b) 50 kV/cm, (c) 60 kV/cm, and (d) 70 kV/cm.

field of 60 kV/cm is applied, the injector and active region levels are almost in resonance with respect to each other, allowing for coherent carrier transport. With this bias electric field, the energy spacing between the injector ground and active region upper lasing level (8.5 meV) is close to the resonant energy splitting (8 meV). The lower levels of the active region are also nearly in resonance with the following injector levels. The energy separation between levels 3 and 4 increases when the electric field further increases to 70 kV/cm in Fig. 5.2(d).

We have calculated the time evolution of the carrier density at each level of the QCL when the applied electric field is varied. We present the time evolution of the carrier density with an electric field of (a) 40 kV/cm, (b) 50 kV/cm, (c) 60 kV/cm, and (d) 70 kV/cm in Fig. 5.3. In Fig. 5.3(a), due to a large detuning between the levels of the injector and the active region with an electric field of 40 kV/cm,

x, y	Δ_0 (meV)	x, y	Δ_0 (meV)	x, y	Δ_0 (meV)
$1, 4_-$	1	$2, 4_-$	1	$3, 4_-$	8
$1, 5_-$	1	$2, 5_-$	1	$3, 5_-$	5
$1, 6_-$	1	$2, 6_-$	1	$3, 6_-$	8
$1, 7_-$	1	$2, 7_-$	1	$3, 7_-$	9
$1, 8_-$	3	$2, 8_-$	3	$3, 8_-$	11
$1, 4_+$	3	$2, 4_+$	11	$3, 4_+$	5
$1, 5_+$	5	$2, 5_+$	7	$3, 5_+$	4
$1, 6_+$	6	$2, 6_+$	9	$3, 6_+$	2
$1, 7_+$	10	$2, 7_+$	10	$3, 7_+$	2
$1, 8_+$	14	$2, 8_+$	9	$3, 8_+$	2

TABLE 5.1: Resonance energy splitting between the injector and active region levels.

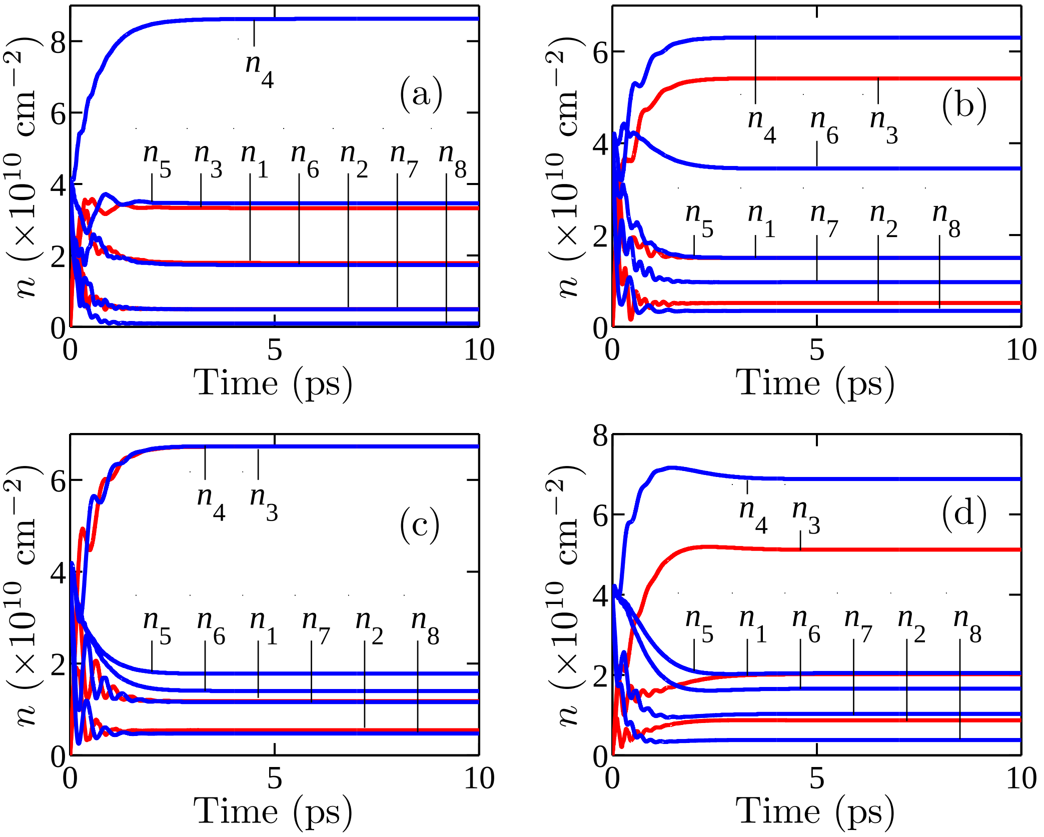

FIGURE 5.3: Time evolution of carrier density at different levels in the QCL structure of Sirtori *et al.* [3]. The applied electric field is (a) 40 kV/cm, (b) 50 kV/cm, (c) 60 kV/cm, and (d) 70 kV/cm. The total carrier density per period is 2×10^{11} cm^{-2}.

carrier injection into the active region and extraction from the active region are affected. We do not observe pronounced Rabi oscillations in the evolution of the carrier densities. We note that electrons accumulate at level 4 due to inefficient tunneling at level 3. At the same time, level 2 in the active region and levels 6, 7, and 8 in the injector scatter electrons to the lower energy levels in their respective regions at a greater rate than the electron tunneling rate between injector and active regions, mainly by emitting LO phonon. Therefore, the steady-state carrier density of these levels is lower than the carrier density of levels 3 and 4. With an electric field of 50 kV/cm applied to the laser, a large fraction of the carrier transfer is due to tunneling because the detuning between the corresponding levels in the injector and active region levels is small. Therefore, in Fig. 5.3(b), we note the increased presence of Rabi oscillations in the time evolution of the carrier densities. Level 6 is far from resonance with any of the active region levels; so, very few Rabi oscillations are visible in the time evolution of n_6. The carrier density in level 3, n_3, is much higher than when the electric field is 40 kV/cm and is close to n_4. This particular QCL reaches threshold when 48 kV/cm is applied to it. With an electric field of 60 kV/cm applied to the QCL, the injector and active region levels are almost at resonance. Carrier transfer due to tunneling increases significantly. As a consequence, pronounced Rabi oscillations are visible in the time evolution of n_3 and n_4, n_1 and n_7, and n_2 and n_8. The carrier density in the corresponding active and injector region levels are almost equal, i.e., $n_3 \approx n_4$, $n_1 \approx n_7$, and $n_2 \approx n_8$. With an electric field of 70 kV/cm in Fig. 5.3(d), Rabi oscillations in the time evolution of the carrier densities diminish. We note that n_4 and n_1 increase and n_3 decrease again due to inefficient electron injection and extraction.

In Fig. 5.4, we plot the current density through the QCL as a function of the applied electric field. We see that little current flows when the electric field is < 40 kV/cm. However, as the electric field increases further, the current density increases significantly. The increase occurs at the point that the injector ground and active region upper lasing levels begin to align, leading to a rapid increase in the carrier tunneling between the injector and active regions.

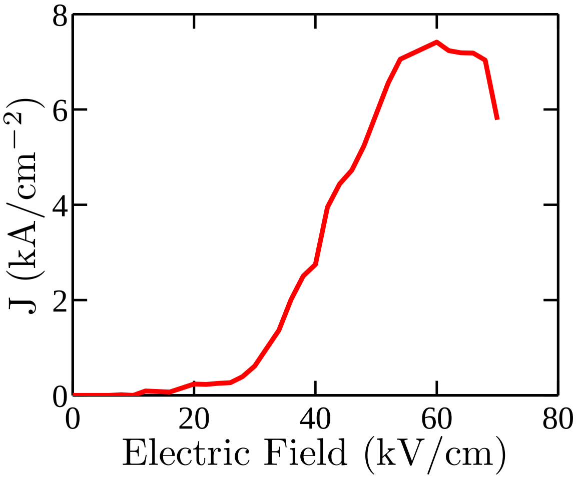

FIGURE 5.4: Current density through the QCL as a function of the applied electric field. The total carrier density per period is 2×10^{11} cm^{-2}.

5.4 Effects of Temperature

Generally, the performance of a QCL becomes worse as the temperature rises. In work to date, this performance degradation has been mainly attributed to the scattering of electrons from the injector and the upper lasing levels to levels that are not localized within the conduction band [144]. Therefore, the number of electrons that take part in the radiative process decreases. A portion of the degradation has also been attributed to electron back-scattering from the injector levels to the lower lasing level, thus reducing the population inversion [144]. This work did not take into account the breakdown of coherence between the injector and active region levels when the temperature rises. This coherence breakdown leads to a decrease in the tunneling rate between the injector and active region levels.

We find that the increased rate of the decay of the coherence between injector and active region levels significantly contributes to the performance drop at higher temperature. The rate of electron scattering depends on the temperature. In particular, the rate of intrasubband scattering of electrons due to LO phonons and electrons increases significantly when the temperature increases. The increased rate of electron scattering at an increased temperature destroys the phase coherence of the propagating electrons that is needed for tunneling. In this section, we will study the change in the carrier transport with temperature. We will show that carrier transport between the injector and active regions decreases when the temperature increases.

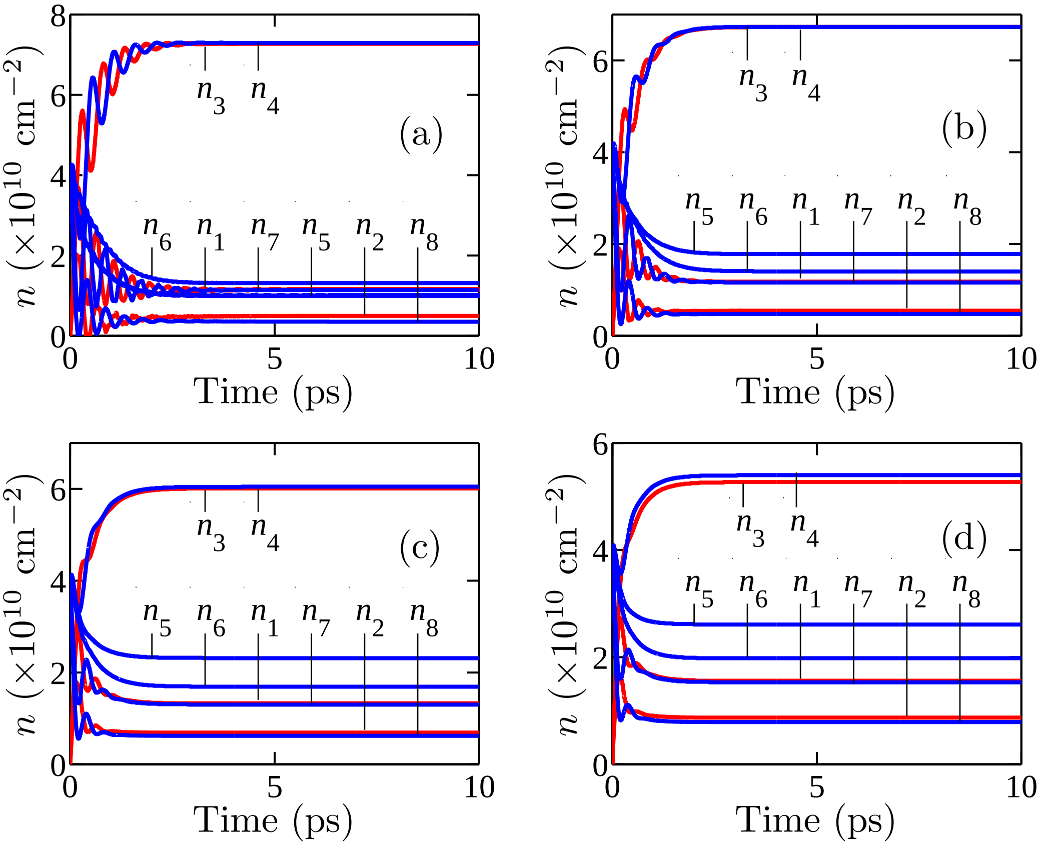

FIGURE 5.5: Time evolution of carrier density at different levels in the QCL of Sirtori *et al.* [3]. The applied electric field is 60 kV/cm, and the total carrier density per period is 2×10^{11} cm^{-2}. The temperature is (a) $T = 100$ K, (b) $T = 200$ K, (c) $T = 300$ K, and (d) $T = 400$ K.

We present the time evolution of the carrier density at each level of the QCL structure with a temperature of (a) 100 K, (b) 200 K, (c) 300 K, and (d) 400 K in Fig. 5.5. The total number of carriers (N_d) in each period is 2×10^{11} cm^{-2} and the QCL is biased with an electric field of 60 kV/cm in each case. In Fig. 5.5(a), when $T = 100$ K, the carriers oscillate between the levels before settling down to a steady-state value due to significant coherent carrier transport and a slow decay of the coherence between the injector and active region levels. In this case, carrier injection into the active region and extraction from the active region are efficient. We note that the upper lasing level has nearly equal carrier density as in the injector ground level, i.e., $n_3 \approx n_4$. We also note that n_3 and n_4 are much greater than the carrier densities of other levels. Therefore, backscattering is less than at higher temperatures. As the temperature increases further, the coherence time between the injector and active region levels diminishes. Therefore, fewer oscillations are visible in Figs. 5.5(b)–5.5(d) and the density n_3 decreases. Even when the corresponding levels in the injector and active regions are close to resonance, coherent transport decreases as the temperature rises. We note that n_4 drops as electrons back-scatter to the upper energy levels, thereby further decreasing n_3. Therefore, the densities n_1, n_2, n_6, n_7, and n_8 increase when the temperature increases.

In Fig. 5.6, we show the steady-state carrier density at each level in the injector and active region as the temperature varies. The densities n_3 and n_4 decrease with temperature, while, n_1, n_2, n_6, n_7, and n_8 increase as temperature increases. These density changes are due to the decrease of the coherent carrier transport at a higher temperature and increase of backscattering of electrons from level 3 and level 4 to the higher energy levels in the injector and the lower active region levels of the previous period.

We plot the values of the coherence time between the injector ground level and the upper lasing level ($T_{2,34}$) vs. temperature in Fig. 5.7 for three different total carrier densities per period. The coherence time monotonically decreases with temperature. However, the rate of decrease is larger at temperatures that are less than 200 K. At temperatures that are greater than 400 K, we find that the temperature effects saturate. The coherence time also strongly depends on the total number of carriers in a period (N_d). The coherence time is 0.54 ps at 100 K with 1×10^{11} cm^{-2} carriers in one period, while it is only 0.18 ps at the same temperature with 4×10^{11} cm^{-2} carriers in one period.

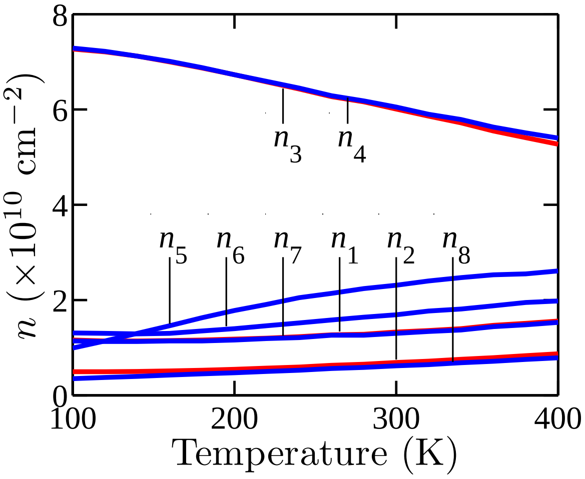

FIGURE 5.6: Carrier density at different levels vs. temperature. The applied electric field is 60 kV/cm, and the total carrier density per period is 2×10^{11} cm^{-2}.

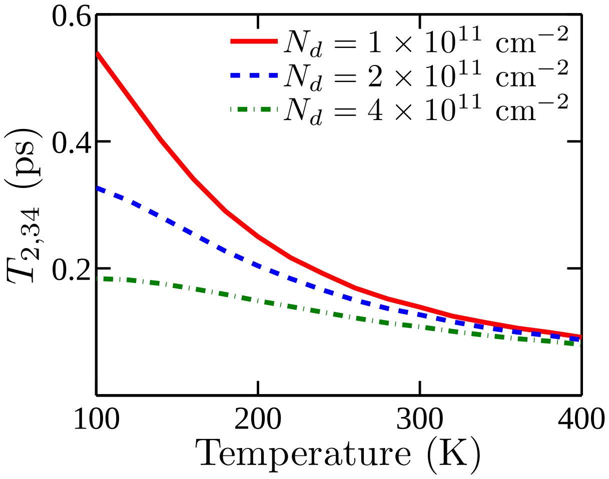

FIGURE 5.7: Coherence time between the upper lasing level (level 3) and the injector ground level (level 4) vs. temperature. The applied electric field is 60 kV/cm and total carrier density per period is 2×10^{11} cm^{-2}.

5.5 Effects of Doping Density

Next, we study the effects of doping density (N_d) on the coherence between levels and on the carrier transport. We assume that the total carrier density in a QCL period equals the total doping density in that period. We show the time evolution of the carrier density at each level in the injector and active region with (a) $N_d = 1 \times 10^{11}$ cm^{-2}, (b) $N_d = 4 \times 10^{11}$ cm^{-2}, (c) $N_d = 7 \times 10^{11}$ cm^{-2}, and (d) $N_d =$

10×10^{11} cm^{-2} in Fig. 5.8. In all cases, the temperature is fixed at 200 K and the applied electric field is 60 kV/cm. Since the total carrier density per period increases, the carrier density at each level increases from Fig. 5.8(a) to 5.8(d). However, we note that the number of Rabi oscillations in the time evolution of the carrier density decreases as the total carrier density per period increases, which is due to a decrease in the coherence times. Rabi oscillations are more pronounced in the time evolution of the carrier densities in the injector and active region levels with $N_d = 1 \times 10^{11}$ cm^{-2} than in other cases. Carriers move easily from the injector into the active region. Therefore, the carrier densities in levels 3 and 4 are approximately equal. However, as the carrier density per period increases, Rabi oscillations diminish and coherent current transport ultimately ceases. As a result, the difference between n_3 and n_4 becomes wider as shown in Figs. 5.8(c) and 5.8(d).

In Fig. 5.9, we show the upper lasing level carrier density (n_3) vs. the total number of carriers in one period for three different temperatures. The slope dn_3/dN_d decreases as N_d increases. We also note the temperature dependence. At a fixed value of N_d, the density n_3 is smaller at a higher temperature. Also, the decrease of dn_3/dN_d as N_d increases is greater at a higher temperature.

The phenomena observed in Figs. 5.8 and 5.9 are due to the change in the coherence time between the injector and active region levels. Due to its significance for the carrier transport, we focus on the coherence time between the injector ground level and active region upper lasing level. We denote this time as $T_{2,34}$. The calculated values of $T_{2,34}$ at three different temperatures are plotted as a function of N_d in Fig. 5.10. We see that $T_{2,34}$ decreases as N_d increases. The rate of decrease of $T_{2,34}$ is higher at a smaller temperature. Also at a fixed N_d, the time $T_{2,34}$ is greater at a smaller temperature. Therefore, we find that at a higher temperature and a higher carrier density, coherent carrier transport is significantly diminished.

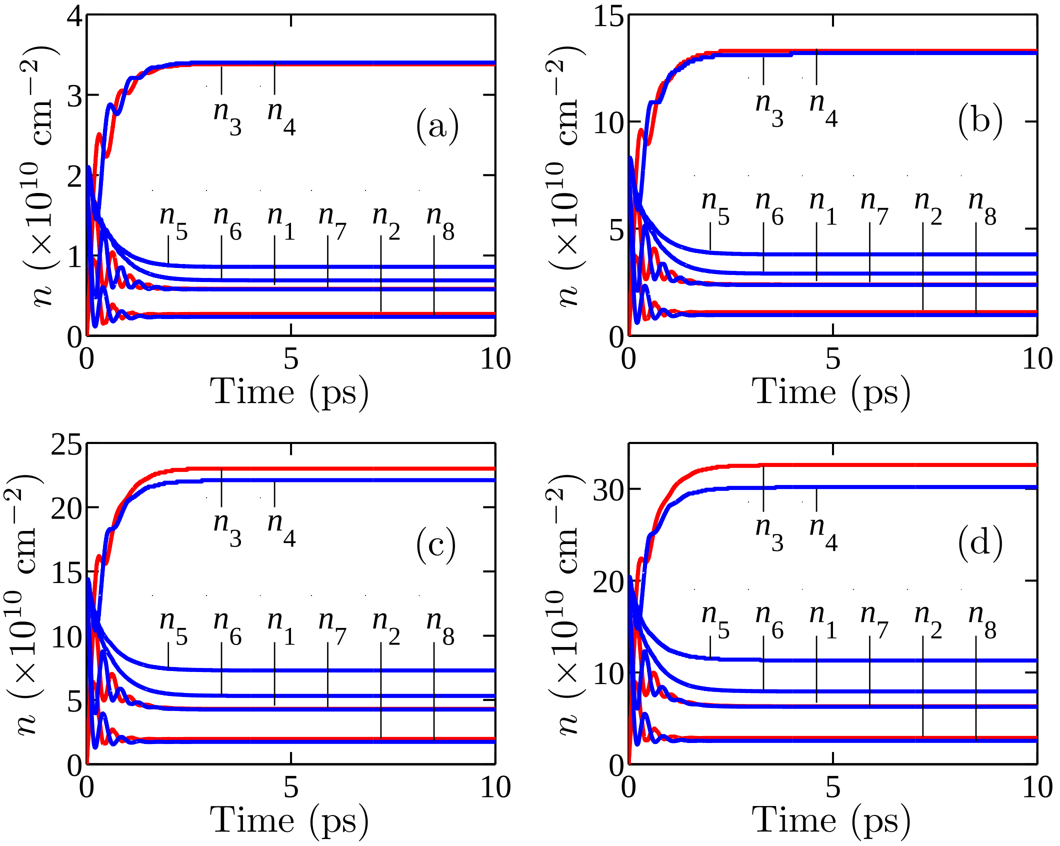

FIGURE 5.8: Time evolution of the carrier density at different levels in the QCL of Sirtori *et al.* [3]. The applied electric field is 60 kV/cm, and the electron temperature is 200 K. The total carrier density per period is (a) $N_d = 1 \times 10^{11}$ cm^{-2}, (b) $N_d = 4 \times 10^{11}$ cm^{-2}, (c) $N_d = 7 \times 10^{11}$ cm^{-2}, and (d) $N_d = 10 \times 10^{11}$ cm^{-2}.

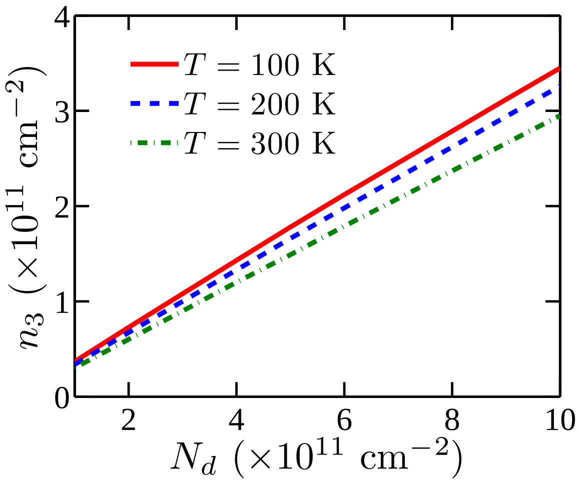

FIGURE 5.9: Upper lasing level (level 3) carrier density (n_3) vs. total carrier density per period (N_d) at different temperatures. The applied electric field is 60 kV/cm.

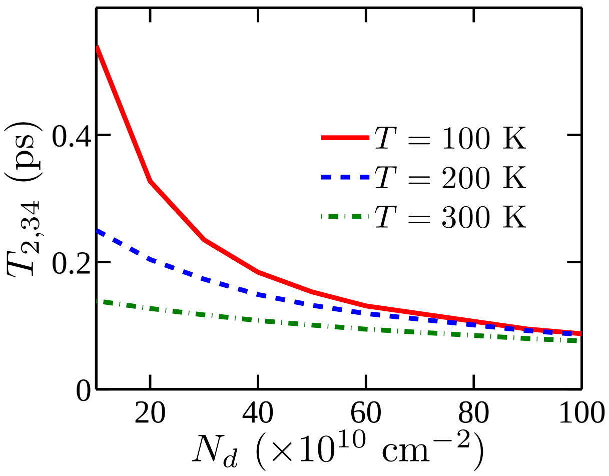

FIGURE 5.10: Coherence time between the upper lasing level (level 3) and the injector ground level (level 4) vs. total carrier density per period. The applied electric field is 60 kV/cm.

5.6 Conclusion

We have developed a model to calculate the carrier transport of QCLs that includes both coherent tunneling and incoherent scattering mechanisms. In particular, we calculated the coherence times between injector and active region levels and included its effect in the carrier transport calculation. We extensively investigated the carrier transport in the QCL structure of Sirotori *et al.* [3] as the operating conditions change. We showed the dependence of carrier transport on applied electric field, on temperature, and on carrier density. We found that resonant or non-resonant tunneling mechanisms increases the current significantly when the applied electric field aligns the injector levels with the appropriate active region levels. However, the coherent tunneling contribution of carrier transport is reduced when the temperature increases or the carrier density in the levels increases due to the rapid decay of phase coherence of the propagating electrons.

In this analysis, we have assumed that the lattice and the electrons of the QCL have the same temperature. In practice, the lattice and the electrons will have different temperatures with electron temperature always greater than the lattice temperature. Electron temperature can be significantly higher than the lattice temperature for continuous wave and high-power operation of the laser. Therefore, the phenomena discussed in this chapter should be observed at a lower lattice temperature. The values of the coherence time estimated in this work are somewhat over-estimated. We have calculated the coherence time by including all possible electron-LO phonon scattering, electron-interface roughness scattering, and dominant $x, x \rightarrow x, x$ and $y, y \rightarrow y, y$ electron-electron scattering. There are other scattering mechanisms such as $x, y \rightarrow x, y$ electron-electron scattering, electron-acoustic phonon scattering, and electron-impurity scattering that if included in the model would slightly decrease the calculated coherence times.

Chapter 6

QCL Structures for SIT Modelocking

6.1 Introduction

A QCL structure that can modelock using the SIT effect differs from conventional QCL structures. The most distinctive difference is the introduction of periods that will produce loss rather than producing gain. In this chapter, we will discuss the design issues that must be addressed to create an SIT modelocked QCL. We will present realistic QCL designs with interleaved gain and absorbing periods that satisfy the requirements for SIT modelocking. We will also present the calculated stability limits of $\bar{g}$ and $\bar{a}$ for a modelocked QCL structure and the curves within the stability region that correspond to different ratios of the gain to absorbing periods. The QCL theory and the modeling concepts described in Chapter 4 have been used to design and characterize these QCL structures. The models for the calculation of carrier transport and coherence time developed in Chapter 5 have been used to determine carrier densities at the resonant levels and the coherence time between the resonant levels of the gain and absorbing periods.

The remainder of this chapter is organized as follows: Sec. 6.2 discusses the principal issues that should be considered in the design of an SIT modelocked QCL structure. In Sec. 6.3, we will present two QCL structures, one emitting at ~ 8 μm and the other emitting at ~ 12 μm, that have interleaved gain and absorbing periods, and we will show that these structures satisfy the requirements for SIT modelocking. In Sec. 6.4, we will discuss the ratio of the gain to absorbing periods that is required for the laser to operate stably. Section 6.5 concludes this chapter.

6.2 Design Issues

The design of an SIT modelocked QCL is different from that of a standard QCL as it will have absorbing periods in addition to the gain periods; absorbing and gain periods have to appear in a ratio that falls between limits that must be calculated; and the values of the coherence time T_2, the gain recovery time T_1, and the lifetimes of the two resonant levels in the gain and absorbing periods affect the stability limits on the gain and absorption per unit length and the corresponding ratio of the number of gain and absorbing periods.

The gain periods in SIT modelocked QCLs are conventional QCL structures. They are meant to produce gain, so that electrons are injected into the upper resonant level. On the contrary, the absorbing periods are meant to produce coherent absorption, so that the electrons are injected into the lower resonant level. Therefore, the relation between an injector and an active region in the absorbing periods is different from that in the gain periods, as the injector ground level should have nearly the same energy as the lower resonant level in the active region, rather than the upper resonant level. Since the electrons are injected into the lower resonant level in the absorbing periods, the upper resonant level may approach the conduction band edge and induce leakage of the carriers into the continuum or delocalized energy levels. One must design a structure that avoids this leakage. In the absorbing periods, electrons stay in the upper resonant level for half a Rabi oscillation period after being radiatively scattered from the lower resonant level. The leakage of any electrons during that time will reduce the coherent emission by the absorbing periods into the trailing edge of the pulse that is required for SIT [122]. Thus, a design objective is to ensure that the upper resonant level is below the energy of the conduction band edge by at least several times k_bT. Additionally, electrons may tunnel or scatter from the upper resonant level into the following injector region if there are energy levels in the following injector that couple well to the upper resonant level and whose energies are close to the energy of the upper resonant level. Therefore, the following injector region should be designed in a way that it acts as a Bragg reflector for the upper resonant level [172], so that electrons from the upper resonant level do not tunnel or scatter into the following injector region.

The radiative transition energy in the gain periods, $\hbar\omega_g$, must be close to the radiative transition energy in the absorbing periods, $\hbar\omega_a$. SIT is a resonant phenomenon. The pulses will be damped if they are comparable in duration to the coherence times T_{2g} or T_{2a} due to the decay of the polarization of the electrons in the resonant levels. Therefore, it is preferable for the coherence times to be as large as possible. The gain and absorption coefficients obtained from the gain and absorbing periods also depend directly on T_{2g} and T_{2a}, respectively. Therefore, large values of T_{2g} and T_{2a} will reduce the requirement on input current to produce the same amount of gain or absorption. The gain recovery time T_1 should be such that it is greater than the pulse duration and the coherence time but much shorter than the cavity round-trip time T_{rt}. A value of T_1 that is comparable to the cavity round-trip time will affect the stability, since, in that case, the gain does not have enough time to recover when the pulses bounce back from the edges and travel in the opposite direction. On the other hand, if the value of T_1 is comparable to the pulse duration, pulses cannot form as the pulse edges experience much higher gain due to the recovery of gain within its duration. This effect will lead to a long tail, which may then produce continuous waves and multiple pulses.

The upper resonant level in the gain period should have as long a lifetime as possible, while the lower resonant level should have as short a lifetime as possible, so that the population inversion is as large as possible. Additionally, a long upper resonant level lifetime will increase the number of the carriers that contribute to the radiation, which will reduce the required input current. The population inversion in the absorbing periods will always be close to -1 as electrons are injected into the lower resonant level. Nonetheless, the lower resonant level should have a long lifetime so that the current requirement is reduced.

Absorbing periods should have a dipole moment twice as large as the dipole moment in the gain periods. However, this requirement is not stringent. From the analysis in Chapter 3, we note that modelocking can be obtained when the ratio of the dipole moments in the absorbing periods and gain periods are as small as 1.2 and as large as ~ 5. However, a dipole moment ratio of more than 2 would be difficult to obtain while maintaining a large gain. When the dipole moment ratio is less than 2, the equilibrium pulses are broader than when the ratio is two. When the ratio is close to the limiting value of 1.2, the equilibrium pulses are broader by more than a factor two than when the dipole moment ratio is 2.

6.3 QCL Structures

In this section, we present and discuss the design of two QCL structures that fulfill the SIT modelocking requirements at two different wavelengths, i.e., at 8 and 12 μm. Similar structures can be designed over a broad range of mid-IR wavelengths. We use the $In_{0.52}Al_{0.48}As$ and $In_{0.53}Ga_{0.47}As$ material systems for barriers and wells, respectively, and the composition is lattice-matched to InP. To date, this material system is the most common for mid-IR QCLs. However, modelocking structures operating at less than 8 μm will be difficult to design using this material system. Since electrons are injected into the lower energy level in the absorbing periods, the upper energy level is close enough to the conduction band edge when the wavelength is below 8 μm to lead to a large increase in the carrier loss due to scattering to the continuum-like states. To design a modelocking structure at shorter wavelengths, it should be possible to use a strain-balanced InAlAs/InGaAs or Sb-based material systems that increases the conduction band offset between the wells and barriers.

The gain periods in our designs are typical QCL periods. We design a three-quantum-well active region for the gain periods that has a diagonal transition, which lowers the dipole moment relative to designs that have a vertical transition. This choice simplifies the design of the absorbing periods. Population inversion is achieved by confining the wavefunctions of the resonant levels in separate quantum wells and depopulating the lower resonant level through phonon relaxation to another level that is located below this lower resonant level. While the dipole moment in the gain periods is not high, the upper resonant level lifetime is larger than in the case of vertical transitions so that the gain remains high.

The design of the absorbing periods is different from the design of the gain periods. The combined requirements of carrier injection into and extraction from the lower resonant level and a dipole moment twice that of the gain periods makes it challenging to design the absorbing periods. To achieve a large dipole moment, the transition should be between two excited states that are extended over a number of wells. The carrier lifetime is made high by reducing scattering through phonon relaxation and reducing the carrier tunneling from the lower resonant level into the succeeding injector levels. The injector regions have different designs when the electrons are tunneling into a gain or absorbing active region due to the different quantum electronic structures of gain and absorbing active regions.

The QCL structure in Fig. 6.1(a) emits light at 12 μm. We present a QCL structure with one gain period and one absorbing period. Many such gain and absorbing periods will be used in an actual structure. The ratio of the number of gain to absorbing periods will be calculated later in this chapter. In the gain periods, electrons are injected into level 3g, and the gain transition is between

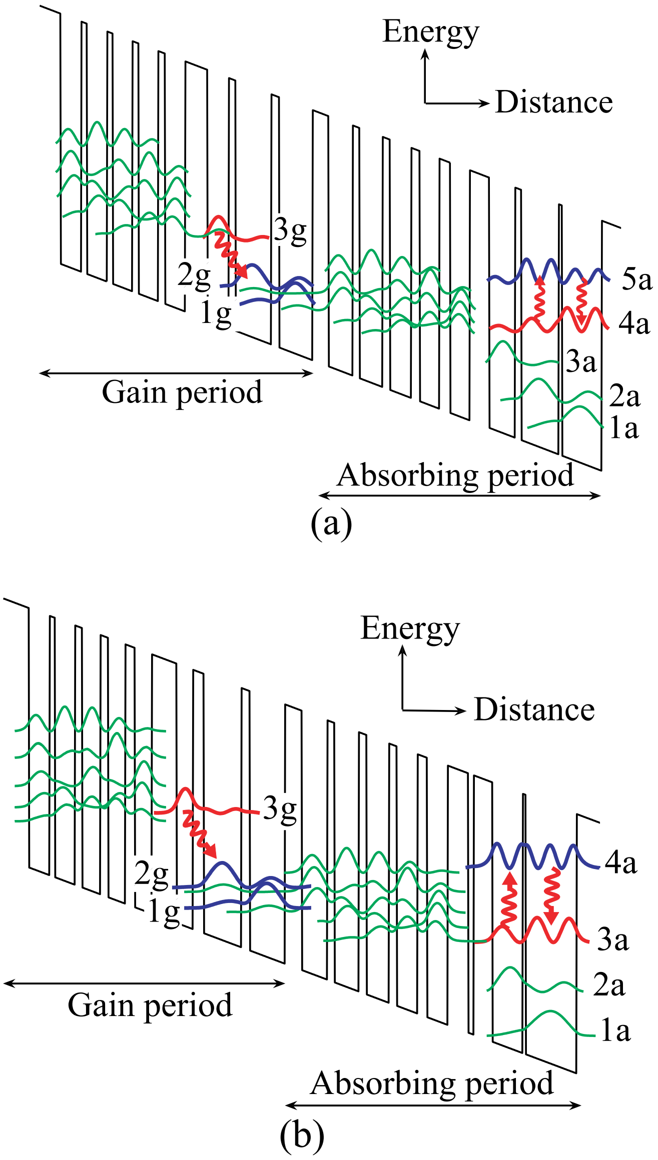
Energy
Distance
3g
2g
1g
5a
4a
3a
2a
1a
Gain period
Absorbing period
(a)
Energy
Distance
3g
2g
1g
4a
3a
2a
1a
Gain period
Absorbing period
(b)

FIGURE 6.1: Conduction band diagram and modulus-squared wavefunctions for one gain and one absorbing period of the (a) 12 μm, (b) 8 μm modelocking QCL structures. The sequence of layer dimensions is (in Å, starting from left): (a) **37**, 36, **10**, 35, **10**, 34, **11**, 34, **12**, 35, **39**, 37, **12**, 62, **14**, 58, **28**, 42, **12**, 40, **13**, 37, **15**, 34, **19**, 34, **34**, 45, **11**, 65, **6**, 69; (b) **42**, 34, **9**, 33, **12**, 30, **13**, 28, **16**, 28, **41**, 27, **18**, 62, **14**, 58, **28**, 42, **12**, 40, **13**, 37, **13**, 34, **16**, 34, **34**, 9, **31**, 50, **5**, 84. The numbers in bold type indicate $In_{0.52}Al_{0.48}As$ barrier layers and in roman type indicate $In_{0.53}Ga_{0.47}As$ well layers. Red wavy arrows indicate radiative transitions.

levels 3g and 2g. The dipole moment between the resonant levels is given by $\mu_g/e = 1.81$ nm, where e is the charge of an electron. Level 3g has a lifetime of ~ 2 ps. Level 1g is positioned approximately at phonon resonance with level 2g. Level 2g has a lifetime of ~ 0.5 ps, so that the population inversion is high. The radiative transition energy between levels 3g and 2g is 101 meV. In the absorbing periods, levels 4a and 5a are resonant with the levels 3g and 2g in the gain periods, i.e., the transition energy between levels 4a and 5a is 101 meV. In the absorbing period, the electrons are injected into the lower resonant level 4a. The dipole moment between levels 4a and 5a is $\mu_a/e = 3.65$ nm and level 5a has a lifetime of ~ 0.83 ps.

When an appropriate bias is applied across the QCL structure of Fig. 6.1(a), the injector ground level that precedes the active region of the gain period aligns with 3g, and the injector ground level that precedes the active region of absorbing period aligns with 4a. In this case, the gain periods will have a good population inversion as level 3g has a lifetime much greater than the lifetime of level 2g, and the absorbing period will have a population inversion ~ -1 since level 5a can always be considered empty. When the optical pulse propagates, the population in level 3g radiatively scatters to level 2g. Level 2g depopulates quickly to level 1g through interaction with LO phonons, and then the electrons are extracted from the active region by the following injector region. Since the gain recovery time will be much shorter compared to the cavity round-trip time, population inversion will be restored before the optical pulse arrives after bouncing back from the cavity edges, except in a very short region of the cavity near the edges. In absorbing periods, electrons stay in level 4a after being injected by the preceding injector range. When an optical pulse propagates through the absorbing periods, electrons from level 4a scatter to level 5a by absorbing photons. If the light pulse has sufficient energy to make a Rabi oscillation shorter than the coherence time of the levels, then the population from level 5a returns to level 4a in one Rabi oscillation time by re-emitting photon energy coherently.

We present another QCL structure that will produce light at ~ 8 μm in

Fig. 6.1(b). In the gain period, the electrons are injected into level 3g and the radiative transition takes place between levels 3g and 2g. Levels 3g and 2g have a transition energy of 150 meV and a dipole moment, μ_g/e, of 1.55 nm. Level 3g has a lifetime of ~ 3 ps, while level 2g has a lifetime of ~ 0.5 ps. The absorbing periods of this structure have four levels. The radiative transition takes place between levels 3a and 4a and levels 3a and 4a are in resonance with levels 3g and 2g of the gain periods. In the absorbing periods, electrons are injected into level 3a, and level 4a is empty when there is no radiative scattering from level 3a. With the application of bias that brings the injector ground levels in the injectors preceding both the gain and absorbing periods close to levels 3g and 3a of gain and absorbing periods, respectively, the gain periods have a high population inversion due to a very long lifetime of level 3g compared to the lifetime of level 2g and the absorbing periods will have approximately a population inversion of ~ -1 as electrons are injected into level 3a, and level 4a can be considered empty at steady-state.

Strictly speaking, there is not a single gain recovery time T_1 for the gain or absorbing periods. The gain recovery time is defined for a two-level system and it is assumed that both levels relax at the same rate after they are perturbed, so that there is only one time constant. Figure 6.1 shows that both gain and absorbing periods have a complicated level structure; the levels all have different relaxation times. Moreover, the two resonant levels will not relax at the same rate after being perturbed. Despite this complexity, however, detailed calculations of the relaxation times of the different levels in the structure, as described in Chapter 5, show that all the relaxation times are on the order of ~ 1 ps.

6.4 Ratio of Gain to Absorbing Periods

We have implemented the carrier transport model and the coherence time model developed in chapter 5 to the structure that emits light at ~ 8 μm. From the calculated values of the carrier densities in the resonant levels and the coherenece times between the resonant levels of the gain and absorbing periods, we have calculated the ratio of the gain per unit length that is produced by one gain period to the absorption per unit length that is produced by one absorbing period. Using this result, we may calculate the ratio of the number of gain to absorbing periods R_{ga} that corresponds to a given ratio of gain to absorption per unit length. Once that is determined, we may find the limits on the ratio of gain to absorbing periods that will lead to stable structures for SIT modelocking.

From the equations for g and a given in Chapter 3, the ratio of gain to absorption is given by

$$\frac{g}{a} = \frac{N_g \Gamma_g \mu_g^2 T_{2g}}{N_a \Gamma_a \mu_a^2 T_{2a}}. \tag{6.1}$$

In Eq. (6.1), N_g and N_a are the total carrier densities in the gain and absorbing periods, respectively. To calculate the ratio of the gain from one gain period g' to absorption from one absorbing period a', we have to replace N_g and N_a by N'_g and N'_a, respectively, where N'_g is the carrier density in one gain period, i.e., a summation of the carrier densities in two gain resonant levels, and N'_a is the carrier density in one absorption period, i.e. a summation of the carrier densities in two absorbing resonant levels. We can assume that the optical mode overlap factor for the gain and absorbing periods are approximately equal, i.e., $\Gamma_g \approx \Gamma_a$. Therefore, we may write

$$\frac{g'}{a'} = \frac{N'_g \mu_g^2 T_{2g}}{N'_a \mu_a^2 T_{2a}}. \tag{6.2}$$

After calculating the values of the quantities in Eq. (6.2) using the models developed in Chapter 4 and in Chapter 5, we find that for the ~ 8 μm QCL, $g'/a' \approx 4.9$. The operating point of the QCL, and hence its stability, depends on g/a, which may be varied by changing the ratio of the number of gain periods to the number of absorbing periods R_{ga}. In Fig. 6.2, we plot the stability curves for the ~ 8 μm QCL and different lines within the stable operating limits that correspond to different choices of R_{ga}.

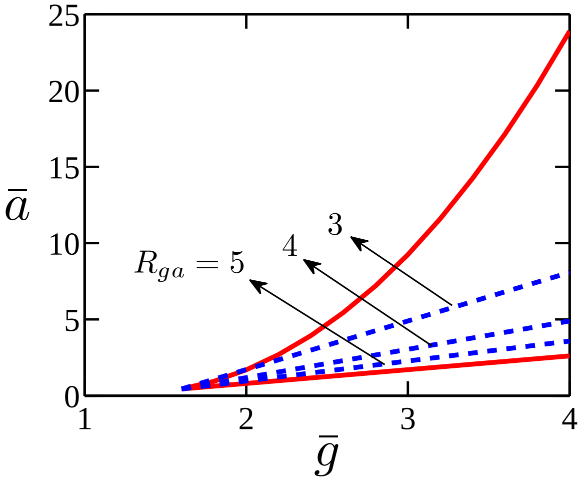

Figure 6.2: Stability limits of $\bar{g}$ vs. $\bar{a}$ for the $\sim$ 8 μm QCL. If the laser is operated with $\bar{a}$ above the upper red solid curve, the pulse damps, and if the laser is operated with $\bar{a}$ below the lower red solid curve, continuous waves grow. The blue dashed lines show the operating lines of the QCL with different gain to absorbing period ratios.

6.5 Conclusion

In this chapter, we describe QCL structures that satisfy the condition to achieve SIT modelocking. Absorbing periods are different from gain periods. Achieving the required population inversion in the absorbing periods is simple, but minimizing excited loss from the upper resonant level is challenging. The gain and absorption obtained from the gain and absorbing periods depend on the design, input current, and the ratio of the number of gain and absorbing periods. Once the basic period is designed, appropriate numbers of gain and absorbing periods can be determined by using the theory of Chapter 5.

Chapter 7

Backward-Propagating Waves and Lumped Mirror Losses

7.1 Introduction

Up to this point, we have used the Maxwell-Bloch equations, applied to a simple two-level system [122, 123], to model the light propagation in both the gain and absorbing periods, ignoring all spatial inhomogeneity. In particular, the large lumped mirror losses were averaged over the propagation and no backward-propagating waves were considered. We only considered the waves that propagate in a single direction as shown in Fig. 7.1(a). A uni-directional propagation model for the evolution of modelocked pulses is a standard approach in the literature and has been extensively used [27]. However, when continuous waves experience gain, the forward- and backward-propagating waves can interfere nonlinearly and produce standing waves, due to the small values of gain recovery time T_1. As a result, Wang *et al.* [28] and Gordon *et al.* [29] observed spatial hole burning in conventional QCLs with an input current set above threshold.

In this chapter, we will discuss a model for SIT modelocking of a QCL in which the waves propagate in both directions and the mirror losses are not averaged over

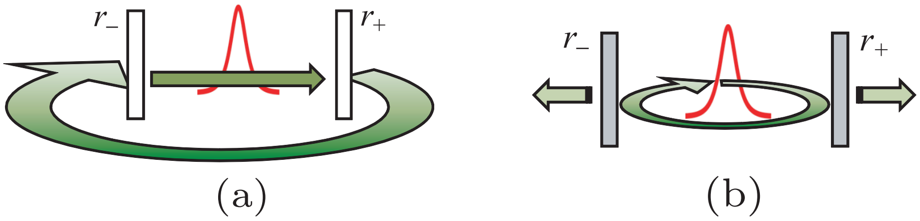

FIGURE 7.1: Schematic illustration of (a) Uni-directional propagation and (b) Bi-directional propagation.

the cavity length, but instead are lumped at the edges as shown in Fig. 7.1(b). We will show that backward-propagating waves do not affect the stability of SIT modelocking. However, SIT modelocking is only stable when backward-going continuous waves are suppressed and hence cannot interact with forward-going waves. By contrast, the lumped losses at the mirrors do affect the stability due to the incomplete gain recovery that the pulses experience after reflecting from the mirrors, coincident with their loss of energy at the mirrors.

7.2 Theoretical Models

When the electric field propagates in only one direction, so that there is no interference, and we ignore spatial inhomogeneity, the dynamics in a QCL having absorbing periods in addition to gain periods can be described by the Maxwell-Bloch equations in the two-level approximation [119],

$$\frac{n}{c}\frac{\partial E}{\partial t} + \frac{\partial E}{\partial z} = -i\sum_{x=a,g}\frac{kN_x\Gamma_x\mu_x}{2\epsilon_0 n^2}\eta_x - \frac{1}{2}l_u E, \tag{7.1a}$$

$$\frac{\partial \eta_{g,a}}{\partial t} = \frac{i\mu_{g,a}}{2\hbar}\Delta_{g,a}E - \frac{\eta_{g,a}}{T_{2g,a}}, \tag{7.1b}$$

$$\frac{\partial \Delta_{g,a}}{\partial t} = \frac{i\mu_{g,a}}{\hbar}\eta_{g,a}E^* - \frac{i\mu_{g,a}}{\hbar}\eta^*_{g,a}E + \frac{\Delta_{g,a0}-\Delta_{g,a}}{T_{1g,a}}, \tag{7.1c}$$

where the subscripts g and a refer to quantities in the gain and absorbing periods, respectively. The independent variables z and t are length along the light-propagation axis of the QCL and time. The dependent variables E, η and Δ denote the envelopes of the electric field, gain polarization, and gain inversion. The parameters $\Delta_{g0} \simeq 1.0$ and $\Delta_{a0} \simeq -1.0$ denote the equilibrium inversion away from the modelocked pulse. The parameters n and c denote the index of refraction and the speed of light. The parameters N and Γ denote the effective electron density and the optical mode overlap factor with the active region of the laser structure. The parameters k, ϵ_0, and $\hbar$ denote the wavenumber, the vacuum dielectric permittivity, and Planck's constant. The parameter l_u denotes the average linear loss including mirror loss.

If we take into account counter-propagating waves and lumped mirror losses, then the dynamics of a QCL that has both gain and absorbing periods can be described by

$$\begin{align}
\frac{n}{c}\frac{\partial E_\pm}{\partial t} + \frac{\partial E_\pm}{\partial z} &= -i \sum_{x=a,g} \frac{kN_{g,a}\Gamma_{g,a}\mu_{g,a}}{2\epsilon_0 n^2}\eta_{g,a\pm} - \frac{1}{2} l_b E_\pm, \tag{7.2a}\\
\frac{\partial \eta_{g,a\pm}}{\partial t} &= i\frac{\mu_{g,a}}{2\hbar}(\Delta_{g,a}E_\pm + \Delta^\pm_{2g,a}E_\mp) - \frac{\eta_{g,a\pm}}{T_{2g,a}}, \tag{7.2b}\\
\frac{\partial \Delta_{g,a}}{\partial t} &= i\frac{\mu_{g,a}}{\hbar}(\eta_{g,a+}E^*_+ + \eta_{g,a-}E^*_- + \text{c.c.}) + \frac{\Delta_{g,a0} - \Delta_{g,a}}{T_{1g,a}}, \tag{7.2c}\\
\frac{\partial \Delta^\pm_{2g,a}}{\partial t} &= \pm\, i\frac{\mu_{g,a}}{\hbar}(E^*_+\eta_- - \eta^*_+ E_-) - \frac{\Delta^\pm_{2g,a}}{T_{1g,a}}, \tag{7.2d}
\end{align}$$

where the variables, constants, and subscripts are the same as in the Eqs. (7.1a)–(7.1c) for uni-directional propagation except that $\Delta_{2g,a}$ refers to the inversion grating. The quantities with + (−) subscripts represent waves traveling in the positive (negative) z-direction. The linear loss l_b in Eq. (7.2a) only includes the loss in the medium. Mirror losses are taken into account by the boundary conditions. QCLs have cleaved facets, and the reflection coefficients at the edges depend on the refractive index difference between the laser medium and air, i.e., $r_- = r_+ = (n-1)/(n+1)$, where r_- and r_+ are the reflection coefficients at the two interfaces. The notation closely follows that of Wang *et al.* [28] and Gordon *et al.* [29], with the difference that we have an absorbing as well as a gain medium.

Actually, in Eq. (7.2d), the recovery time T_1 should be replaced by the grating lifetime T_G which is defined by [29]

$$\frac{1}{T_G} = \frac{1}{T_1} + 4k^2 D. \tag{7.3}$$

The parameter T_G determines the strength of spatial hole burning. The parameter T_G can therefore range from zero when there is no spatial hole burning to T_1 when spatial hole burning is strongest. The diffusion coefficient D can be estimated from the Einstein relation $D = \mu k_B T/q$, where μ is the electron mobility, k_B is the Boltzmann's constant, T is the temperature, and q is the electron charge. Even using an upper value for the electron mobility of 7000 (cm^2/s)/V and $k = 2.25 \times 10^4$ cm^{-1}, which corresponds to a vacuum wavelength of 8.38 μm, $4k^2D \approx$ 0.09 THz at 77 K and $4k^2D \approx$ 0.4 THz at 300 K, both significantly smaller than $T_1^{-1} \approx$ 0.6 THz at 77 K and $T_1^{-1} \approx$ 2 THz at 300 K. Thus the contribution of carrier diffusion in Eq. (7.3) is insignificant. Hence, it can be assumed that $T_G \approx T_1$. Due to the fast gain recovery in QCLs, carrier diffusion does not eliminate spatial hole burning, in contrast to what occurs in diode lasers [173, 174].

As has been discussed in Chapter 3, the gain per unit length (g) from the gain periods of the QCL and the absorption per unit length (a) from the absorbing periods are given by

$$g = \frac{kN_g\Gamma_g\mu_g^2T_{2g}}{2\epsilon_0 n^2\hbar}, \quad a = \frac{kN_a\Gamma_a\mu_a^2T_{2a}}{2\epsilon_0 n^2\hbar}. \tag{7.4}$$

We present the results in terms of normalized gain ($\bar{g}$) and absorption ($\bar{a}$) coefficients. Gain and absorption coefficients are normalized by average loss per unit length, which is l_u when we solve Eq. (7.1) and is $l_b - \ln r_-/L - \ln r_+/L$ when we solve Eq. (7.2). Here, we use L to denote the cavity length.

7.3 Simulation Results

We have presented an extensive computational analysis of SIT modelocking using Eq. (7.1) in Chapter 3. Here, we analyze SIT modelocking by computationally solving Eq. (7.2) and comparing the results to those of Chapter 3. We assume that a resonant pulse of hyperbolic-secant shape and a π pulse in the gain medium is injected into the QCL structure from an external source. We note that since continuous waves must be suppressed, this laser will not self-start. Our computational results show that stable modelocked solutions exist when we consider backward-propagating waves and lumped mirror losses at the edges. An initially broad pulse becomes narrower and evolves toward a fixed intensity profile after each round trip. We show the pulse evolution in a 3-mm-long QCL cavity in Fig. 7.2. In this example, we set $\bar{g} = 3.5$ and $\bar{a} = 2.8$. An initial pulse of 100 fs duration (FWHM/1.763) narrows down to ~ 65 fs. The pulse narrowing when we solve Eq. (7.2) is less than when we solve Eq. (7.1). With the same parameters and initial conditions as in Fig. 7.2, the stable pulse duration is only ~ 43.5 fs, when solving Eq. (7.1).

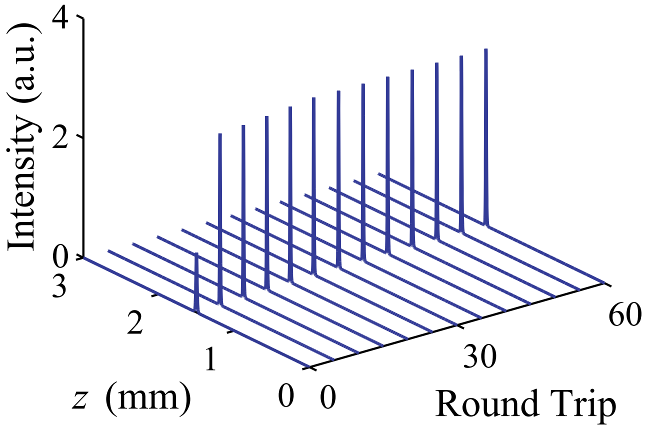

FIGURE 7.2: Modelocked pulse evolution when backward-propagating waves and lumped mirror losses are considered. We set $T_{1g} = T_{1a} \equiv T_1$, $T_{2g} = T_{2a} \equiv T_2$, and $T_1/T_2 = 10$ with $T_2 = 100$ fs.

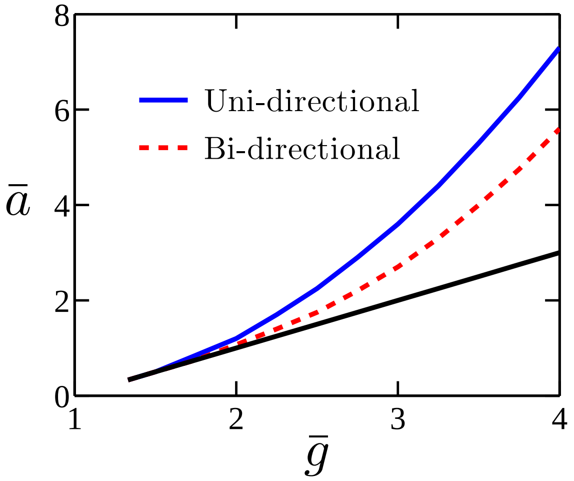

FIGURE 7.3: Stability limits of normalized gain ($\bar{g}$) versus normalized absorption ($\bar{a}$) coefficients. We set $T_{1g} = T_{1a} \equiv T_1$, $T_{2g} = T_{2a} \equiv T_2$, and $T_1/T_2 = 10$ with $T_2 = 100$ fs. The upper curves are the upper limiting values of $\bar{a}$. The bottom black line is the limiting values for continuous wave (cw) growth in both cases.

Figure 7.3 compares the stability limits of $\bar{g}$ and $\bar{a}$ for SIT modelocking when we solve Eq. (7.1) and when we solve Eq. (7.2). The bottom black solid line shows the lower stability limit in both cases. This boundary is set by the growth of continuous waves. If the lasers are operated with parameters set below this boundary, continuous waves are unstable, and multiple pulses may form due to the Risken-Nummedal-Graham-Haken effect [33, 34]. The upper lines show the upper stability limits of $\bar{a}$ and are set by the losses. If the laser is operated with parameters set above these lines, pulses damp. The upper limiting values of $\bar{a}$ are smaller when we solve Eq. (7.2) than when we solve Eq. (7.1) due to the lumped mirror losses and the delay in the gain recovery when pulses reflect from the mirrors. Pulses lose a significant amount of energy ($\sim$50%) at the QCL mirrors before bouncing back for another passage through the laser. Ideally, the absorption should decrease and the gain should increase in order for the pulse to grow to a sustainable intensity. However, just the opposite occurs. When the pulses bounce back from the cavity edges, the inversion $\Delta_{g,a}$ will not have regained its equilibrium value before the pulse passes through again. When QCLs operate below the lower stability limit in $\bar{a}$, continuous waves are unstable, so that multiple pulses are created and interfere each other, and we observe spatial hole burning in some parameter regimes. However, if QCLs operate with $\bar{a}$ above the lower stability limit, continuous wave growth is suppressed by the absorbing layers, and no spatial hole burning is observed.

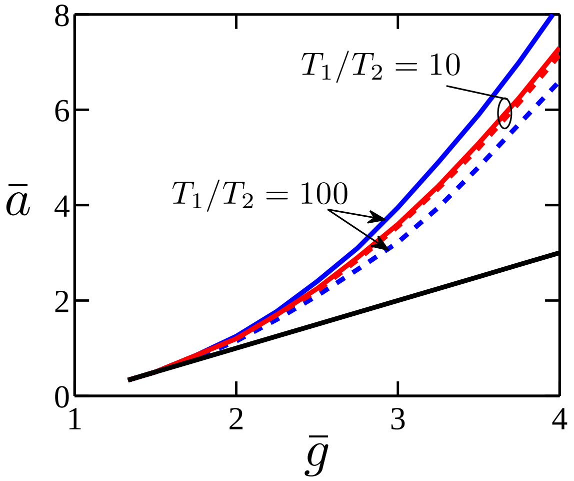

FIGURE 7.4: Stability limits for different T_1/T_2 values with $r_- = 1$ and $r_+ = 1$. Solid lines show solutions of Eq. (1), while dashed lines show solutions of Eq. (2).

In Fig. 7.4, we show the effect of the gain recovery time on the upper stability limit in $\bar{a}$. We set $r_- = r_+ = 1$ so that we can observe the change in stability that is due only to the delay in the gain recovery. We assume $T_{1g} = T_{1a} \equiv T_1$ and $T_{2g} = T_{2a} \equiv T_2$. As expected, the upper limit for $\bar{a}$ is lower when we solve Eq. (7.2), than it is when we solve Eq. (7.1), even though there are no mirror losses. When we solve Eq. (7.1), the upper stability limit in $\bar{a}$ increases, whereas it decreases when we solve Eq. (7.2). However, when $T_1/T_2 = 10$ with $T_2 = 100$ fs, the gain recovery time T_1 is only 1 ps, which is a typical value obtained in QCLs, and is very short compared to the cavity round-trip time of ~ 50 ps. Therefore, the population inversion can recover its equilibrium value before the pulse passes through after reflecting from the mirrors, except in a small region near the edges of the QCL. The instantaneous population inversions for both the gain and absorbing media are drawn in Fig. 7.5 at different points in the cavity when the pulse bounces back from the right edge. Figure 7.5 shows that when T_1/T_2 become large, i.e.,

$T_1/T_2 = 100$ with $T_2 = 100$ fs, the population inversion at the left edge has not recovered even when the pulse reaches the right edge.

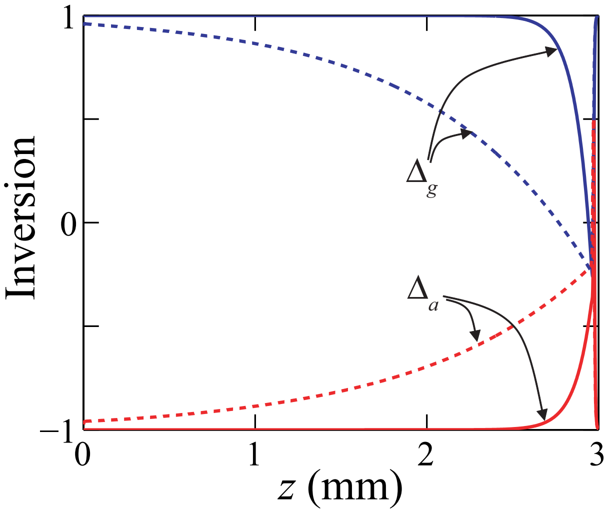

FIGURE 7.5: Population inversion in the cavity. The solid lines are for $T_1/T_2 = 10$ and the dashed lines are for $T_1/T_2 = 100$.

7.4 Conclusion

In this chapter, we have shown that SIT modelocking is stable in QCLs when we take into account realistic, lumped mirror losses and backward-propagating waves. However, the stable parameter regime is reduced. Incomplete gain recovery at the QCL edges when the pulses pass through after reflecting from the mirrors, along with mirror losses, is largely responsible for this reduction. Since continuous waves are suppressed in the stable operating regime, spatial hole burning does not appear in this regime. It does appear when $\bar{a}$ is below the stable operating limit.

Chapter 8

Saturable Nonlinearity and Chromatic Dispersion

8.1 Introduction

Paiella *et al.* [35] observed self-focusing due to a strong intensity-dependent refractive index in QCLs. In addition, Wang *et al.* [28] and Gordon *et al.* [29] found evidence for an intensity-dependent loss in QCLs. They found that the loss saturates when QCLs are operated with an input current that is above threshold. As the intensity of the light inside the laser increases, the intensity-dependent portion of the refractive index, n_2, adds to the intensity-independent portion of the refractive index, n_0. The total refractive index of the core increases. Therefore, the overlap of the lateral optical mode with the core increases, and the overlap with the lossy cladding decreases, as schematically shown in Fig. 8.1(a). As a result, the loss decreases. In practice, the change of the refractive index with intensity can be positive or negative, depending on the wavelength. When the sign of n_2 is negative, then the loss will increase because the overlap of the lateral optical mode with the lossy cladding will increase, as schematically shown in Fig. 8.1(b). Therefore, an optical pulse may experience saturable loss or saturable gain, depending on the wavelength of the laser transition.

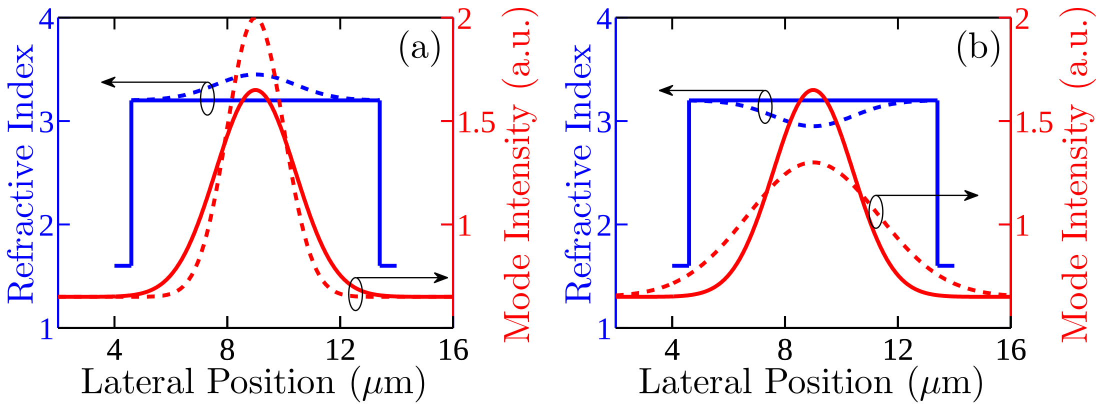

Figure 8.1: Refractive index profile and resulting intensity distribution of the fundamental waveguide mode along the lateral direction of a conventional QCL waveguide in case of (a) saturable loss and (b) saturable gain. The intensity profile changes due to the strong index nonlinearity of the active region. (a) If the intensity increases, the index near the center of the waveguide increases and the mode is more tightly confined. (b) If the intensity decreases, the index near the center of the waveguide decreases and the mode is more weakly confined.

Chromatic dispersion is also present in QCLs. Choi *et al.* [175] found for a particular QCL a dispersion coefficient $\beta_2 \sim -4.6$ ps^2/m at the 5 μm gain transition. Therefore, a pulse may broaden during propagation inside the laser structure.

In the work on SIT modelocking of QCLs that we have discussed so far, we have not considered the effects of saturable nonlinearity and chromatic dispersion. The intensity dependence of the refractive index when the pulse propagates in the laser structure has been neglected, and therefore, the loss has always been independent of the intensity in the analysis. Since the stability of the SIT modelocking depends on the values of the gain and absorption coefficients relative to loss, the modulation of loss by the intensity will affect the stability of the SIT modelocking. Since SIT modelocking generates, in principle, pulses on the order of only 100 fs, chromatic dispersion, which spreads the pulses will also affect the stability. Therefore, it is essential to investigate the effects of saturable nonlinearity and chromatic dispersion in order to determine the practicality of SIT modelocking.

In this chapter, we find that SIT modelocking is achieved in the presence of the saturable loss or the saturable gain, but only when the saturable loss and the saturable gain are below critical values. The limiting values of the saturable loss are significantly lower in magnitude than the limiting values of the saturable gain. The intensity and duration of the modelocked pulse depend on the amount of the saturable loss or saturable gain, in addition to the gain and absorption coefficients.

SIT modelocking is stable when the chromatic dispersion is normal or anomalous, in contrast to conventional passively modelocked systems that can be modeled by the complex Ginzburg-Landau equation [27]. In fact, as we will show, the pulse intensity as a function of time is the same regardless of the sign of the chromatic dispersion in SIT modelocking. The pulse intensity decreases and the pulse duration increases when the absolute value of the dispersion coefficient increases. Beyond a critical value that depends on the magnitude of the gain and absorption coefficients, the pulses become unstable. They either break up into multiple pulses due to the growth of continuous waves, or they damp away.

When saturable nonlinearity and chromatic dispersion are simultaneously present, as would be expected to occur in practice, the stability limit for the saturable loss increases, becoming less stringent, while the stability limit for the saturable gain remains almost unchanged. We will show that realistic values for the saturable nonlinearity and chromatic dispersion are within the range where SIT modelocked pulses are expected to be stable.

The remainder of this chapter is organized as follows: Sec. 8.2 discusses the theoretical model of the pulse dynamics in QCLs that have interleaved gain and absorbing periods, when the saturable nonlinearity and chromatic dispersion are present in the laser medium. In Sec. 8.3, we show the effects of the saturable loss or the saturable gain on SIT modelocking. In Sec. 8.4, we show the effects of the chromatic dispersion on SIT modelocking. In Sec. 8.5, we show the effects on the SIT modelocking when both the nonlinearity and chromatic dispersion are present. Finally, in Sec. 8.6, we summarize the results and draw conclusions.

8.2 Theoretical Model

In the presence of saturable nonlinearity and chromatic dispersion, the Maxwell-Bloch equations presented in Chapter 3 that describe the gain dynamics of a QCL having both the gain and absorbing periods change to

$$\frac{n}{c}\frac{\partial E}{\partial t} = -\frac{\partial E}{\partial z} - i\frac{kN_g\Gamma_g\mu_g}{2\epsilon_0 n^2}\eta_g - i\frac{kN_a\Gamma_a\mu_a}{2\epsilon_0 n^2}\eta_a - \frac{1}{2}l(|E|^2)E - i\frac{1}{2}\beta_2\frac{\partial^2 E}{\partial t^2}, \tag{8.1a}$$

$$\frac{\partial \eta_g}{\partial t} = \frac{i\mu_g}{2\hbar}\Delta_g E - \frac{\eta_g}{T_{2g}}, \tag{8.1b}$$

$$\frac{\partial \Delta_g}{\partial t} = \frac{i\mu_g}{\hbar}\eta_g E^* - \frac{i\mu_g}{\hbar}\eta_g^* E + \frac{\Delta_{g0} - \Delta_g}{T_{1g}}, \tag{8.1c}$$

$$\frac{\partial \eta_a}{\partial t} = \frac{i\mu_a}{2\hbar}\Delta_a E - \frac{\eta_a}{T_{2a}}, \tag{8.1d}$$

$$\frac{\partial \Delta_a}{\partial t} = \frac{i\mu_a}{\hbar}\eta_a E^* - \frac{i\mu_a}{\hbar}\eta_a^* E + \frac{\Delta_{a0} - \Delta_a}{T_{1a}}, \tag{8.1e}$$

where the subscripts g and a in Eq. (1) refer to the gain and absorbing periods, respectively. The independent variables z and t denote length along the light-propagation axis of the QCL and time. The dependent variables E, η_g, Δ_g, η_a, and Δ_a denote the envelope of the electric field, the polarization and inversion in the gain medium, and the polarization and inversion in the absorbing medium. The parameters Δ_{g0} and Δ_{a0} denote the equilibrium inversion away from the modelocked pulse. The parameters μ_g and μ_a denote the dipole moments. The parameters N and Γ denote the electron density and the mode overlap factor. The parameters n, c, k, ϵ_0, and $\hbar$ denote the index of refraction, the speed of light, the wavenumber in the active region, the vacuum dielectric permittivity, and Planck's constant. The parameter β_2 is the dispersion coefficient. The parameter $l(|E|^2)$ denotes the loss that depends on the light intensity.

The Maxwell-Bloch equations (8.1) are the same as the Maxwell-Bloch equations given in Chapter 3 except that in Eq. (8.1a), we include the effect of chromatic dispersion, and we allow l to depend on the field intensity. We may write the intensity dependent loss as

$$l(|E|^2) = l_0 - \gamma |E|^2, \tag{8.2}$$

where l_0 is the linear loss and γ is the saturable nonlinearity coefficient. According to Eq. 8.2, the loss will saturate when $\gamma > 0$ and the gain will saturate when $\gamma < 0$. The sign of γ depends directly on the sign of n_2, which in turn depends on the wavelength of the laser transition [123]. Gordon *et al.* [29] found that γ depends sensitively on the width of the QCL active region. As the width of the active region increases, the parameter γ decreases. Gordon *et al.* found that γ decreases approximately by a factor of two when the width of the active region increases from 3 μm to 7.5 μm.

In this work, we have set $T_{2g} = T_{2a} = 100$ fs and $T_{1g} = T_{1a} = 1$ ps. We have set $l_0 = 10$ cm^{-1} and $L_c = 3$ mm. All these values are realistic [29]. We set $\mu_g/e = 1.8$ nm, which corresponds to the design value that we presented in Chapter 6. We also assume that the gain periods are completely inverted in equilibrium, i.e., $\Delta_{g0} = 1$, while the absorbing periods are completely uninverted in equilibrium, i.e., $\Delta_{a0} = -1$. The absorbing periods have a dipole moment twice as large as the dipole moment in the gain periods, i.e., $\mu_a/\mu_g = 2$.

We will consider initial pulses that are hyperbolic-secant shaped, so that $E(t) = E_0 \,\mathrm{sech}(t/\tau)$, where $\tau = 50$ fs, and we choose E_0 so that the initial pulse is a π pulse in the gain periods and a 2π pulse in the absorbing periods. We note that when $\tau = 50$ fs, the full width half maximum (FWHM) duration is given by $[2\ln(1+\sqrt{2})]\tau \approx 1.763\tau \approx 88$ fs. We recall that the condition to be a π pulse in the gain medium is $(\mu_g/\hbar)\int_{-\infty}^{\infty} E(t)\,dt = \pi$, so that $E_0 = 7.3 \times 10^6$ V/m.

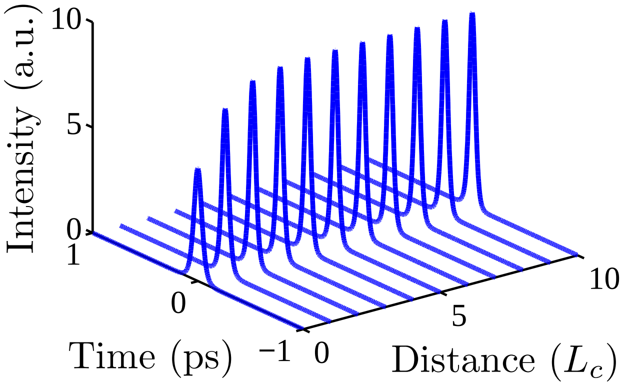

FIGURE 8.2: Modelocked pulse evolution in presence of saturable loss. The saturable nonlinearity coefficient $\gamma = 10^{-12}$ m/V^2. We set $\bar{g} = 4$ and $\bar{a} = 5$. The dispersion coefficient (β_2) is set to zero.

8.3 Nonlinearity

In this section, we study the case when only saturable loss or saturable gain is present in the medium by setting $\beta_2 = 0$ in Eq. (8.1a).

Saturable Loss ($\gamma > 0$)

The saturable nonlinearity coefficient γ is positive when the refractive index increases with intensity. Therefore, with $\gamma > 0$, the lateral optical mode becomes better confined in the core, and the loss saturates as the intensity of the pulse grows, as shown schematically in Fig. 8.1(a). We have found that stable modelocked pulses are obtained when $\gamma < \gamma_c$, where γ_c is the critical value of the coefficient γ. In Fig. 8.2, we show an example of the evolution of an initial hyperbolic-secant pulse whose initial energy corresponds to a π pulse in the gain periods. Here, we have set $\gamma = 10^{-12}$ m/V^2. The gain normalized to the linear loss and the absorption normalized to the linear loss are set to 4 and 5, respectively. The pulse reaches its stable equilibrium after propagating a distance that is only a few times the cavity length (L_c). The intensity of the initial pulse grows,

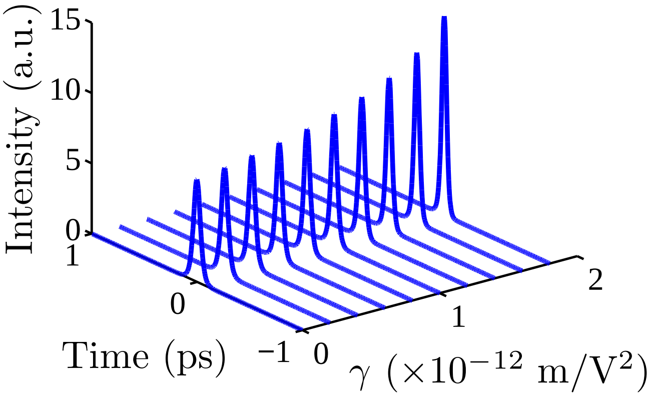

FIGURE 8.3: Equilibrium modelocked pulse shapes vs. the saturable nonlinearity coefficient (γ). In each case, the pulse is shown after it has propagated a distance of $1000L_c$. We set $\bar{g} = 4$ and $\bar{a} = 5$. The dispersion coefficient (β_2) is set to zero.

and the duration of the initial pulse narrows before the pulse equilibrates. In an SIT-modelocked laser, the pulse intensity and the pulse duration are determined by the values of the gain and absorption coefficients relative to the loss [119, 120]. However, in the presence of a saturable loss, pulses are further shaped by the intensity-dependent loss in addition to the gain and absorption coefficients. A saturable loss favors more intense, shorter pulses. The additional pulse shaping depends on the magnitude of γ. In Fig. 8.3, we show the stable modelocked pulses with different values of γ. The maximum intensity of the pulse increases and the duration of the pulse decreases as γ increases. However, the laser becomes unstable when $\gamma > 1.9 \times 10^{-12}$ m/V^2 with $\bar{g} = 4$ and $\bar{a} = 5$.

In Fig. 8.4, we show the change in the normalized maximum intensity and in the duration of the stable modelocked pulses when γ changes. We define the duration as the full width at half maximum (FWHM) divided by $2\ln(1+\sqrt{2}) = 1.763$. The maximum intensity of the pulses has been normalized by the maximum intensity of the pulse with $\gamma = 0$. The maximum intensity and the pulse durations have been calculated after the pulses have propagated a distance of $1000L_c$. In each case, the pulse becomes stable after propagating a distance of less than $100L_c$. We find that the maximum intensity of the pulse increases as γ increases. The maximum intensity of the pulse is larger by more than a factor of two when $\gamma = 1.9\times10^{-12}$ m/V^2 than it is when $\gamma = 0$. However, beyond this nonlinearity, i.e., $\gamma > 1.9 \times 10^{-12}$ m/V^2, the pulse becomes unstable. The pulse duration decreases as γ increases. We see that the stable pulse has a duration of $\sim$ 43 fs when $\gamma = 0$, while the stable pulse has a duration of $\sim$ 28 fs when $\gamma = 1.9 \times 10^{-12}$ m/V^2.

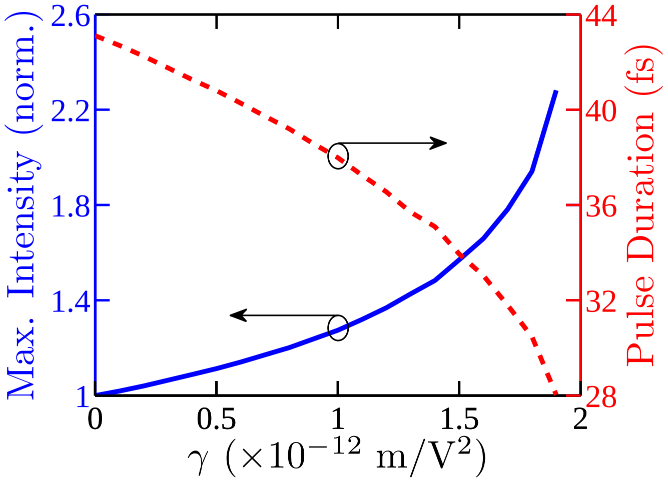

FIGURE 8.4: The normalized maximum intensity and pulse duration (FWHM/1.763) of the stable modelocked pulse vs. the saturable nonlinearity coefficient (γ). We set $\bar{g} = 4$ and $\bar{a} = 5$. The dispersion coefficient (β_2) is set to zero.

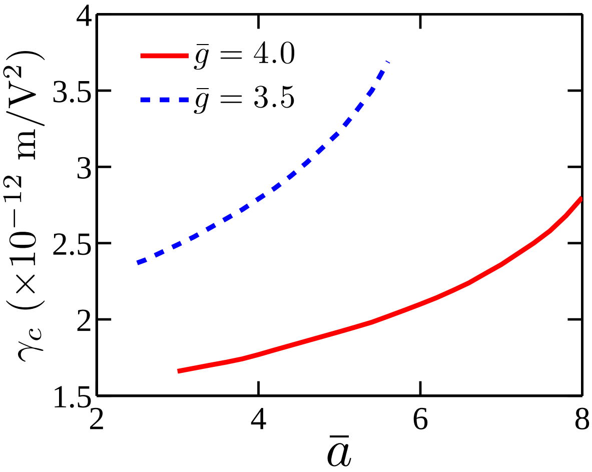

FIGURE 8.5: The critical values of the saturable nonlinearity coefficient (γ_c) vs. the normalized absorption coefficient ($\bar{a}$) for two values of the normalized gain coefficient ($\bar{g}$). The dispersion coefficient (β_2) is set to zero.

The critical value of γ, $\gamma = \gamma_c$, at which there is no stable pulse depends on the normalized gain and absorption coefficients. In Fig. 8.5, we present γ_c vs. $\bar{a}$ for two values of $\bar{g}$. We find that the values of γ_c vary significantly when $\bar{a}$ and $\bar{g}$ change. As $\bar{a}$ increases or $\bar{g}$ decreases, we find that γ_c increases. By increasing $\bar{a}$ and decreasing $\bar{g}$, the critical value of the saturable loss for stable operation can be significantly increased.

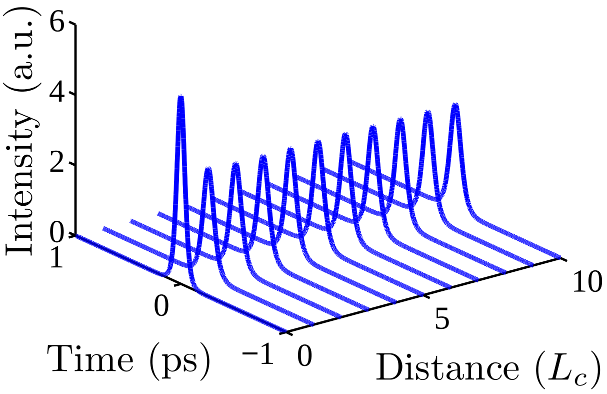

FIGURE 8.6: Modelocked pulse evolution in the presence of saturable gain. The saturable nonlinearity coefficient $\gamma = -10 \times 10^{-12}$ m/V^2. We set $\bar{g} = 4$ and $\bar{a} = 5$. The dispersion coefficient (β_2) is set to zero.

Saturable Gain ($\gamma < 0$)

The saturable nonlinearity coefficient γ becomes negative when the refractive index of the core decreases as the light intensity increases. In this case, the overlap of the lateral mode with the core decreases, while the overlap with the lossy cladding increases as in Fig. 8.1(b). As a result, the gain will saturate as the light intensity increases. We show an example of the evolution of a stable modelocked pulse in Fig. 8.6 when saturable gain is present. As before, we choose an initial π pulse. In this case, the nonlinear coefficient γ is set to -10×10^{-12} m/V, and we use $\bar{g} = 4$ and $\bar{a} = 5$. We note that the intensity of the initial pulse decreases and the duration of the initial pulse increases before the pulse equilibrates. Similar to the case when the saturable loss is present, the pulse intensity and the pulse duration are determined by the saturable gain, in addition to the gain and absorption coefficients. In Fig. 8.7, we plot the stable modelocked pulses with different amounts of saturable gain. In each case, the pulse is shown after it has propagated a distance of $1000L_c$. Stable modelocked pulses become less intense and broader as γ becomes more negative. The pulses no longer equilibrate, but instead damp away when $\gamma \lesssim -68 \times 10^{-12}$ m/V^2.

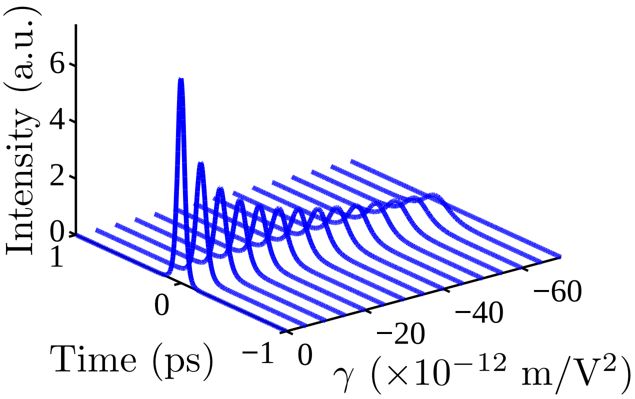

FIGURE 8.7: Equilibrium modelocked pulse shapes vs. the saturable nonlinearity coefficient (γ). In each case, the pulse is shown after it has propagated a distance of $1000L_c$. We set $\bar{g} = 4$ and $\bar{a} = 5$. The dispersion coefficient (β_2) is set to zero.

In Fig. 8.8, we show the change in the normalized maximum intensity and in the duration (FWHM/1.763) of the stable modelocked pulses as $|\gamma|$ increases. The maximum intensity and the pulse duration values have been calculated after the pulses have propagated a distance of $1000L_c$. In each case, the pulse equilibrates after propagating a distance of less than $100L_c$. We see that the maximum intensity of the pulse at equilibrium decreases as $|\gamma|$ increases, i.e., when γ becomes more negative. The maximum intensity of the pulse is lower by approximately a factor of eight when $\gamma = -68 \times 10^{-12}$ m/V^2 than it is when $\gamma = 0$. When γ becomes more negative, pulses damp away. As $|\gamma|$ increases, the equilibrium pulse duration also increases. The stable pulse duration is 43 fs when $\gamma = 0$, while the stable pulse duration is 155 fs when $\gamma = -68 \times 10^{-12}$ m/V^2. We note that this value is more than 30 times larger in magnitude than the corresponding limit for saturable loss (1.9×10^{-12} m/V^2). Hence the constraint on the saturable gain is far less stringent than the constraint on the saturable loss.

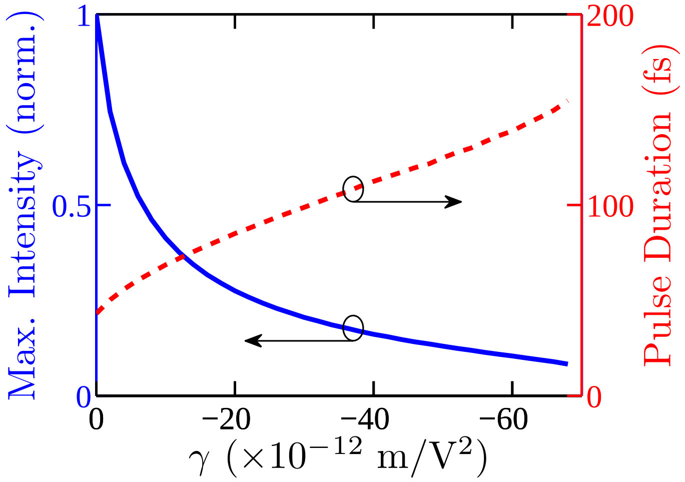

FIGURE 8.8: The normalized equilibrium maximum intensity and pulse duration (FWHM/1.763) of the stable modelocked pulse vs. the saturable nonlinearity coefficient (γ). We set $\bar{g} = 4$ and $\bar{a} = 5$. The dispersion coefficient (β_2) is set to zero.

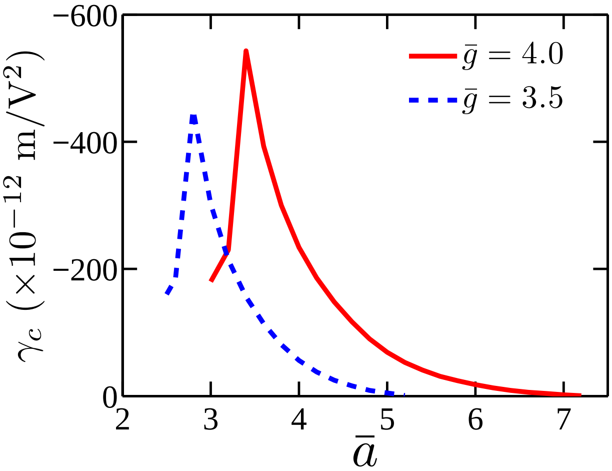

FIGURE 8.9: Critical values of the saturable nonlinearity coefficient (γ_c) vs. the normalized absorption coefficient ($\bar{a}$) for two values of the normalized gain coefficient ($\bar{g}$). The dispersion coefficient (β_2) is set to zero.

In Fig. 8.9, we show the critical values of the saturable nonlinearity coefficient (γ_c) vs. the absorption coefficient ($\bar{a}$) for two values of the gain coefficient ($\bar{g}$) when the pulse experiences saturable gain during propagation. When $|\gamma| > |\gamma_c|$, the initial pulses do not equilibrate. The magnitude of γ_c is sharply peaked, first increasing rapidly as $\bar{a}$ increases and then decreasing. On either side of the peak, $\bar{a}_{\text{peak}}(\bar{g})$, different physical mechanisms destabilize the initial pulse. When $\bar{a} < \bar{a}_{\text{peak}}$ and $|\gamma| > |\gamma_c|$, continuous waves grow and ultimately lead to the generation of multiple pulses. When $\bar{a} > \bar{a}_{\text{peak}}(\bar{g})$ and $|\gamma| > |\gamma_c|$, the initial pulse damps away.

8.4 Chromatic Dispersion

In this section, we study the effects of the chromatic dispersion on SIT modelocking. We assume that the loss is linear and that it does not depend on the intensity of the light pulse, i.e., $\gamma = 0$. In Fig. 8.10, we show the evolution of a stable modelocked pulse in the presence of dispersion where the initial pulse is a π pulse. In this case, the dispersion coefficient $|\beta_2|$ is 5 ps^2/m. We use $\bar{g} = 4$ and $\bar{a} = 5$. We note that the solutions of Eq. (1) when $\beta_2 < 0$ are complex conjugates of the solutions when $\beta_2 > 0$ for equal values of $|\beta_2|$. Hence, the pulse intensity as a function of time is unaffected by the sign of β_2. In Fig. 8.10, we see that the pulse's intensity decreases and its duration increases before the pulse equilibrates, but a modelocked solution exists. Pulse broadening increases as $|\beta_2|$ increases. In Fig. 8.11, we show the stable modelocked pulses in the presence of

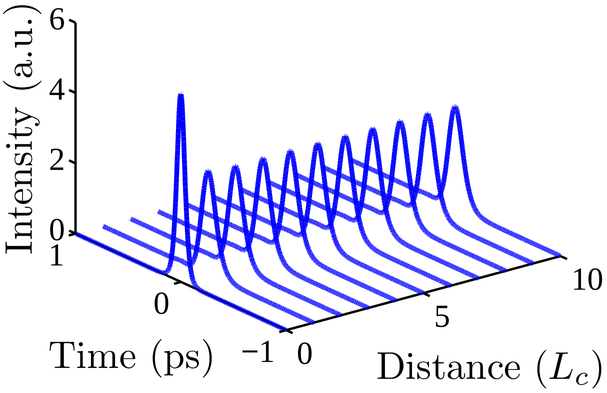

FIGURE 8.10: Modelocked pulse evolution in presence of chromatic dispersion. The dispersion coefficient $|\beta_2| = 5$ ps^2/m. We set $\bar{g} = 4$ and $\bar{a} = 5$. The saturable nonlinearity coefficient (γ) is set to zero.

different amounts of dispersion. In each case, the pulse has propagated a distance of $1000L_c$. We note that the peak intensity of the stable modelocked pulse decreases and the duration increases as $|\beta_2|$ increases. There is no modelocked solution when $|\beta_2| > 82$ ps^2/m. Beyond this critical value of dispersion, the initial pulse damps away.

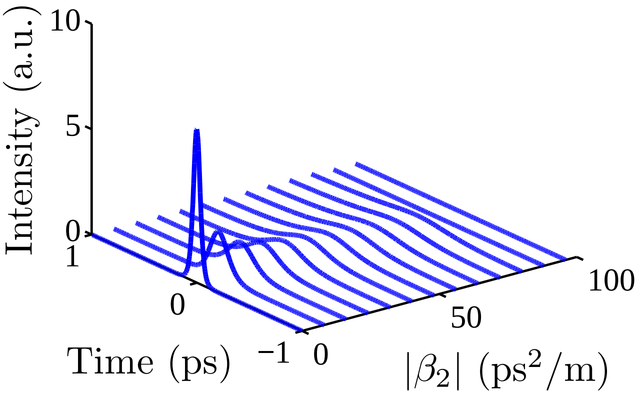

FIGURE 8.11: Equilibrium modelocked pulse shapes vs. chromatic dispersion coefficient ($|\beta_2|$). We set $\bar{g} = 4$ and $\bar{a} = 5$. The saturable nonlinearity coefficient (γ) is set to zero.

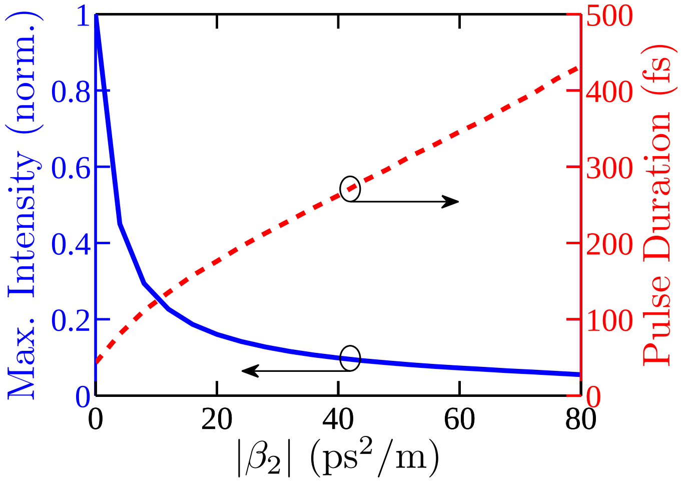

FIGURE 8.12: The normalized maximum intensity and pulse duration (FWHM/1.763) at equilibrium vs. the dispersion coefficient (β_2). We set $\bar{g} = 4$, $\bar{a} = 5$. The saturable nonlinearity coefficient (γ) is set to zero.

In Fig. 8.12, we draw the change in the normalized maximum intensity and in the duration (FWHM/1.763) of the stable pulses as the chromatic dispersion is varied. The maximum intensity has been normalized by the maximum intensity of the pulse with $|\beta_2| = 0$. The maximum intensity and the duration have been calculated after the pulses have propagated a distance of $1000L_c$. In each case, the pulse becomes stable after propagating a distance of less than $100L_c$. We see that the maximum intensity of the pulse decreases as $|\beta_2|$ increases. The maximum intensity of the pulse decreases by approximately a factor of 10 when $|\beta_2| = 80$ ps^2/m compared to when $|\beta_2| = 0$. The equilibrium pulse duration when $|\beta_2| = 0$ is 43 fs, while the equilibrium pulse duration is 432 fs when $|\beta_2| = 80$ ps^2/m.

The critical values of the dispersion coefficients for stable modelocking $|\beta_{2c}|$ have been plotted in Fig. 8.13 vs. $\bar{a}$ for two different values of $\bar{g}$. We see that the critical value first increases as $\bar{a}$ increases up to $\bar{a}_{\text{peak}}(\bar{g})$, and then decreases. The equilibrium pulse duration is always larger when dispersion is present than when it is not. Analogous to the case shown in Fig. 8, we find that when $\bar{a} < \bar{a}_{\text{peak}}(\bar{g})$ and $|\beta_2| > |\beta_{2c}|$, multiple pulses are generated, and when $\bar{a} > \bar{a}_{\text{peak}}(\bar{g})$ and $|\beta_2| > |\beta_{2c}|$, the initial pulse damps away.

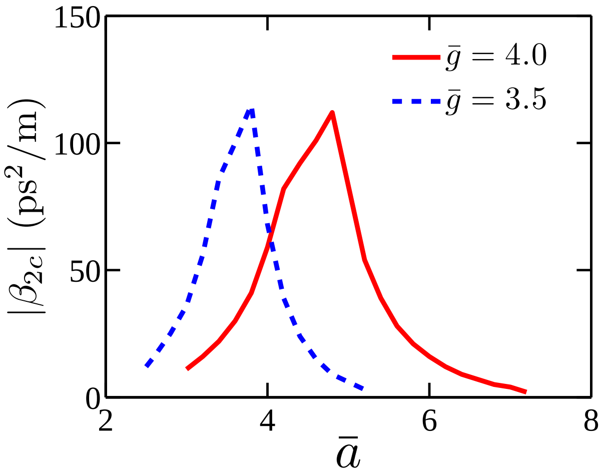

FIGURE 8.13: The critical values of the dispersion coefficient ($|\beta_{2c}|$) vs. the normalized absorption coefficient ($\bar{a}$) for two values of the normalized gain coefficient ($\bar{g}$). The saturable nonlinearity coefficient (γ) is set to zero.

8.5 Saturable Nonlinearity and Chromatic Dispersion

In this section, we will discuss the realistic case in which a saturable nonlinearity and chromatic dispersion are simultaneously present. We note once more that the solutions when $\beta_2 < 0$ are the complex conjugates of those when $\beta_2 > 0$ and $|\beta_2|$ is unchanged. In Fig. 8.14, we present a contour plot of the maximum intensity of the equilibrium modelocked pulses as the saturable loss and chromatic dispersion vary. The unstable region is shown blank. The maximum intensity has been normalized by the value of the maximum intensity of the stable modelocked pulse with $\gamma = 0$ and $\beta_2 = 0$. We note that the critical value of the saturable loss increases significantly when $|\beta_2|$ increases. We also note that the maximum intensity varies significantly with the change of the saturable loss when $|\beta_2| < 4$ ps^2/m. The maximum intensity decreases as $|\beta_2|$ increases for a fixed value of γ. When $|\beta_2| > 4$ ps^2/m, the maximum intensity does not vary much as γ changes, and the normalized maximum intensity is less than 1 even when $\gamma \approx \gamma_c$. The critical value of dispersion coefficient $|\beta_{2c}|$ increases as γ increases. We show a

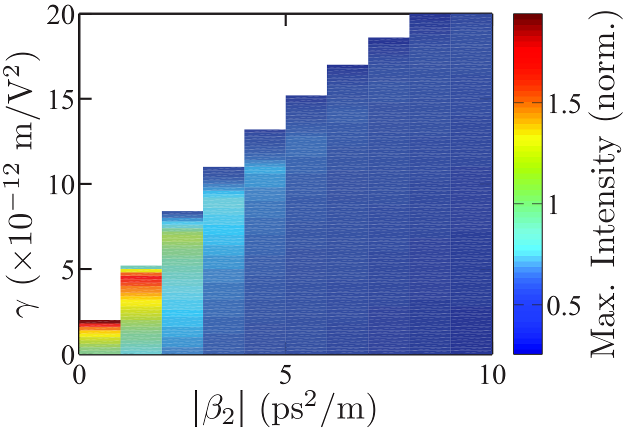

FIGURE 8.14: Contour plot of the normalized maximum intensity vs. the saturable nonlinearity coefficient ($\gamma > 0$) and chromatic dispersion coefficient (β_2). The maximum intensity has been calculated after the pulse has propagated a distance of $1000L_c$. We set $\bar{g} = 4$ and $\bar{a} = 5$.

contour plot for the duration of the modelocked pulse when saturable loss and dispersion are varied in Fig. 8.15. We note that the duration of the modelocked pulse increases when $|\beta_2|$ increases for any value of γ. However, the duration of the modelocked pulse remains approximately the same when γ increases for a fixed value of $|\beta_2|$. When dispersion is present, a larger saturable loss can be tolerated. Conversely, when saturable loss is present, pulse broadening due to dispersion is diminished. The limits on saturable loss and chromatic dispersion become less stringent when the other is present.

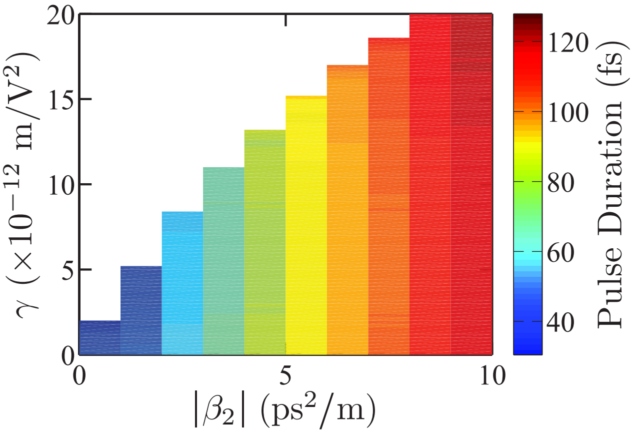

FIGURE 8.15: Contour plot of the duration vs. the saturable nonlinearity coefficient ($\gamma > 0$) and chromatic dispersion coefficient (β_2). The duration has been calculated after the pulse has propagated a distance of $1000L_c$. We set $\bar{g} = 4$ and $\bar{a} = 5$.

In Fig. 8.16, we show a contour plot for the maximum intensity of the stable modelocked pulses when saturable gain and chromatic dispersion are simultaneously present. We note that the maximum intensity only changes significantly as $|\beta_2|$ and γ change when $|\beta_2| \lesssim 5$ ps^2/m and $\gamma \gtrsim -20 \times 10^{-12}$ m/V^2. When $\gamma \lesssim -20 \times 10^{-12}$ m/V^2, the maximum pulse intensity of the modelocked pulse changes very little as $|\beta_2|$ changes. Similarly, when $|\beta_2| \gtrsim 5$ ps^2/m, the maximum intensity of the modelocked pulse is essentially same for any amount of saturable gain. Critical values of the saturable gain do not vary much when the dispersion coefficient is varied. The critical value of dispersion coefficient $|\beta_{2c}|$ decreases as $|\gamma|$ increases. In Fig. 8.17, we show a contour plot of the stable modelocked pulse

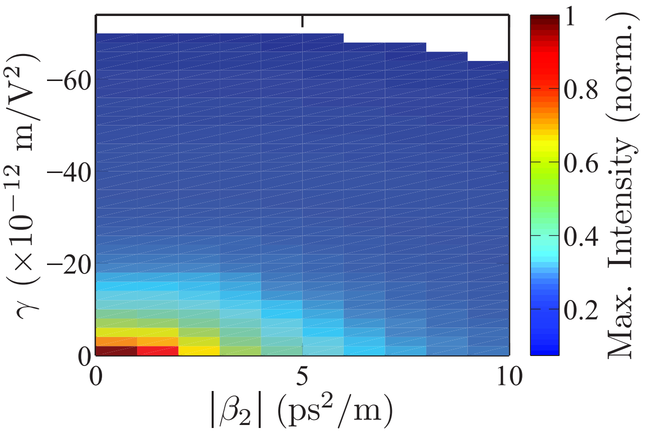

FIGURE 8.16: Contour plot of the normalized maximum intensity vs. the saturable nonlinearity coefficient ($\gamma < 0$) and chromatic dispersion coefficient (β_2). The maximum intensity has been calculated after the pulse has propagated a distance of $1000L_c$. We set $\bar{g} = 4$ and $\bar{a} = 5$.

duration when both saturable gain and dispersion vary. We note that the pulse duration increases when the saturable gain increases for any $|\beta_2|$. Similarly, the pulse duration increases when $|\beta_2|$ increases for any amount of saturable gain. The equilibrium duration decreases by well over a factor of 100 before the initial pulse becomes unstable. However, the equilibrium pulse duration when the saturable gain is just below the critical value stays approximately the same as $|\beta_2|$ is varied.

8.6 Conclusion

In conclusion, we show that QCLs can be modelocked using the SIT effect in the presence of a saturable nonlinearity, either saturable loss or saturable gain, and in the presence of chromatic dispersion, as long as their magnitudes are below critical limits. However, the modelocked pulse's equilibrium duration and maximum intensity are affected. The saturable loss sets a more stringent limit on $|\gamma_c|$ than does the saturable gain. The limits are 1.9×10^{-12} m/V^2 and 68×10^{-12} m/V^2 with $\bar{g} = 4$ and $\bar{a} = 5$, which differ by more than a factor of 30. However, when chromatic dispersion is present, the limit on $|\gamma_c|$ increases significantly in the case

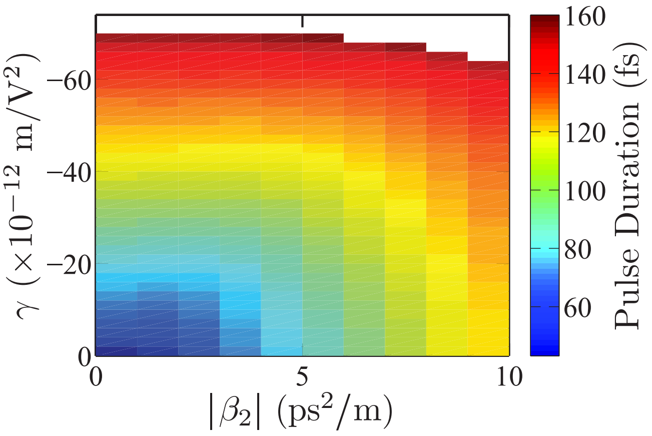

FIGURE 8.17: Contour plot of the duration vs. the saturable nonlinearity coefficient ($\gamma < 0$) and chromatic dispersion (β_2). The duration has been calculated after the pulse has propagated a distance of $1000L_c$. We set $\bar{g} = 4$ and $\bar{a} = 5$.

of saturable loss, while $|\gamma_c|$ is relatively unaffected in the case of saturable gain. The critical limits of saturable nonlinearity and chromatic dispersion also change significantly when $\bar{g}$ and $\bar{a}$ change.

The saturable nonlinearity calculated by Gordon *et al.* ($\sim 10^{-11}$ m/V^2) [29] and the chromatic dispersion calculated by Choi *et al.* (-4.6 ps^2/m) [175] for particular QCLs are within the stable regime in Fig. 8.14 and in Fig. 8.15. The magnitude of the saturable nonlinearity coefficient γ depends on the gain linewidth and on the lateral dimension of the laser core. Thus, one can always reduce γ in principle to ensure stable operation by properly designing the QCL.

Chapter 9

Conclusions

QCLs cannot be passively modelocked in their conventional parameter regimes. While active modelocking has been demonstrated using a specially-engineered QCL structure, passive modelocking has yet to be reported. Actively modelocked QCLs cannot produce sub-ps pulses. The objective of this dissertation is to demonstrate a way to modelock QCLs in their usual parameter regime and thus to open a path to the generation of ultra-short pulses (sub-ps) in the mid-infrared range. We find that though the usual parameter regimes are not suitable for conventional passive modelocking, they are suitable to use SIT modelocking. The capability of band engineering and the possibility of interleaving gain periods and absorbing periods make QCLs an ideal tool for obtaining SIT modelocking. While modelocking using the SIT effect in a laser that has an absorbing medium in addition to a gain medium was proposed earlier by Kozlov [118], a realistic laser structure has never previously been proposed. In Kozlov's hypothetical structure, the gain and absorbing medium are spatially separate along the length of the laser cavity. Kozlov assumed that the pulse energy does not change when a pulse traverses through the gain or absorbing medium in a single trip; this configuration is not realizable. On the contrary, we have designed realistic QCL structures that have gain and absorbing periods interleaved along the growth axis. Therefore, the gain and absorbing media interact simultaneously with an optical pulse, and it is possible to create stable pulses over a broad parameter regime.

We now summarize the major accomplishments of this dissertation:

- We have proposed that QCLs can be modelocked using the SIT effect. We have explained in detail the physical concept of SIT modelocking in QCLs that have absorbing periods in addition to the gain periods. We have described the set of conditions that a QCL has to satisfy in order to experience SIT modelocking. Subsequently, we solved Maxwell-Bloch equations that describe the dynamics in a QCL. We obtained analytical solutions for the modelocked pulses in special cases when absorbing periods have a dipole moment twice as large as the dipole moment in the gain periods, the gain recovery times in both the gain and absorbing periods are infinite, there is no detuning between the resonant levels of the gain and absorbing periods, and the initial pulse is a π pulse in the gain medium. We derived the conditions that are required to obtain stable modelocked pulses. However, to determine the solutions in more general cases, i.e., when the ratio of the dipole moment of the absorbing to gain periods is not two, the gain recovery times are finite and are on the order of a ps, there is a finite detuning between the resonant levels of the gain and the absorbing periods, and the initial pulse is not a π pulse in the gain medium, we solved the Maxwell-Bloch equations computationally. We carried out an extensive study to calculate the stability limits of the key parameters. We found that there exists a broad stability regime for the key parameters that we just mentioned and that the parameters of existing QCLs are well within this regime. Our claim that QCLs are the ideal tool to achieve modelocking using SIT was established through these studies.

- We have reviewed QCL theory and modeling concepts. Based on standard approaches, we have built simulation tools to design QCLs. Electronic states for the multi-quantum well QCL structures were found using the envelope function approximation. We have studied QCLs that consist of GaAs/AlGaAs and InGaAs/AlInAs material systems lattice-matched or strain-compensated. The electronic states are used to characterize the QCLs by calculating key physical quantities, including electron scattering lifetimes, tunneling rates, dipole moments, and transition energies.

- We have developed a carrier transport model for QCLs. Calculating the carrier transport rate and understanding the physical phenomena that determine that rate is important in both estimating the device performance and finding ways to improve the performance. For SIT modelocking, it is also important to calculate the ratio of gain and absorption coefficients so that the number of gain and absorbing periods that are required for stable modelocking can be estimated. We include both incoherent scattering mechanisms and coherent tunneling mechanisms in the model. We also take into account the mutual coherence time between the levels. Calculation of the mutual coherence time is important. It affects the carrier transport through tunneling, and it also affects the propagation of a resonant pulse through the active medium since it determines the decay of the polarization of the carriers in the two resonant levels. We have studied the effects of different operating and design parameters on the carrier transport. In particular, we found that the carrier transport through tunneling decreases at high temperature because the coherence between the levels decays at a faster rate as the temperature increases.

- Based on the theory of QCLs and using the simulation tool we have developed, we designed SIT modelocked QCL structures that emit light at two different wavelength, i.e., at ~ 8 μm and ~ 12 μm. Similar structures can be grown to emit light at different mid-infrared wavelengths. In both designs, the gain and absorbing periods are resonant and the absorbing periods have a dipole moment approximately twice as large as the dipole moment in the gain periods. The electrons are injected into the upper resonant levels in the gain periods to produce gain; however, they are injected into the lower resonant levels in the absorbing periods to absorb continuous waves. Using the carrier transport model that we developed, we calculated the carrier densities at the resonant levels of the SIT-modelocking QCLs. These carrier densities, along with the calculated coherence times between the resonant levels in the gain and absorbing periods, have been used to calculate the required ratio of gain to absorbing periods.

- When propagating waves bounce back from the edges of a QCL cavity, they may interfere and produce standing waves. Since QCLs have a very fast gain recovery time on the order of a ps, spatial hole burning can be observed in conventional QCLs that have only gain periods when the input current is above the lasing threshold. Additionally, when pulses bounce back from the laser edges and travel in the opposite direction, a portion of the cavity may not have regained its equilibrium population inversion. The extent of the gain recovery depends on the gain recovery time. Additionally, a significant amount of energy is lost at the two edges. Therefore, we have implemented a propagation model where counter-propagating waves and lumped mirror losses are taken into account. We studied the modelocked pulse evolution and calculated the stability limits. We showed that lumped mirror losses and the incomplete gain recovery when the pulses bounce back from the edges reduce the upper stability limits of the absorption coefficients for a fixed gain coefficient. We found that spatial hole burning is not an issue for SIT modelocking in QCLs when the continuous waves are suppressed; however, spatial-hole burning is observed in the parameter regime where continuous waves can grow.

- QCLs have been shown to produce large nonlinearity. Intensity-dependent loss has been observed to lead to self-focusing and a reduction in the threshold for the Risken-Nummedal-Graham-Haken instability. Since the stability of SIT modelocking depends on the values of the gain and absorption coefficients relative to the value of loss, the stability will change when the medium has saturable loss or saturable gain. The pulses in a QCL are affected by chromatic dispersion. The narrow pulses produced using SIT modelocking may broaden when they propagate inside a dispersive medium and may be completely damped. Therefore, we have studied the effects of the saturable nonlinearity, i.e., saturable gain and saturable loss, and chromatic dispersion on SIT modelocking. We studied the pulse evolution under various conditions and calculated the critical values of the nonlinearity and dispersion inside of which the pulse evolution is stable. We showed that the typical nonlinearity and chromatic dispersion that are present in a QCL lie well within the allowed range of these parameters for stable operation.

In this dissertation, we assumed that the initial pulse is injection-locked from an external source. As long as the initial pulse has a duration and energy that lie within the range presented in Chapter 3, modelocking is observed and the pulse reaches its equilibrium duration, which is ultimately determined by the normalized gain and absorption coefficients. While this approach is sufficient for an experimental demonstration, an approach that generates the seed pulse from the modelocked QCL itself will be necessary for practical applications. It is possible that active modelocking may be used to generate the seed pulse. In that approach a two-segment QCL should be used with the gain and absorption coefficients modulated in one segment. Such an approach with only gain periods produces active mode-locking and has been demonstrated by Wang *et al.* [13]. However, it is an open question whether active modelocking can be achieved when absorbing periods are interleaved with gain periods. A combination of active-SIT modelocking is worth studying in future.

Bibliography

[1] R. F. Kazarinov and R. A. Suris, "Possibility of amplification of electromagnetic waves in a semiconductor with a superlattice," Sov. Phys. Semicond. **5**, 707–709 (1971).

[2] F. Capasso, K. Mohammed, and A. Y. Cho, "Sequential resonant tunneling through a multiquantum well superlattice," Appl. Phys. Lett. **48**, 478–480 (1986).

[3] C. Sirtori, P. Kruck, S. Barbieri, P. Collot, and J. Nagle, "GaAs/Al$_x$Ga$_{1-x}$As quantum cascade lasers," Appl. Phys. Lett. **73**, 3486–3488 (1998).

[4] L. Esaki and R. Tsu, "Superlattice and negative differential conductivity in semiconductors," IBM J. Res. Devel. **14**, 61–65 (1970).

[5] A. Yariv, *Quantum Electronics* (Wiley, New York, 1989).

[6] H. T. Grahn, *Semiconductor Superlattices Growth and Electronic Properties* (World Scientific, Singapore, 1995).

[7] J. Faist, F. Capasso, D. Sivco, C. Sirtori, A. Hutchinson, and A. Cho, "Quantum cascade laser," Science **264**, 553–556 (1994).

[8] A. Y. Cho and J. R. Arthur Jr., "Molecular beam epitaxy," Prog. Solid State Chem. **10**, 157–192 (1975).

[9] A. Cho, *Molecular Beam Epitaxy* (API Press, Woodbury, NW, 1994).

[10] C. Gmachl, D. L. Sivco, R. Colombelli, F. Capasso, and A. Y. Cho, "Ultrabroadband semiconductor laser," Nature **415**, 883–887 (2002).

[11] M. Razeghi, "High-performance InP-based mid-IR quantum cascade lasers," IEEE J. Sel. Topics in Quantum Electron. **15**, 941–951 (2009).

[12] A. Hugi, R. Terazzi, Y. Bonetti, A. Wittmann, M. Fischer, M. Beck, J. Faist, and E. Gini, "External cavity quantum cascade laser tunable from 7.6 to 11.4 μm," Appl. Phys. Lett. **95**, 061103 (2009).

[13] C. Y. Wang, L. Kuznetsova, V. M. Gkortsas, L. Diehl, F. X. Kärtner, M. A. Belkin, A. Belyanin, X. Li, D. Ham, H. Schneider, P. Grant, C. Y. Song, S. Haffouz, Z. R. Wasilewski, H. C. Liu, and F. Capasso, "Mode-locked pulses from mid-infrared quantum cascade lasers," Opt. Express **17**, 12929–12943 (2009).

[14] A. E. Siegman, *Lasers* (University Science Books, California, 1986).

[15] J. J. Macklin, J. D. Kmetec, and C. L. Gordon III, "High-order harmonic generation using intense femtosecond pulses," Phys. Rev. Lett. **70**, 766–769 (1993).

[16] J. M. Dudley, G. Genty, and S. Coen, "Supercontinuum generation in photonic crystal fiber," Rev. Mod. Phys. **78**, 1135–1184 (2006).

[17] E. A. Gibson, A. Paul, N. Wagner, R. Tobey, D. Gaudiosi, S. Backus, I. P. Christov, A. Aquila, E. M. Gullikson, D. T. Attwood, M. M. Murnane, and H. C. Kapteyn, "Coherent soft x-ray generation in the water window with quasi-phase matching," Science **302**, 95–98 (2003).

[18] R. Huber, F. Tauser, A. Brodschelm, M. Bichler, G. Abstreiter, and A. Leitenstorfer, "How many-particle interactions develop after ultrafast excitation of an electron-hole plasma," Nature **414**, 286–289 (2001).

[19] R. Torre, P. Bartolini, and R. Righini, "Structural relaxation in supercooled water by time-resolved spectroscopy," Nature **428**, 296–299 (2004).

[20] D. Meshulach and Y. Silberberg, “Coherent quantum control of two-photon transitions by a femtosecond laser pulse,” Nature **396**, 239–242 (1998).

[21] W. S. Warren, H. Rabitz, and M. Dahleh, “Coherent control of quantum dynamics: The dream is alive,” Science **259**, 1581–1589 (1993).

[22] T. Udem, R. Holzwarth, and T. W. Hänsch, “Optical frequency metrology,” Nature **416**, 233–237 (2002).

[23] P. Loza-Alvarez, C. T. Brown, D. T. Reid, W. Sibbett, and M. Missey, “High-repetition-rate ultrashort-pulse optical parametric oscillator continuously tunable from 2.8 to 6.8 μm,” Opt. Lett. **24**, 1523–1525 (1999).

[24] S. French, M. Ebrahimzadeh, and A. Miller, “High-power, high-repetition-rate picosecond optical parametric oscillators for the near- to mid-infrared,” J. Mod. Opt. **43**, 929–952 (1996).

[25] M. R. X. de Barros, R. S. Miranda, T. M. Jedju, and P. C. Becker, “High-repetition-rate femtosecond midinfrared pulse generation,” Opt. Lett. **20**, 480–482 (1995).

[26] H. Okamoto and M. Tasumi, “Generation of ultrashort light-pulses in the midinfrared (3000–80 cm^{-1}) by 4-wave-mixing,” Opt. Commun. **121**, 63–68 (1995).

[27] H. A. Haus, “Mode-locking of lasers,” IEEE J. Sel. Quantum Electron. **6**, 1173–1185 (2000).

[28] C. Y. Wang, L. Diehl, A. Gordon, C. Jirauschek, F. X. Kärtner, A. Belyanin, D. Bour, S. Corzine, G. Höfler, M. Troccoli, J. Faist, and F. Capasso, “Coherent instabilities in a semiconductor laser with fast gain recovery,” Phys. Rev. A **75**, 031802 (2007).

[29] A. Gordon, C. Y. Wang, L. Diehl, F. X. Kärtner, A. Belyanin, D. Bour, S. Corzine, G. Höfler, H. C. Liu, H. Schneider, T. Maier, M. Troccoli, J. Faist,

and F. Capasso, "Multimode regimes in quantum cascade lasers: From coherent instabilities to spatial hole burning," Phys. Rev. A **77**, 053804 (2008).

[30] C. Sirtori and R. Teissier, *Intersubband Transitions in Quantum Structures* (McGraw-Hill, New York, 2006).

[31] H. Choi, L. Diehl, Z.-K. Wu, M. Giovannini, J. Faist, F. Capasso, and T. B. Norris, "Gain recovery dynamics and photon-driven transport in quantum cascade lasers," Phys. Rev. Lett. **100**, 167401 (2008).

[32] H. Choi, L. Diehl, Z.-K. Wu, M. Giovannini, J. Faist, F. Capasso, and T. B. Norris, "Time-resolved investigations of electronic transport dynamics in quantum cascade lasers based on diagonal lasing transition," IEEE J. Quantum Electron. **45**, 307–321 (2009).

[33] H. Risken and K. Nummedal, "Self-pulsing in lasers," J. Appl. Phys. **39**, 4662–4672 (1968).

[34] R. Graham and H. Haken, "Quantum theory of light propagation in a fluctuating laser-active medium," Z. Phys. **213**, 420–450 (1968).

[35] R. Paiella, F. Capasso, C. Gmachl, D. L. Sivco, J. N. Baillargeon, A. L. Hutchinson, A. Y. Cho, and H. C. Liu, "Self-mode-locking of quantum cascade lasers with giant ultrafast optical nonlinearites," Science **290**, 1739–1742 (2000).

[36] R. Paiella, F. Capasso, C. Gmachl, H. Y. Hwang, D. L. Sivco, A. L. Hutchinson, A. Y. Cho, and H. C. Liu, "Monolithic active mode locking of quantum cascade lasers," Appl. Phys. Lett. **77**, 169–171 (2000).

[37] A. Soibel, F. Capasso, C. Gmachl, M. L. Peabody, A. M. Sergent, R. Paiella, D. L. Sivco, A. Y. Cho, and H. C. Liu, "Stability of pulse emission and enhancement of intracavity second-harmonic generation in self-mode-locked quantum cascade lasers," IEEE J. Quantum Electron. **40**, 197–204 (2004).

[38] A. Soibel, F. Capasso, C. Gmachl, M. L. Peabody, A. M. Sergent, R. Paiella, H. Y. Hwang, D. L. Sivco, A. Y. Cho, H. C. Liu, C. Jirauscheck, and F. X. Kärtner, "Active mode locking of broadband quantum cascade lasers," IEEE J. Quantum Electron. **40**, 844–851 (2004).

[39] S. L. McCall and E. L. Hahn, "Self-induced transparency by pulsed coherent light," Phys. Rev. Lett. **18**, 908–912 (1967).

[40] S. L. McCall and E. L. Hahn, "Self-induced transparency," Phys. Rev. **183**, 457–489 (1969).

[41] C. K. Patel and R. E. Slusher, "Self-induced transparency in gases," Phys. Rev. Lett. **19**, 1019–1022 (1967).

[42] C. K. Rhodes, A. Szöke, and A. Javan, "The influence of level degeneracy on the self-induced transparency effect," Phys. Rev. Lett. **21**, 1151–1155 (1968).

[43] C. K. Patel, "Investigation of pulse delay in self-induced transparency," Phys. Rev. A **1**, 979–982 (1970).

[44] H. M. Gibbs and R. E. Slusher, "Peak amplification and breakup of a coherent optical pulse in a simple atomic absorber," Phys. Rev. Lett. **24**, 638–641 (1970).

[45] R. E. Slusher and H. M. Gibbs, "Self-induced transparency in atomic rubidium," Phys. Rev. A **5**, 1634–1659 (1972).

[46] H. M. Gibbs and R. E. Slusher, "Optical pulse compression by focusing in a resonant absorber," Appl. Phys. Lett. **18**, 505–507 (1971).

[47] R. Bonifacio and L. M. Narducci, "Short-pulse propagation in a laser amplifier with saturable losses," Lett. Nuovo Cimento **1**, 671–676 (1969).

[48] K. Gürs and R. Müller, "Breitband-modulation durch Steuerung der emission eines optischen masers (Auskopple-modulation)," Phys. Lett. **5**, 179–181 (1963).

[49] K. Gürs, *Quantum Electronics III* (Columbia Univ. Press, New York, 1964).

[50] H. Statz and C. L. Tang, *Quantum Electronics III* (Columbia Univ. Press, New York, 1964).

[51] M. DiDomenico Jr., "Small-signal analysis of internal (coupling-type) modulation of lasers," J. Appl. Phys. **35**, 2870–2876 (1964).

[52] L. E. Hargrove, R. L. Fork, and M. A. Pollack, "Locking of He-Ne laser modes induced by synchronous intracavity modulation," Appl. Phys. Lett. **5**, 4–6 (1964).

[53] A. Yariv, "Internal modulation in multimode laser oscillators," J. Appl. Phys. **36**, 388–391 (1965).

[54] H. W. Mocker and R. J. Collins, "Mode competition and self-locking effects in a Q-switched ruby laser," Appl. Phys. Lett. **7**, 270–272 (1965).

[55] E. P. Ippen, C. V. Shank, and A. Dienes, "Passive mode locking of the cw dye laser," Appl. Phys. Lett. **21**, 348–350 (1972).

[56] C. V. Shank and E. P. Ippen, "Sub-picosecond kilowatt pulses from a mode-locked cw dye laser," Appl. Phys. Lett. **24**, 373–375 (1974).

[57] J. G. Fujimoto, A. M. Weiner, and E. P. Ippen, "Generation and measurement of optical pulses as short as 16 fs," Appl. Phys. Lett. **44**, 832–834 (1984).

[58] R. L. Fork, B. I. Greene, and C. V. Shank, "Generation of optical pulses shorter than 0.1 psec by colliding pulse mode-locking," Appl. Phys. Lett. **38**, 617–619 (1981).

[59] W. H. Knox, R. L. Fork, M. C. Downer, R. H. Stolen, C. V. Shank, and J. A. Valdmanis, "Optical pulse compression to 8 fs at a 5-kHz repetition rate," Appl. Phys. Lett. **46**, 1120–1122 (1985).

[60] R. L. Fork, C. H. B. Cruz, P. C. Becker, and C. V. Shank, "Compression of optical pulses to six femtoseconds by using cubic phase compensation," Opt. lett. **12**, 483–485 (1987).

[61] M. H. Crowell, "Characteristics of mode-coupled lasers," IEEE J. Quantum Electron. **1**, 12–20 (1965).

[62] D. I. Kuizenga and A. E. Siegman, "Modulator frequency detuning effects in the FM mode-locked laser," IEEE J. Quantum Electron. **QE-6**, 803–808 (1970).

[63] H. A. Haus, "Theory of mode locking with a fast saturable absorber," J. Appl. Phys. **46**, 3049–3058 (1975).

[64] H. A. Haus, "Theory of mode locking with a slow saturable absorber," IEEE J. Quantum Electron. **9**, 736–746 (1975).

[65] M. W. Phillips, A. I. Ferguson, and D. C. Hanna, "Frequency-modulation mode locking of a Nd^{3+}-doped fiber laser," Opt. Lett. **14**, 219–221 (1989).

[66] G. T. Maker and A. I. Ferguson, "Frequency-modulation mode locking of a diode-pumped Nd:YAG laser," Opt. Lett. **14**, 788–790 (1989).

[67] W. H. Glenn, M. J. Brienza, and A. J. DeMaria, "Mode locking of an organic dye laser," Appl. Phys. Lett. **12**, 54–56 (1968).

[68] D. J. Bradley and A. J. F. Durrant, "Generation of ultrashort dye laser pulses by mode locking," Phys. Lett. A **27**, 73–74 (1968).

[69] B. H. Soffer and J. W. Lin, "Continuously tunable picosecond-pulse organic-dye laser," J. Appl. Phys. **39**, 5859–5860 (1968).

[70] C. K. Chan and S. O. Sari, "Tunable dye laser pulse converter for production of picosecond pulses," Appl. Phys. Lett. **25**, 403–406 (1974).

[71] J. M. Harris, R. W. Chrisman, and F. E. Lytle, "Pulse generation in a cw dye laser by mode-locked synchronous pumping," Appl. Phys. Lett. **26**, 16–18 (1975).

[72] I. D. Jung, F. X. Kärtner, N. Matuschek, D. H. Sutter, F. M.-Genoud, G. Zhang, U. Keller, V. Scheuer, M. Tilsch, and T. Tschudi, "Self-starting 6.5-fs pulses from a Ti:sapphire laser," Opt. Lett. **22**, 1009–1011 (1997).

[73] R. Herda and O. G. Okhotnikov, "Dispersion compensation-free fiber laser mode-locked and stabilized by high-contrast saturable absorber mirror," IEEE J. Quantum Electron. **40**, 893–899 (2004).

[74] R. Herda, O. G. Okhotnikov, E. U. Rafailov, and A. Starodumov, "Semiconductor quantum-dot saturable mode-locked fiber laser," IEEE Photon. Technol. Lett. **18**, 157–159 (2006).

[75] S. Y. Set, H. Yaguchi, Y. Tanaka, and M. Jablonski, "Laser mode locking using a saturable absorber incorporating carbon nanotubes," J. Lightwave Technol. **22**, 51–56 (2004).

[76] V. J. Matsas, T. P. Newson, D. J. Richardson, and D. J. Payne, "Self-starting passively mode-locked fiber ring soliton laser exploiting nonlinear polarization rotation," Electron. Lett. **28**, 1391–1393 (1992).

[77] N. J. Doran and D. Wood, "Non-linear optical loop mirror," Opt. Lett. **14**, 56–58 (1988).

[78] D. E. Spence, P. N. Kean, and W. Sibbett, "60-fsec pulse generation from a self-mode-locked Ti:Sapphire laser," Opt. Lett. **16**, 42–44 (1991).

[79] D. K. Negus, L. Spinelli, N. Goldblatt, and G. Feugnet, "Sub-100 femtosecond pulse generation by Kerr lens mode-locking in Ti:Al_2O_3," OSA Proc. Advanced Solid-State Lasers **10**, 120–124 (1991).

[80] T. Brabec, C. Spielmann, P. F. Curley, and F. Krausz, "Kerr lens mode-locking," Opt. Lett. **17**, 1292–1294 (1992).

[81] L. C. West and S. J. Eglash, "First observation of an extremely large-dipole infrared transition within the conduction band of a GaAs quantum well," Appl. Phys. Lett. **46**, 1156–1158 (1985).

[82] M. Helm, E. Colas, P. England, F. Derosa, and S. J. Allen, "Observation of grating-induced intersubband emission from GaAs/AlGaAs superlattice," Appl. Phys. Lett. **53**, 1714–1716 (1988).

[83] M. Helm, E. Colas, P. England, F. Derosa, and S. J. Allen, "Intersubband emission from semiconductor superlattices excited by sequential resonant tunneling," Phys. Rev. Lett. **63**, 74–77 (1989).

[84] F. Capasso, R. Paiella, R. Martini, R. Colombelli, C. Gmachl, T. L. Myers, M. S. Taubman, R. M. Williams, C. G. Bethea, K. Unterrainer, H. Y. Hwang, D. L. Sivco, A. Y. Cho, A. M. Sergent, H. C. Liu, and E. A. Whittaker, "Quantum cascade lasers: Ultrahigh-speed operation, optical wireless communication, narrow linewidth, and far-infrared emission," IEEE J. Quantum Electron. **38**, 511–532 (2002).

[85] J. Faist, D. Hofstetter, M. Beck, T. Aellen, M. Rochat, and S. Blaser, "Bound-to-continuum and two-phonon resonance quantum-cascade lasers for high duty cycle, high-temperature operation," IEEE J. Quantum Electron. **38**, 533–546 (2002).

[86] C. Gmachl, F. Capasso, D. L. Sivco, and A. Y. Cho, "Recent progress in quantum cascade lasers and applications," Rep. Prog. Phys. **64**, 1533–1601 (2001).

[87] M. P. Semtsiv, M. Wienold, S. Dressler, and W. T. Masselink, "InP-based strain-compensated quantum cascade lasers," Appl. Phys. Lett. **90**, 051111 (2007).

[88] D. G. Revin, J. W. Cockburn, M. J. Steer, R. J. Airey, M. Hopkinson, A. B. Krysa, L. R. Wilson, and S. Menzel, "InGaAs/AlAsSb/InP quantum cascade lasers operating at wavelengths close to 3 μm," Appl. Phys. Lett. **90**, 021108 (2007).

[89] J. S. Yu, A. Evans, S. Slivken, S. R. Darvish, and M. Razeghi, "Temperature dependent characteristics of $\lambda \sim 3.8$ μm room-temperature continuous-wave quantum-cascade lasers," Appl. Phys. Lett. **88**, 251118 (2006).

[90] B. S. Williams, S. Kumar, H. Callebaut, Q. Hu, and J. L. Reno, "Terahertz quantum-cascade laser at $\lambda \approx 100$ μm using metal waveguide for mode confinement," Appl. Phys. Lett. **83**, 2124–2126 (2003).

[91] B. S. Williams, S. Kumar, Q. Hu, and J. L. Reno, "Operation of terahertz quantum-cascade lasers at 164 K in pulsed mode and at 117 K in continuous-wave mode," Opt. Express **13**, 3331–3339 (2005).

[92] B. S. Williams, "Terahertz quantum cascade lasers," Nature Photon. **1**, 517–525 (2007).

[93] C. Walther, M. Fischer, G. Scalari, R. Terazzi, N. Hoyler, and J. Faist, "Quantum cascade lasers operating from 1.2 to 1.6 THz," Appl. Phys. Lett. **91**, 131122 (2007).

[94] M. A. Belkin, J. A. Fan, S. Hormoz, F. Capasso, S. P. Khanna, M. Lachab, A. G. Davies, and E. H. Linfield, "Terahertz quantum cascade lasers with copper metal-metal waveguides operating up to 178 K," Opt. Express **16**, 3242–3248 (2008).

[95] M. A. Belkin, F. Capasso, F. Xie, A. Belyanin, M. Fischer, A. Wittmann, and J. Faist, "Room temperature terahertz quantum cascade laser source based on intracavity difference-frequency generation," Appl. Phys. Lett. **92**, 201101 (2008).

[96] A. Evans, J. S. Yu, S. Slivken, and M. Razeghi, "Continuous-wave operation of $\lambda \sim 4.8$ μm quantum-cascade lasers at room temperature," Appl. Phys. Lett. **85**, 2166–2168 (2004).

[97] J. S. Yu, A. Evans, J. David, L. Doris, S. Slivken, and M. Razeghi, "High-power continuous-wave operation of quantum-cascade laser up to 60 °C," IEEE Photon. Technol. Lett. **16**, 747–749 (2004).

[98] L. Diehl, D. Bour, S. Corzine, J. Zhu, G. Hofler, M. Loncar, M. Troccoli, and F. Capasso, "High-power quantum cascade lasers grown by low-pressure metal organic vapor-phase epitaxy operating in continuous wave above 400 K," Appl. Phys. Lett. **88**, 201115 (2006).

[99] S. Kumar, *Development of terahertz quantum cascade lasers*, Ph.D. Dissertation, Massachusetts Institute of Technology (2007).

[100] T. Aellen, R. Maulini, R. Terazzi, N. Hoyler, M. Giovannini, J. Faist, S. Blaser, and L. Hvozdara, "Direct measurement of the linewidth enhancement factor by optical heterodyning of an amplitude-modulated quantum cascade laser," Appl. Phys. Lett. **89**, 091121 (2006).

[101] I. Vurgaftman and J. R. Meyer, "Photonic-crystal distributed-feedback quantum cascade lasers," IEEE J. Quantum Electron. **38**, 592–602 (2002).

[102] R. Paiella, R. Martini, F. Capasso, C. Gmachl, H. Y. Hwang, D. L. Sivco, J. N. Baillargeon, A. Y. Cho, E. A. Whittaker, and H. C. Liu, "High-frequency modulation without the relaxation oscillation response in quantum cascade lasers," Appl. Phys. Lett. **79**, 2526–2528 (2001).

[103] B. Lax,"[111] direct transition exciton and magnetoreflection in germanium," Phys. Rev. Lett. **4**, 511–513 (1960).

[104] R. N. Hall, G. E. Fenner, J. D. Kingsley, T. J. Soltys, and R. O. Carlson, "Coherent light emission from GaAs junctions," Phys. Rev. Lett. **9**, 366–369 (1962).

[105] L. L. Bonilla and H. T. Grahn, "Non-linear dynamics of semiconductor superlattices," Rep. Prog. Phys. **68**, 577–683 (2005).

[106] L. L. Chang, L. Esaki, and R. Tsu, "Resonant tunneling in semiconductor double barriers," Appl. Phys. Lett. **24**, 593–595 (1974).

[107] J. Faist, F. Capasso, C. Sirtori, and D. L. Sivco, *Intersubband Transitions in Quantum Wells: Physics and Device Applications II* (Academic Press, San Diego, CA, 2000).

[108] F. Capasso, K. Mohammed, and A. Y. Cho, "Resonant tunneling through double barriers, perpendicular quantum transport phenomena in superlattices, and their device applications," IEEE J. Quantum Electron. **22**, 1853–1869 (1986).

[109] F. Capasso, "Band-gap engineering: From physics and materials to new semiconductor devices," Science **235**, 172–176 (1987).

[110] M. Beck, D. Hofstetter, T. Aellen, J. Faist, U. Oesterle, M. Ilegems, E. Gini, and H. Melchior, "Continuous wave operation of a mid-infrared semiconductor laser at room temperature," Science **295**, 301–305 (2002).

[111] M. Woerner, K. Reimann, and T. Elsaesser, "Coherent charge transport in semiconductor quantum cascade structures," J. Phys.: Condens. Matter **16**, R25–R48 (2004).

[112] A. Wittmann, Y. Bonetti, J. Faist, E. Gini, and M. Giovannini, "Intersubband linewidths in quantum cascade laser designs," Appl. Phys. Lett. **93**, 141103 (2008).

[113] T. Uchida and A. Ueki, "Self locking of gas lasers," IEEE J. Quantum Electron. **3**, 17–30 (1967).

[114] A. G. Fox and P. W. Smith, "Mode-locked laser and the 180° pulse," Phys. Rev. Lett. **18**, 826–828 (1967).

[115] P. W. Smith, "The self-pulsing laser oscillator," IEEE J. Quantum Electron. **3**, 627–635 (1967).

[116] A. Frova, M. A. Duguay, C. G. B. Garrett, and S. L. McCall, "Pulse delay effects in the He-Ne laser mode-locked by a Ne absorption cell," J. Appl. Phys. **40**, 3969–3972 (1969).

[117] V. V. Kozlov, “Self-induced transparency soliton laser,” JETP Lett. **69**, 906–911 (1999).

[118] V. V. Kozlov, “Self-induced transparency soliton laser via coherent mode locking,” Phys. Rev. A **56**, 1607–1612 (1997).

[119] C. R. Menyuk and M. A. Talukder, “Self-induced transparency modelocking of quantum cascade lasers,” Phys. Rev. Lett. **102**, 023903 (2009).

[120] M. A. Talukder and C. R. Menyuk, “Analytical and computational study of self-induced transparency modelocking in quantum cascade lasers,” Phys. Rev. A **79**, 063841 (2009).

[121] M. A. Talukder and C. R. Menyuk, “Effects of backward propagating waves and lumped mirror losses on self-induced transparency modelocking in quantum cascade lasers,” Appl. Phys. Lett. **95**, 071109 (2009).

[122] L. Allen and J. H. Eberley, *Optical Resonance and Two Level Atoms* (Dover, New York, 1987).

[123] R. W. Boyd, *Nonlinear Optics* (Academic Press, London, 2003).

[124] H. Choi, V.-M. Gkortsas, F. X. Kärtner, L. Diehl, C. Y. Wang, F. Capasso, D. Bour, S. Corzine, J. Zhu, G. Höfler, and T. B. Norris, “Femtosecond resonant pulse propagation in quantum cascad lasers: evidence of coherent effects,” in *Proceedings of Conference on Lasers and Electro-Optics* (2008).

[125] B. K. Ridley, *Quantum Processes in Semiconductors* (Springer, Berlin, 1988).

[126] G. Bastard, “Superlattice band structure in the envelope-function approximation,” Phys. Rev. B **24**, 5693–5697 (1981).

[127] G. Bastard, “Theoretical investigations of superlattice band structure in the envelope-function approximation,” Phys. Rev. B **25**, 7584–7597 (1982).

[128] G. Bastard, *Wave Mechanics Applied to Semiconductor Heterostructures* (John Wiley & Sons, New York, 1988).

[129] M. G. Burt, "The justification for applying the effective-mass approximation to microstructures," J. Phys.: Condens. Matter **4**, 6651–6690 (1992).

[130] J. P. Loehr and M. O. Manaresh, *Semiconductor quantum wells and superlattices for long-wavelength infrared detectors* (Artech House Materials Science Library, Artech, Boston, 1993), chap. 2, pp. 159–188.

[131] P. Harrison, *Quantum Wells, Wires and Dots* (John Wiley & Sons, England, 2005).

[132] D. F. Nelson, R. C. Miller, and D. A. Kleinman, "Band nonparabolicity effects in semiconductor quantum wells," Phys. Rev. B **35**, 7770–7773 (1987).

[133] C. Sirtori, F. Capasso, J. Faist, and S. Scandolo, "Nonparabolicity and sum rule associated with bound-to-bound and bound to continuum intersubband transitions in quantum wells," Phys. Rev. B **50**, 8663–8674 (1994).

[134] G. C. Osbourn, "Strained-layer superlattices from lattice mismatched materials," J. Appl. Phys. **53**, 1586–1589 (1982).

[135] C. G. V. de Walle, "Band lineups and deformation potentials in the model-solid theory," Phys. Rev. B **39**, 1871–1883 (1989).

[136] M. Cardona and N. E. Christensen, "Comment on spectroscopy of excited states in $\mathrm{In_{0.53}Ga_{0.47}As-InP}$ single quantum wells grown by chemical-beam epitaxy," Phys. Rev. B **37**, 1011–1012 (1988).

[137] J. H. Smet, *Intrawell and interwell intersubband transitions in single and multiple quantum well heterostructures*, Ph.D. Dissertation, Massachusetts Institute of Technology (1995).

[138] B. S. Williams, *Terahertz quantum cascade lasers*, Ph.D. Dissertation, Massachusetts Institute of Technology (2003).

[139] B. S. Williams, *GaAs/AlGaAs mid-infrared quantum cascade lasers*, M.S. Thesis, Massachusetts Institute of Technology (1998).

[140] R. Ferreira and G. Bastard, "Evaluation of some scattering times for electrons in unbiased and biased single- and multiple-quantum-well structures," Phys. Rev. B **40**, 1074–1086 (1989).

[141] M. Hartig, S. Haacke, B. Deveaud, and L. Rota, "Femtosecond luminescence measurements of the intersubband scattering rate in $\mathrm{Al}_x\mathrm{Ga}_{1-x}\mathrm{As}$/GaAs quantum wells under selective excitation," Phys. Rev. B **54**, 14269–14272 (1996).

[142] J. Shah, *Hot carriers in semiconductor nanostructures* (Academic Press, San Diego, 1992).

[143] P. Harrison, "The nature of the electron distribution functions in quantum cascade lasers," Appl. Phys. Lett. **75**, 2800–2802 (1999).

[144] D. Indjin, P. Harrison, R. W. Kelsall, and Z. Ikonić, "Self-consistent scattering theory of transport and output characteristics of quantum cascade lasers," J. Appl. Phys. **91**, 9019–9026 (2002).

[145] J. H. Smet, C. G. Fonstad, and Q. Hu, "Intrawell and interwell intersubband transitions in multiple quantum wells for far-infrared sources," J. Appl. Phys. **79**, 9305–9320 (1996).

[146] T. Unuma, M. Yoshita, T. Noda, H. Sakaki, and H. Akiyama, "Intersubband absorption linewidth in GaAs quantum wells due to scattering by interface roughness, phonons, alloy disorder, and impurities," J. App. Phys. **93**, 1586–1597 (2003).

[147] P. J. Price, "Two-dimensinal electron transport in semiconductor layers. I. phonon scattering," Ann. Phys. (N.Y.) **133**, 217 (1981).

[148] S.-C. Lee, I. Galbraith, and C. R. Pidgeon, "Influence of electron temperature and carrier concentration on electron-LO-phonon intersubband scattering in wide GaAs/$\mathrm{Al}_x\mathrm{Ga}_{1-x}$As quantum wells," Phys. Rev. B **52**, 1874–1881 (1995).

[149] J. H. Heyman, K. Unterrainer, K. Craig, B. Galdrikian, M. S. Sherwin, K. Campman, P. F. Hopkins, and A. C. Gossard, "Temperature and intensity dependence of intersubband relaxation rates from photovoltage and absorption," Phys. Rev. Lett. **74**, 2682–2685 (1995).

[150] J. H. Heyman, K. Unterrainer, K. Craig, J. Williams, M. S. Sherwin, K. Campman, P. F. Hopkins, A. C. Gossard, B. N. Murding, and C. J. G. M. Langerak, "Far-infrared pump-probe measurement of the intersubband lifetime in an AlGaAs/GaAs coupled-quantum well," Appl. Phys. Lett. **68**, 3019–3021 (1986).

[151] K. Luo, H. Zheng, Z. Lu, J. Xu, Z. Xu, T. Zhang, C. Li, X. Yang, and J. Tian, "Subband separation energy dependence of intersubband relaxation time in wide quantum wells," Appl. Phys. Lett. **70**, 1155–1157 (1997).

[152] M. Hartig, S. Haacke, P. E. Selbmann, B. Deveaud, R. A. Taylor, and L. Rota, "Efficient intersubband scattering via carrier-carrier interaction in quantum wells," Phys. Rev. Lett. **80**, 1940–1943 (1998).

[153] M. Hartig, J. D. Ganiére, P. E. Selbmann, B. Deveaud, and L. Rota, "Density dependence of carrier-carrier-induced intersubband scattering in GaAs/$\mathrm{Al}_x\mathrm{Ga}_{1-x}$As quantum wells," Phys. Rev. B **60**, 1500–1503 (1999).

[154] S.-C. Lee and I. Galbraith, "The intrasubband and intersubband relaxation of nonequilibrium electron populations in wide semiconductor quantum wells," Physica E **7**, 229–232 (2000).

[155] T. Ando, "Line width of inter-subband absorption in inversion layers: Scattering from charged ions," J. Phys. Soc. Jpn. **54**, 2671–2675 (1985).

[156] T. Unuma, T. Takahashi, T. Noda, M. Yoshita, H. Sakaki, M. Baba, and H. Akiyama, “Effects of interface roughness and phonon scattering on intersubband absorption linewidth in a GaAs quantum well,” Appl. Phys. Lett. **78**, 3448–3450 (2001).

[157] S. Tsujino, A. Borak, E. Müller, M. Scheinert, C. V. Falub, H. Sigg, D. Grützmacher, M. Giovannini, and J. Faist, “Interface-roughness-induced broadening of intersubband electroluminescence in *p*-SiGe and *n*-GaInAs/AlInAs quantum-cascade structures,” Appl. Phys. Lett. **86**, 062113 (2005).

[158] P. Offermans, P. M. Koenraad, J. H. Wolter, M. Beck, T. Aellen, and J. Faist, “Digital alloy interface grading of an InAlAs/InGaAs quantum cascade laser structure studied by cross-sectional scanning tunneling microscopy,” Appl. Phys. Lett. **83**, 4131–4133 (2003).

[159] R. C. Iotti and F. Rossi, “Nature of charge transport in quantum-cascade lasers,” Phys. Rev. Lett. **87**, 146603 (2001).

[160] F. Eickemeyer, K. Reimann, M. Woerner, and T. Elsaesser, “Ultrafast coherent electron transport in semiconductor quantum cascade structures,” Phys. Rev. Lett. **89**, 047402 (2002).

[161] H. Choi, T. B. Norris, T. Gresch, M. Giovannini, J. Faist, L. Diehl, and F. Capasso, “Femtosecond dynamics of resonant tunneling and superlattice relaxation in quantum cascade lasers,” Appl. Phys. Lett. **92**, 122114 (2008).

[162] C. Sirtori, F. Capasso, J. Faist, A. Hutchinson, D. Sivco, and A. Cho, “Resonant tunneling in quantum cascade lasers,” IEEE J. Quantum Electron. **34**, 1722–1729 (1998).

[163] A. Wacker, “Coherence and spatial resolution of transport in quantum cascade lasers,” Phys. Stat. Sol. (C) **5**, 215–220 (2008).

[164] R. C. Iotti and F. Rossi, “Microscopic theory of hot-carrier relaxation in semiconductor-based quantum-cascade lasers,” Appl. Phys. Lett. **76**, 2265–2267 (2000).

[165] K. Donovan, P. Harrison, and R. W. Kelsall, “Self-consistent solutions to the intersubband rate equations in quantum cascade lasers: Analysis of a GaAs/$\mathrm{Al}_x\mathrm{Ga}_{1-x}\mathrm{As}$ device,” J. Appl. Phys. **89**, 3084–3090 (2001).

[166] T. Kubis, C. Yeh, and P. Vogl, “Quantum theory of transport and optical gain in quantum cascade lasers,” Phys. Stat. Sol. (C) **5**, 232–235 (2008).

[167] R. Nelander, A. Wacker, M. F. Pereira Jr., D. G. Revin, M. R. Soulby, L. R. Wilson, J. W. Cockburn, A. B. Krysa, J. S. Roberts, and R. J. Airey, “Fingerprints of spatial charge transfer in quantum cascade lasers,” J. Appl. Phys. **102**, 113104 (2007).

[168] I. Savić, N. Vukmirović, Z. Ikonić, D. Indjin, R. W. Kelsall, P. Harrison, and V. Milanović, “Density matrix theory of transport and gain in quantum cascade lasers in a magnetic field,” Phys. Rev. B **76**, 165310 (2007).

[169] M. F. Pereira Jr., S.-C. Lee, and A. Wacker, “Controlling many-body effects in the midinfrared gain and terahertz absorption of quantum cascade laser structures,” Phys. Rev. B **69**, 205310 (2004).

[170] S. Luryi, “Coherent versus incoherent resonant tunneling and implications for fast devices,” Superlattice. and Microstruct. **5**, 375–382 (1989).

[171] S. Barbieri, C. Sirtori, H. Page, M. Stellmacher, and J. Nagle, “Design strategies for GaAs-based unipolar lasers: Optimum injector-active region coupling via resonant tunneling,” Appl. Phys. Lett. **78**, 282–284 (2001).

[172] J. Faist, F. Capasso, C. Sirtori, D. L. Sivco, and A. L. Hutchinson, “Vertical transition quantum cascade laser with Bragg confined excited state,” Appl. Phys. Lett. **66**, 538–540 (1995).

[173] Y. Silberberg, P. W. Smith, D. J. Eilenberger, D. A. B. Miller, A. C. Gossard, and W. Wiegmann, "Passive mode locking of a semiconductor diode laser," Opt. Lett. **9**, 507–509 (1984).

[174] S. Gee, R. Coffie, P. J. Delfyett, G. Alphonse, and J. Connolly, "Intracavity gain and absorption dynamics of hybrid modelocked semiconductor lasers using multiple quantum well saturable absorbers," Appl. Phys. Lett. **71**, 2569–2571 (1997).

[175] H. Choi, L. Diehl, F. Capasso, D. Bour, S. Corzine, J. Zhu, G. Höfler, and T. B. Norris, "Time-domain upconversion measurements of group-velocity dispersion in quantum cascade lasers," Opt. Express **15**, 15898–15907 (2007).